EMBEDDED ULTRASONICS FOR SHM OF SPACE APPLICATIONS

Andrei N. Zagrai

New Mexico Institute of Mining and Technology
801 Leroy Place
Socorro, NM 87801

30 Jul 2012

Final Report

APPROVED FOR PUBLIC RELEASE; DISTRIBUTION UNLIMITED.

AIR FORCE RESEARCH LABORATORY
Space Vehicles Directorate
3550 Aberdeen Ave SE
AIR FORCE MATERIEL COMMAND
KIRTLAND AIR FORCE BASE, NM 87117-5776

DTIC COPY
NOTICE AND SIGNATURE PAGE

This report was cleared for public release by the 377 ABW Public Affairs Office and is available to the general public, including foreign nationals. Copies may be obtained from the Defense Technical Information Center (DTIC) (http://www.dtic.mil).

Qualified requestors may obtain copies of this report from the Defense Technical Information Center (DTIC) (http://www.dtic.mil).

AFRL-RV-PS-TR-2012-0087 HAS BEEN REVIEWED AND IS APPROVED FOR PUBLICATION IN ACCORDANCE WITH ASSIGNED DISTRIBUTION STATEMENT

//SIGNED//   //SIGNED//
WHITNEY REYNOLDS   BRETT J. DEBLONK, Ph.D.
Program Manager   Technical Advisor, Spacecraft Component Technology Branch

//SIGNED//
KENNETH D. BOLE, Lt Col, USAF
Deputy Chief, Spacecraft Technology Division
Space Vehicles Directorate

REPORT DOCUMENTATION PAGE

Form Approved
OMB No. 0704-0188

1. REPORT DATE (DD-MM-YY)	2. REPORT TYPE	3. DATES COVERED (From - To)
30-07-2012	Final Report	3 Feb 2009 – 23 May 2012

4. TITLE AND SUBTITLE
Embedded Ultrasonics for SHM of Space Applications

5a. CONTRACT NUMBER
FA9453-09-1-0318

5b. GRANT NUMBER

5c. PROGRAM ELEMENT NUMBER
61102F

6. AUTHOR(S)
Andrei N. Zagrai

5d. PROJECT NUMBER
2302

5e. TASK NUMBER
PPM00004813

5f. WORK UNIT NUMBER
EF001238

7. PERFORMING ORGANIZATION NAME(S) AND ADDRESS(ES)
New Mexico Institute of Mining and Technology
801 Leroy Place
Socorro, NM 87801

8. PERFORMING ORGANIZATION REPORT NUMBER

9. SPONSORING / MONITORING AGENCY NAME(S) AND ADDRESS(ES)
Air Force Research Laboratory
Space Vehicles Directorate
3550 Aberdeen Ave., SE
Kirtland AFB, NM 87117-5776

10. SPONSOR/MONITOR'S ACRONYM(S)
AFRL/RVSV

11. SPONSOR/MONITOR'S REPORT NUMBER(S)
AFRL-RV-PS-TR-2012-0087

12. DISTRIBUTION / AVAILABILITY STATEMENT
Approved for public release; Distribution Unlimited. (377ABW-2012-1081 dtd 14 Aug 2012)

13. SUPPLEMENTARY NOTES

14. ABSTRACT
The project explores application of embedded ultrasonics for monitoring integrity of space structures. Particular attention is given to the acoustic-elastic method for assessing the condition of bolted joints. The utility of the method is demonstrated for bolted structures of simple and complex geometries. The method allows for locating a loose bolt based on temporal variation of signal phase and, in structures of simple geometry, inferring correlation between torque on a bolt and associated shift in the phase of the elastic wave. A baseline-free acousto-elastic method was developed and validated on several representative structures. The opportunity to infer material parameters and boundary condition variations from embedded ultrasonic tests is highlighted. Acousto-elastic detection of a loose bolt is validated in tests involving the Plug and Play satellite and a suborbital payload. Sensor statistics and shielding are considered. It is advocated that the acousto-elastic structural health monitoring method may find a broad range of applications in space industry, particularly in pre-launch qualification and diagnosis and re-certification for a next flight.

15. SUBJECT TERMS
Structural health monitoring, acousto-elastic, embedded ultrasonics, spacecraft, bolted joints, satellite, piezoelectric sensors

16. SECURITY CLASSIFICATION OF:			17. LIMITATION OF ABSTRACT	18. NUMBER OF PAGES	19a. NAME OF RESPONSIBLE PERSON
					Whitney Reynolds
a. REPORT	b. ABSTRACT	c. THIS PAGE	Unlimited	118	19b. TELEPHONE NUMBER (include area code)
Unclassified	Unclassified	Unclassified			

Standard Form 298 (Rev. 8-98)
Prescribed by ANSI Std. 239.18

(This page intentionally left blank)

Table of Contents

List of Figures

Approved for Public Release; Distribution Unlimited.

Approved for Public Release; Distribution Unlimited.

Approved for Public Release; Distribution Unlimited.

Approved for Public Release; Distribution Unlimited.

Approved for Public Release; Distribution Unlimited.

List of Tables

ACKNOWLEDGMENTS

(This page intentionally left blank)

1   SUMMARY

In this project, application of embedded ultrasonic for structural health monitoring (SHM) of space systems has been investigated. It is envisioned that integration of SHM in a spacecraft may offer benefits at all stages of its service life: from spacecraft assembly to on-orbit aging or re-entry. Present work, however, focuses on use of SHM for spacecraft qualification before launch as the most near-term benefit in reducing qualification time and cost.

A comprehensive review was conducted on prior SHM efforts in space systems. It was found that several practical experimental systems feature fiber optic and acoustic emission sensors, which limits capability of SHM system to do active structural diagnosis. A few studies were available on use of active diagnosis approaches with embeddable piezoelectric sensors on laboratory scale specimens, but no systematic SHM efforts for space structures were considered. As a result of the review, main elements of an SHM system for spacecraft were suggested and focus on monitoring of structural interfaces as one of the main concerns during pre-launch qualification.

Considerable efforts were devoted to exploration of the acoustic-elastic method for assessing the condition of structural interfaces such as bolted joints. The utility of the method was demonstrated for bolted structures of simple and complex geometries. It was demonstrated that the efficiency of detection depends on wave propagation distance and active sensor excitation levels. The acousto-elastic method allows for locating a loose bolt based on temporal variation of signal phase and, in structures of simple geometry, inferring correlation between torque on a bolt and associated shift in the phase of the elastic wave. It was found that the effect of damage is pronounced in both instantaneous amplitude and instantaneous phase features, but phase offers much more stable detection. The Hilbert-Huang Transform has revealed deviation of instantaneous frequency over time as a possible damage detection and classification feature.

A baseline-free acousto-elastic method based on rotation of phases in the transmitted elastic wave was developed and validated on several representative structures. However, sensitivity of the baseline-free method was lower than the method involving the baseline. The baseline-free method has shown utility in detecting loose bolts located on direct wave propagation path between transmitting and receiving sensors. Another interesting fact uncovered during experimental studies was larger standard deviation of signals corresponding to "loose" condition of the joint. As a result, a new methodology for baseline-free statistics-based detection has been proposed.

The acousto-elastic method was validated in a set of experiments conducted on the PnP-1 satellite. A method involving recording a baseline of the intact condition has shown very good performance while the baseline-free method was successful in many, but not all cases.

A fundamental experimental study investigating an effect of applied static stress on the propagation of guided elastic waves has been conducted. Under applied stress, both symmetric and anti-symmetric elastic guided waves have shown a phase shift proportional to stress magnitude, but analysis of the latter one was difficult due to low amplitude and

noise contamination. In addition, it was found that a phase shift depends on mutual orientation of vectors of applied force and the direction of wave propagation. To the author's knowledge, this is the first such study.

The opportunity to infer material parameters and boundary condition variations from embedded ultrasonic tests was explored. Experiments have demonstrated the feasibility of determining elastic modulus and Poisson ratio from wave propagation tests. The effect of stress changes in boundary conditions was investigated using pitch-catch, pulse-echo and electro-mechanical impedance methods. All methods have shown utility in detecting changes in boundary condition, but pulse-echo was also instrumental in locating the site of stress variations.

An SHM experiment involving monitoring of bolted joint was developed for a New Mexico Tech payload launched on a suborbital flight in May 2011. Due to limited flight hardware, wave propagation acousto-elastic studies were conducted only in pre-flight and post-flight conditions. Analysis indicated that the spaceflight clearly changed the torque state in a bolted joint, but quantification of the change was not possible using pre and post flight data. It was confirmed that Hysol® adhesive performed well as a bonding agent for sensors during suborbital flight.

Active sensors are among most critical elements of the SHM system. Because performance of the sensors substantially influences results of structural diagnosis, sensor shielding options were investigated and statistical variation of the sensor response was considered. As a result of this study, two shielding designs were suggested and statistical data on a relatively large sensor sample set was collected. Statistical distribution for natural frequency of low frequency extensional mode was found to follow the normal distribution pattern, however natural frequencies of the high frequency thickness mode did not follow the normal distribution pattern. Noticeable differences were observed for impedance signatures of the sensor with and without leads attached. The impedance model has shown reasonable correlation with experimental data.

It is advocated that the acousto-elastic SHM method may find a broad range of applications in space industry, particularly in pre-launch qualification and diagnosis and re-certification for a next flight. SHM application to space systems may be advanced by considering and addressing the following aspects of the technology:

- Establishing a direct correlation between complex structural models and collected SHM data on material and structural integrity.
- Improving sensitivity of the baseline-free SHM methods.
- Development of lightweight hardware that may be used not only during on-the-ground testing, but also in flight environment.
- Testing of SHM methods during sub-orbital flight.
- Development and experimental validation of a statistically driven SHM model considering statistical variation of individual factors influencing damage detection.
- Exploring use of SHM beyond pre-launch qualification for on-orbit structural diagnosis, model updating and impact detection. Monitoring during vehicle's re-entry may provide information on structural disintegration.

2 INTRODUCTION

2.1 Motivation

Satellite qualification is a comparatively long process that may span for months and even years. In contrast, space applications enabling a prompt response to emerging needs require substantial reduction of the spaceship qualification time [1]. The objective of the Air Force's Responsive Space initiative is to develop technologies that would facilitate assembly, qualification and launch of a satellite in six days. To achieve such an impressive deployment time, it is envisioned that a diverse range of the responsive satellite's structural elements would fit within certain pre-defined design envelops. Critical aspects of this approach include ensuring adequate performance of structural joints and guaranteeing stability (or update-ability) of structural parameters. A promising avenue to address both issues is to consider assessing structural integrity and material state via an on-board structural health monitoring (SHM) system [2].

Joints are amongst most critical constituent elements of space structures. A weak or improperly configured joint may compromise structural integrity of a satellite and lead to substantial operational and financial losses. As a result, joints introduce notable uncertainty into the satellite structural response. To control this uncertainty, structural elements and assemblies are assigned certain pre-defined statistical envelops [2]. Verifying that the structural component with joints fits within the envelope is an important aspect of pre-launch qualification tests. In view of variability in condition and effective strength of a joint, the diagnostic procedures should consider characteristics of structural interfaces. Over a past decade, characterization of interfaces such as bolted joints and adhesive bonds has been a subject of extensive research in both academia and industry. A broad spectrum of studies is available on assessment of adhesive bonds in aeronautical structures [3,4]. This includes convectional ultrasonic scanning [5] and embedded sensor arrays [6,7]. Bolted interfaces were primarily studied in the context of determining stresses in a single bolt [8] or the effect of the deteriorated joint on a global structural vibration signature [9]. Only recently researchers considered adapting nonlinear vibration diagnostic methods to the high frequency regime [10] and utilizing embedded sensors for local assessment of a particular bolted joint [11,12]. In practice, however, there are hundreds of joints on a typical satellite and verifying the structural integrity and compliance to a specific envelop may not constitute a trivial task. Our prior work [13] has shown that utilizing the piezoelectric sensor network embedded into the aerospace structure may provide a promising avenue for diagnosis of structural condition and for qualifying interfaces in simple and complex structural elements.

Although the primary task of the satellite SHM system is diagnosis of structural interfaces during pre-launch qualification, the embedded sensor network with the associated data classification and cataloguing algorithms may allow for inferring additional information on material properties and other forms of damage such as cracks, structural fatigue and/or impact events. This synergistic aspect of the embedded health monitoring system opens opportunities for data acquisition during launch and on-orbit monitoring of structural performance. Figure 1 illustrates the diagnostic potential of the satellite SHM system. Theory and application of embedded SHM systems for monitoring cracks and other types of damage typical to aeronautical structures are extensively covered in journals [14,15] and

books [16]. A limited number of papers explore SHM of space structures [17]; the available studies mostly focus on utilization of the fiber optic technology [18].
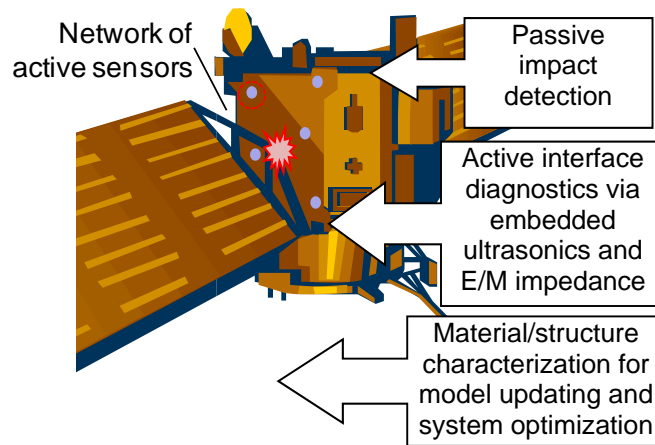
Figure 1   Diagnostic potential of the satellite SHM system

2.2 State of the Art

One of early reports on the development of SHM systems for spacecraft include the work of Bauman *et al.* [19] and Ellerbrock [20], who reported details of design, implementation, and operation of the structural health monitoring system for the NASA/McDonnell Douglas Delta DC-XA re-usable rocket. The key element of the system, a multi-channel Bragg-grating fiber optic sensor module, was utilized to monitor strains exerted on the liquid hydrogen fuel tank. Data from fiber optic and other sensors were integrated into a comprehensive SHM suite, which was flight tested in 1996. Jassemi-Zargani *et al.* [21] mentioned benefits of SHM for enhancing satellite operations. Authors discussed utilization of smart structures in enhanced satellites and suggested that real-time SHM would be useful in predicting and detecting failures in space structures. However, details on possible configuration of the SHM system were not provided, as authors primarily explored the potential of smart structures in phase-array antennas. Following the explosion of a Delta 241 rocket on January 17, 1997, Finlayson *et al.* [22] proposed application of the fiber optic wireless system for impact detection and location in Delta II graphite epoxy motors (GEM). The system was designed to operate on GEM during transport, storage and handling. Authors investigated attenuation characteristics of empty GEM using fiber optic, acoustic emission, and strain gage sensors and presented results of the impact location study. A series of research papers on application of fiber optic sensing to SHM of space structures were published by Japanese researchers led by Takeda. Kabashima et al. [23] described development of fiber Bragg grating (FBG) SHM for satellite systems. The concept of the FBG-based satellite SHM system was discussed, which encompassed potential material condition assessment during manufacturing, establishing requirements for conventional sensors (e.g. accelerometers, thermocouples, etc.) during satellite environmental tests and on-orbit detection of impact and thermal damage. Authors developed specialized optical fiber connectors and a measurement procedure to separate strain and temperature contributions in the FBG sensor signal. The potential of the embedded FBG sensors to detect thermal damage to FRP composite / aluminum panels was investigated, and results indicated

changes in position and shape of the peak in the signal reflection spectrum. Hence, the authors suggested the feasibility of thermal damage assessment using a FBG SHM system. A Brillouin optical time domain reflectometer (BOTDR) was utilized by Shimizu et al. [24] to measure strain in laboratory structures and a prototype liquid hydrogen tank. The authors suggested that a combined BOTDR and FBG system could measure strain and temperature simultaneously and independently. In a further extension of this work with FBG components in particular, was presented by Mizutani *et al.* [25]. The paper discussed design and development of an on-board strain measurement FBG system for ISAS/JAXA reusable rockets and presented results of the real-time strain monitoring during tests. The system demonstrated the capability of measuring strain during rocket operation and correlation of the FBG sensor strain data with strain-gage and internal pressure measurements. The experience of the European Space Agency (ESA) in application of fiber optic sensing in space structures was discussed by Mckenzie and Karafolas [26]. Several applications of FBG sensors for spaceship monitoring were presented, including for an adaptive leg of a telescope structure, a smart flywheel support, elements of propulsion system inter-tank composite structure, and a thermal protection system.

Structural health monitoring systems based on embeddable piezoelectric active sensors are widely used for assessment of aeronautical, civil, and naval structures [27]. Although a considerable number of papers suggest the potential of such systems for health management of spacecraft, limited studies are available on piezoelectric sensing systems geared specifically towards space applications. A recent review on SHM for future space vehicles by Mancini et al. [28] focused on description of available technologies and their perspectives in the context of integration into vehicle's design process. Our literature survey indicates that practical use of piezoelectric SHM systems for space structures was considered primarily for monitoring the condition of the propulsion system, monitoring the condition of the thermal protection system (TPS), and assessing the integrity of bolted and adhesive structural joints.

Embedded ultrasonics for SHM of rocket engines was considered by Qing et al. [29]. Laboratory tests conducted by authors have shown the capability of the piezoelectric sensor network to detect surface and through-thickness cracks a few millimeters long. In the follow-up paper [30] the authors verified performance characteristics of piezoelectric sensors at cryogenic temperatures. Cuc et al. [7] presented application of several embedded ultrasonic SHM methods to monitoring of damage in simulated spacecraft panels. Pitch-catch, pulse echo, embedded ultrasonic structural radar (EUSR), and electro-mechanical impedance methods were considered. The results suggest applicability of these methods for detection of cracks, corrosion damage, and disbonding in aluminum panels. Availability of information on integrity of bolted joints is critical to many applications, including space structures. Monitoring of bolted joints is essential in enabling fast and fault-free assembly of satellites. Recent studies in this area include work of Clayton et al. [31], who considered guided waves with chaotic properties coupled with respective AR/ARX models, and Zagrai et al. [32], which has shown correlation between signal phase and the stress level in the joint.

Thermal protection systems typically have a structural assembly consisting of a carbon-carbon or ceramic panel connected to the base structure using a bracket with bolted joints.

TPS may fail due to excessive heating, high velocity impact, or fastener disintegration. Combination of these modes may result in a catastrophic event, such as the *Columbia* accident, where damage caused by foam impacting the leading edge of the wing, followed by excessive structural heating during re-entry. Because of its significance to reusable space vehicles, monitoring of TPS has received considerable attention. Yang and Chang [33] utilized a piezoelectric sensor network for detection of bolt loosening in TPS. Elastic wave energy and specific damping capacity (SDC) of structural elements were proposed as damage metrics for detection and location of weak joints. Experimental studies conducted by authors have shown the feasibility of the attenuation-based diagnostic for monitoring TPS integrity. Xie et al. [34] presented several validation experiments for monitoring TPS using a piezoelectric sensor network. The authors considered the effect of temperature on the elastic wave energy parameter. Yu [35] discussed application of piezoelectric sensors for detection of impacts on thermal protection panels. A specific algorithm for impact monitoring was reported and potential application of compact sub-node hardware was discussed. Na et al. [36] studied the effect of low energy impact on a different type of thermal protection system fabricated from gamma titanium aluminide honeycomb panels. Authors utilized a PVDF sensor to monitor impact levels and optical systems to assess damage severity.

3 METHODS, ASSUMPTIONS, AND PROCEDURES

3.1 Research Objectives/Goals

The goal of this research project is to develop an elastic wave methodology for structural health monitoring of satellites. An embeddable SHM system for satellite structural elements and joints is considered. In realizing this goal, the research team has focused on the following main objectives:

1. Development of an elastic wave SHM methodology for simple mechanical elements (e.g. beams and plates) of space structures. Consideration of bolted joints in space structures and exploration of mechanical changes in joints for assessment of structural integrity.

2. Exploration of applicability of the elastic wave SHM method to satellite structures of complex geometry. Investigation of method's functionality and limitations in complex structures.

In addition to the indicated major objectives, a range of optional topics were explored:

3. Exploration of a relationship between the elastic wave parameters and structural dynamic characteristics for model updating.

4. Consideration of statistical aspects in piezoelectric-based SHM of space structures.

3.2 Piezoelectric Sensing for Satellite SHM

Piezoelectric sensors are widely used in modern SHM systems [27]. Basic principles and applications of piezoelectric sensors for embedded ultrasonics are thoroughly covered in a number of textbooks, for example in [37]. It should be noted that piezoelectric sensors are utilized as active and passive elements of more than a few SHM techniques such as pulse-echo, pitch-catch, electromechanical impedance, acoustic emission, nonlinear ultrasonics, and others. Although these techniques monitor different signal parameters, all of them explore elastic wave propagation for assessment of structural integrity. To be measured by the piezoelectric sensor, the elastic wave must propagate through a structural element. Hence, if the accrued damage resulted in a variation in elastic properties, it could be detected by these SHM techniques.
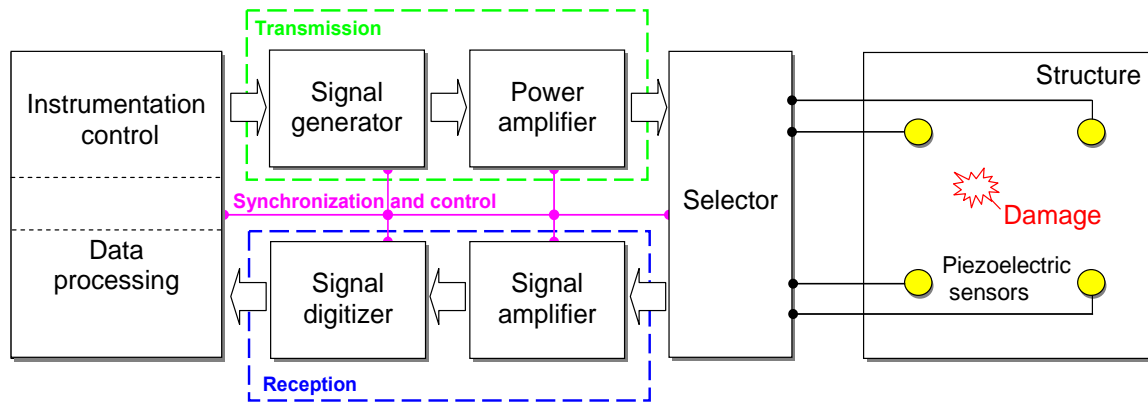
Figure 2   Instrumentation for piezoelectric sensing.

Hardware elements for a piezoelectric active sensing system are presented in the diagram in Figure 2. The computing unit controls the system, ensures synchronization of its elements, and stores the collected data. Parameters of the SHM system and its hardware, such as particular units, power requirements, accuracy of digitizers, or analog processing, significantly depend on SHM tasks. A broad spectrum of options is available, ranging from high power systems delivering kWs of power to custom-built low power embedded microcontroller configurations with data storage modules and radio data transmission. In the pre-launch testing, a system's weight and size may not be of critical concern, and high power instrumentation may be used. The on-board satellite SHM will likely consider an embedded system design with space hardened hardware. While degradation of electronic components in space may be addressed by proper selection of a system's elements, piezoelectric sensor performance in space is rather difficult to assess without environmental testing. A number of factors influence the operation of an SHM system in the space environment [38]:

- Temperature variation from -200 C^0 to +200 C^0 depending on orbital position of the spacecraft. However, this temperature range may be narrowed to -50 C^0 to +50 C^0 in shielded components.

- Neutral gases such as atomic oxygen can cause erosion of material and surface pitting.

- Ultraviolet radiation due to direct sunlight.

- Natural space radiation environment including radiation trapped in planet's magnetic field, galactic cosmic rays, solar wind and solar particle events.

- High vacuum (outgasing).

- Micro-meteorites and space debris.

The effect of the space environment on piezoelectric material (e.g. PVDF) is thoroughly described in [39]. The material performance and lifespan substantially depend on its composition and the orbit.

Bolted joints are among the most critical interfaces in space structures. Incorrect torque on a joint or a missing bolt may cause changes in the dynamic signature of the space structure and potentially lead to structural failure. For this reason, qualification of bolted joints during satellite assembly is an essential issue [40] which requires a careful consideration. It is envisioned [41] that integrity of satellite bolted joints can be assessed through structural health monitoring of satellite elements and the final assembly. Substantial research has been conducted on monitoring bolted joints with ultrasound [42-44]. However, prior investigations were focused on utilizing conventional ultrasonic transducers for assessing integrity of a single bolted joint. Embeddable piezoelectric wafer active sensors (PWAS) were explored in conjunction with the electro-mechanical impedance method also to monitor a single bolted joint [45]. Typical space structures include elements connected with hundreds, if not thousands, of bolts, and utilizing one transducer per joint is not practical. To address this issue an acousto-elastic embedded ultrasonic technique was developed that permits monitoring of considerable number of joints and a rather large structural area with a few embeddable PWAS [32]. The acousto-elastic technique is based on measuring local variation of the sound speed caused by changes in the stress condition of the bolted joint. In contrast to prior studies, an elastic wave is propagated through entire structure, not a single bolt, and this configuration allows for estimating location of a loose bolt based on the time of arrival of the elastic wave [46].

3.3 Theoretical Background on amplitude-phase signal analysis

Embedded ultrasonics structural health monitoring typically utilize amplitude or frequency as damage detection and discrimination features. In contrast, acousto-elastic detection of loose bolts put significant emphasis on phase information in the signal. Signal phase can be extracted from analytical signal x(t) using Hilbert transform

$$x(t) = Hilbert(s(t)) = \text{Re}(x(t)) + i \cdot \text{Im}(x(t))$$
(1)

where s(t) is the acquired sensor signal. Analytical signal x(t) can be presented in terms of real and imaginary parts or as amplitude and phase.

$$x(t) = \text{Re}(x(t)) + i \cdot \text{Im}(x(t)) = A(t) \cdot \exp(i \cdot \varphi(t))$$
(2)

Amplitude and phase in this case are determined in accordance with following formulations.

$$A(t) = |x(t)| = \sqrt{\text{Re}(x(t))^2 + \text{Im}(x(t))^2} \quad \varphi(t) = \tan^{-1}\left(\frac{\text{Im}(x(t))}{\text{Re}(x(t))} \right)$$
(3)

In the following development, we will use expressions above for calculating amplitude and phase of signals acquired in SHM experiments.

Another signal parameter, which is sometimes used in time frequency analysis, is instantaneous frequency defined as a time derivative of instantaneous phase in the preceding equation.

$$\omega(t) = \frac{d\varphi(t)}{dt}$$
(4)

All of the signal features indicated above are typically analyzed as a function of time. Some of the best known time-dependent analyses are time-frequency or time-scale distributions known as spectrogram and scalogram respectively. The first one is obtained using short time Fourier transform (STFT) and the second is determined through Wavelet analysis. Recently a new Hilbert-Huang Transform (HHT) has been suggested that, in contrast to Fourier and Wavelet transforms, is not constrained by stationary and linearity of the record as well as the Nyquist criterion [47]. Comparison between Fourier and HHT presentations is given below.

Fourier representation: data type - piecewise stationary, α and ω are constants.

$$X(t) = \sum_{j=1}^{\infty} a_j e^{i\omega_j t}$$
(5)

Hilbert-Huang representation: data type - stationary and non-stationary α and ω are functions of time.

$$X(t) = \sum_{j=1}^{n} a_j(t) \exp\left(i \int \omega_j(t)\, dt \right)$$
(6)

In HHT, an effective and original way of obtaining the instantaneous frequency distribution is to apply an Empirical Mode Decomposition (EMD) procedure developed by Dr. Norden Huang at NASA [47]. Diagram in Figure 3 illustrates step-by-step processing with HHT.

- Find max and min
- Interpolate (splines) upper and lower envelopes
- Calculate mean m1
- Subtract signal-m1 = IMF1; Do sifting?
- Subtract signal-IMF1 = IMF2; Do sifting?
- Subtract signal-IMF1-IMF2=IMF3; Do sifting?
- ....
                                    Flandrin *et al.*
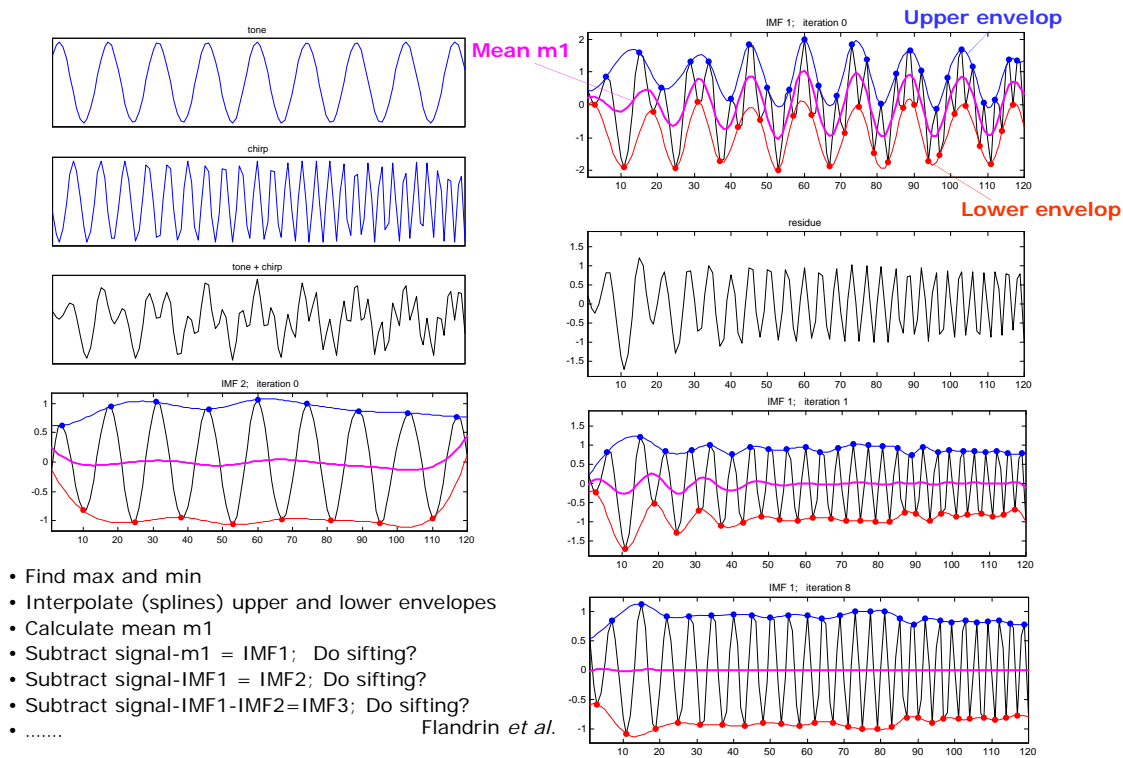
Figure 3   HHT procedure for signal processing. http://perso.ens-lyon.fr/patrick.flandrin/emd.html
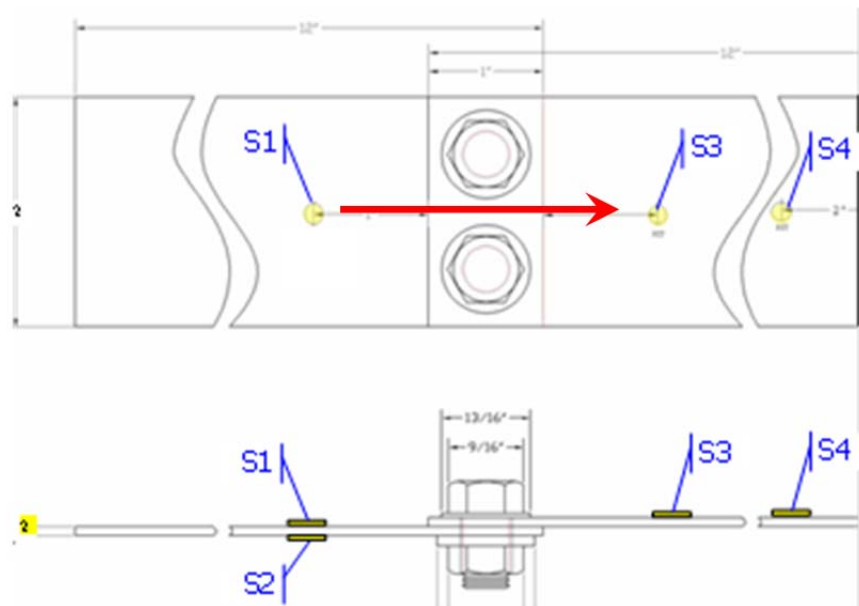
Figure 4   A simple bolted joint used in analysis of the acousto-elastic signals.

Signal processing for diagnosis of structural joints in simple specimens

The discussed signal processing approaches were first applied to a bolted joint specimen of simple geometry. Data for the specimen indicated below was available at different torque level, which allowed correlation of performance of signal processing approaches in detection of loose bolts. Below we present brief description of experiment, signal processing of elastic waveforms and analysis of signal features sensitive to stress levels exerted by bolts.

A brief description of the experiment is given below.

■ Experimental specimen was fabricated from thin aluminum 2024-T3 plates (12" x 2" x 0.08") bolted with two 3/8-16 grade 8 hex flange screws, and accompanying 3/8-16 UNC flange nuts.

■ Bolts were torqued with a torque wrench to specified levels (see figures).

(a)

(b)
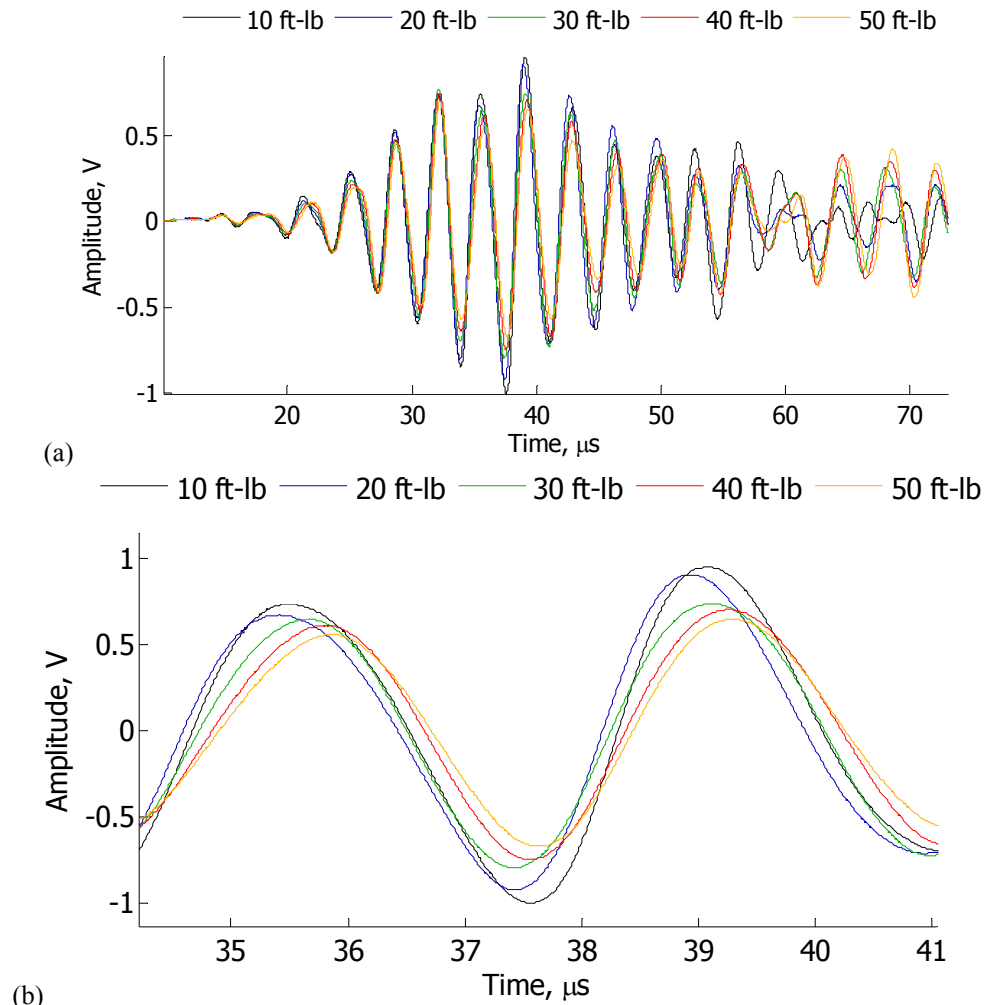
Figure 5   Elastic wave signals of a bolted joint under different torque conditions on the bolts. (a) full-length record, (b) zoom-in portion.

As it could be seen from figures above, changing the bolt torque causes elastic wave amplitude change and a shift in signal phase .To quantify these changes, we apply expressions presented above and plot results in Figure 6.
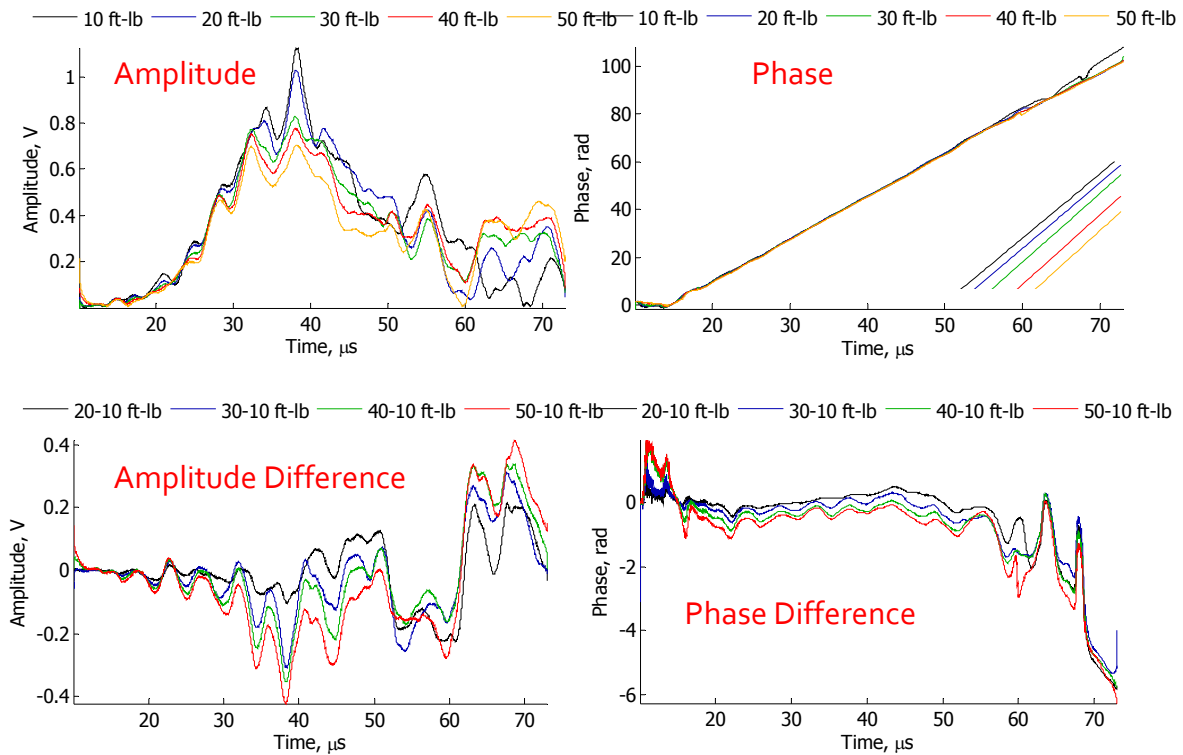
Figure 6   Amplitude and phase dependencies calculated for elastic wave signals propagated through a bolted joint subjected to indicated levels of torque.

Figure 6 gives much clearer picture on variation of amplitude and phase due to applied torque. In contrast to phase, amplitude shows less stable behavior (although larger changes) with amplitude difference changing in the first and the second portion of the signal. Phase change for the main pulse is very stable with vertical deviation indicating magnitude of the phase shift at different torque levels. Progressive shift downwards is observed for the whole pulse as torque on both bolts increases. An oscillatory variation of phase in the main pulse indicates nonlinear behavior, which increases under high torque levels and then stabilizes.

A traditional approach to evaluating time-dependent nonlinear effects would be calculating spectrograms at each torque condition. This was done for signals presented above and spectrograms are presented in Figure 7.

As it can be seen from the figure, increased level of the second harmonic is observed at increasing torques. However, manifestation suffers from limitations of short-time Fourier transform (signal stationarity and time vs. frequency resolution) and therefore other time-frequency distributions are sought to improve manifestation of nonlinear effects. In particular, Hilbert-Huang transform (HHT) is suggested as described in preceding section. An example of signal processing using HHT is presented in Figure 8 and Figure 9. The

signal is essentially decomposed in a number of empirical modes that accept Hilbert transform and can be represented in a time-frequency plane as illustrated in Figure 9.
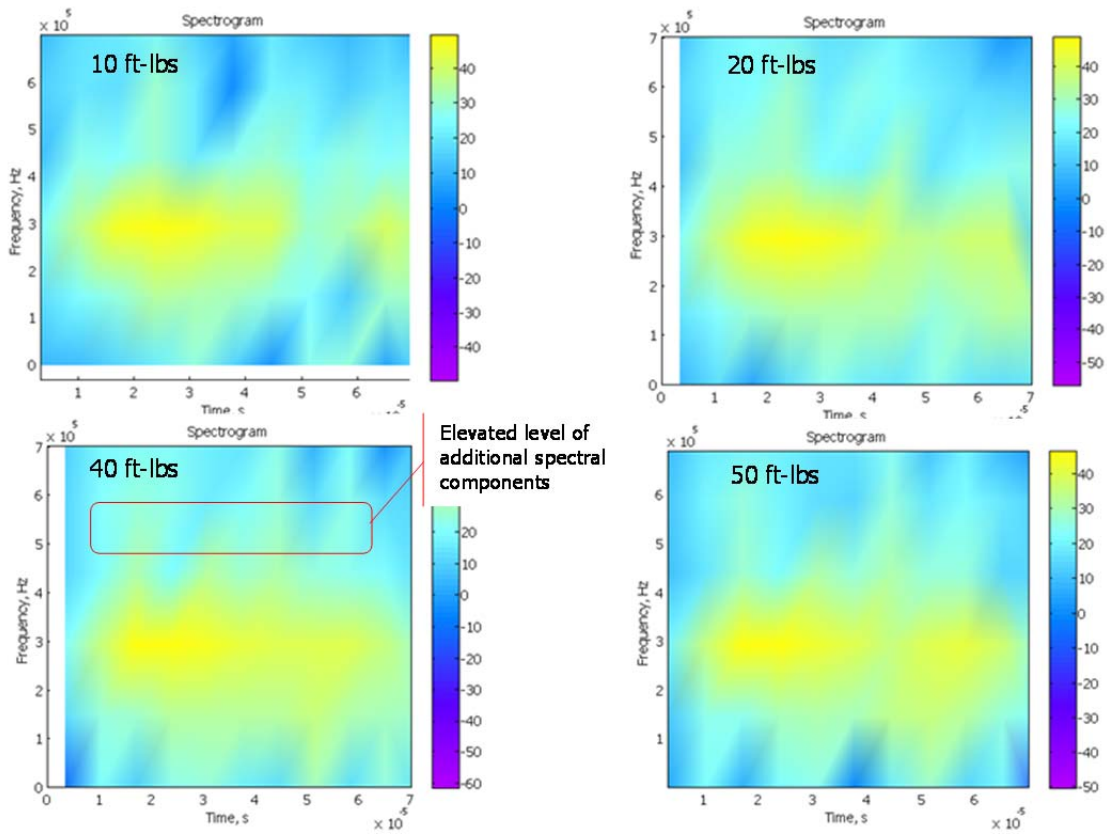
Figure 7   Spectrograms of elastic wave signals propagated through a bolted joint subjected to levels of torque as indicated.

Often, the decomposed intrinsic mode functions - imf (e.g. depicted in Figure 8) of Hilbert-Huang transform have physical meaning. Although this statement may not be proved theoretically, at least the first imf in Figure 8 should include an effect of torque on the elastic wave signal. Indeed we see that at the fundamental frequency of around 300 kHz oscillations of the instantaneous frequency (Eq. 4) indicate nonlinear effects associated with torque on a bolted joint. In general, amplitude of these oscillations tend to increase as applied torque increases, but stability and repeatability of this increase is questionable as slight signal deviations may have a profound effect on empirical (i.e. not theoretical functions) mode decomposition. In other words, the detection of torque suffers from general instabilities of the HHT processing. Therefore, for future investigations, we selected amplitude-phase analysis which produced instantaneous signal features with much more clear visual manifestation and analytical presentation.
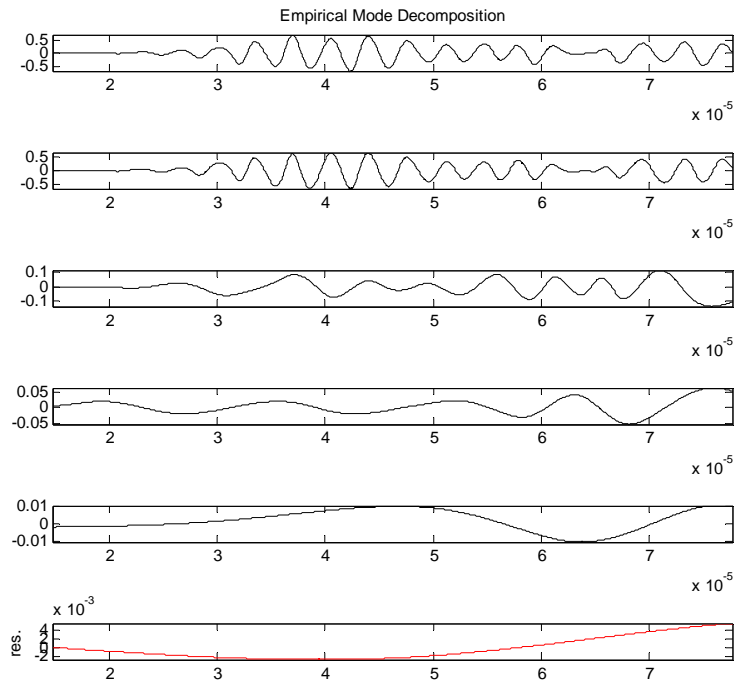
Figure 8   Empirical mode decomposition of elastic wave signal from the bolted joint.
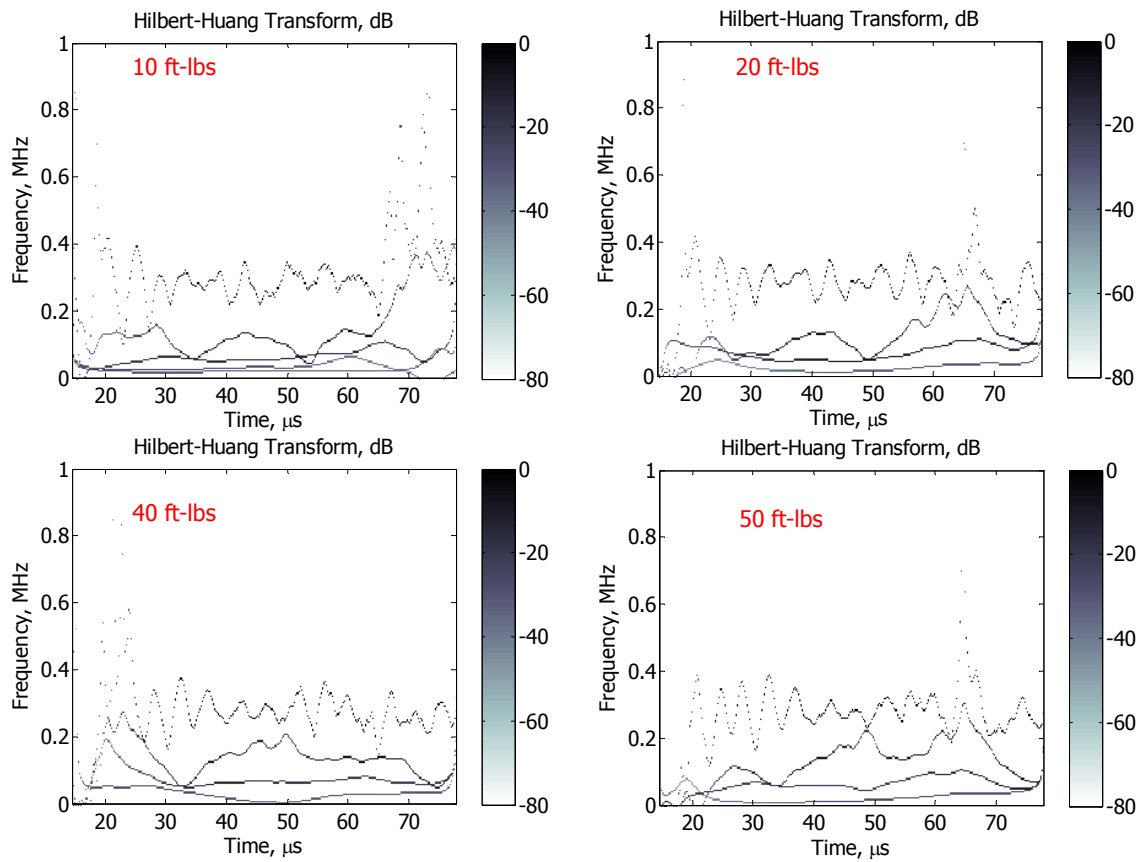
Figure 9   Hilbert-Huang transform elastic wave signals at various torque conditions.

4   RESULTS AND DISCUSSION

4.1   Acousto-elastic Measurements in Thin plates

It is known that the sound speed of the ultrasonic wave depends on stress condition in the elastic material [48]. This effect is a foundation of acousto-elasticity, which is used to determine the third order material constants or evaluate stresses in structural components. The relationship between the sound speed and the applied stress is determined by mutual orientation of the stress vector and direction of the wave propagation as well as structural geometry, boundary conditions, and constitutive material.

$$\rho c^2 = E_1 + \sigma \cdot E_2 \tag{7}$$

In the expression above, c signifies sound speeds of various types (e.g. longitudinal, shear, etc.) that in general may be frequency dependent. E_1 includes a combination of linear elastic components, and E_2 is a combination of linear and nonlinear elastic components. Equation (7) reflects a general principle of the acousto-elasticity, and actual formulations for each sound speed may be obtained for particular wave propagation settings [49]. The objective of this study is to investigate experimentally changes in velocities of symmetric and anti-symmetric Lamb waves propagating in thin aluminum plates. Consideration of the effect of the applied stress on the elastic wave propagation in thin plates is necessary because the condition of the bolted joint depends on stresses in structural material adjacent the bolt.

4.1.1   Experimental Samples and Test Setup

A series of acousto-elastic tests were conducted to determine sound speed of Lamb waves in a thin aluminum plate subjected to increasing levels of tensile loads. The aim of the tests was to develop fundamental understanding of the acousto-elastic response of the stressed aluminum plates.
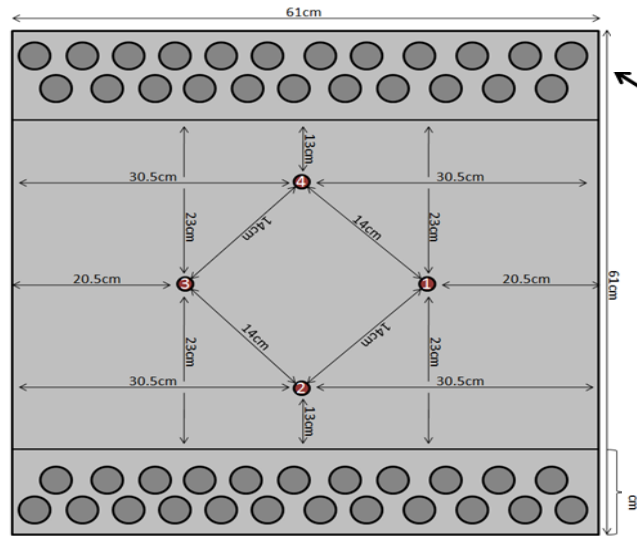
Figure 10 Geometry and sensor layout of the aluminum plate subjected to tensile loads.

An experimental specimen—1 millimeter thick aluminum 6061 plate— is illustrated in Figure 10. The figure provides the geometry of the plate and the sensor layout. Special steel grips were fabricated and installed into the test area of the MTS Landmark tensile machine to permit uniform stress distribution in the plate. To monitor the effect of the applied stress on the sound speed, piezoelectric wafer active sensors (PWAS) were positioned in the cross pattern on the plate as presented in Figure 10. Equipment and general settings for the acousto-elastic test are depicted in Figure 11. The sensors were made from APC-851 piezoelectric ceramic disks with diameter of 7mm and thickness 0.25 mm. In the experiment, through-transmission signals between sensor pairs S1-S3, S2-S4, S3-S1, S3-S2, S4-S1, and S4-S2 were recorded with the NI 5142 16 bit high speed digitizer and analyzed to infer sound speeds. The elastic wave signals were measured at 5 different frequencies with a 50 kHz increment: 300 kHz, 350 kHz, 400 kHz, 450 kHz, and 500 kHz. First, the elastic wave signals were acquired in the free-free condition of the plate implemented by placing the plate on foam. Then, the plate was installed in the load frame and signals from the same sensors were acquired under no-load condition. Subsequently, the loads of 5, 10, 15, 20, 25, 30, 35, and 40 kN were applied, and the elastic waveforms corresponding to these stress levels were measured. It needs to be mentioned that in this tensile test the plate was completely unloaded after each stress increment; i.e. each load increment started with 0 kN and then reached the designated value.
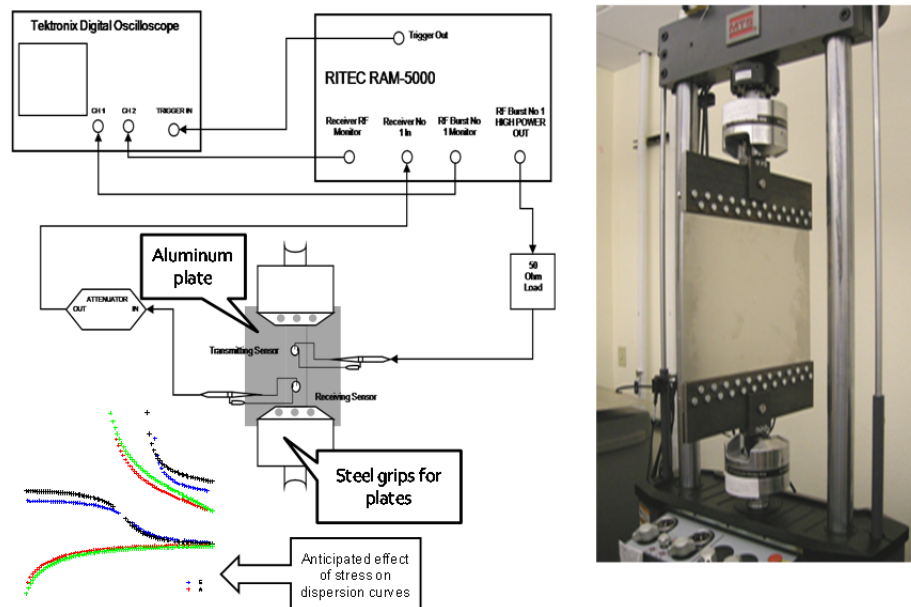
Figure 11 Equipment utilized in the acousto-elastic test.
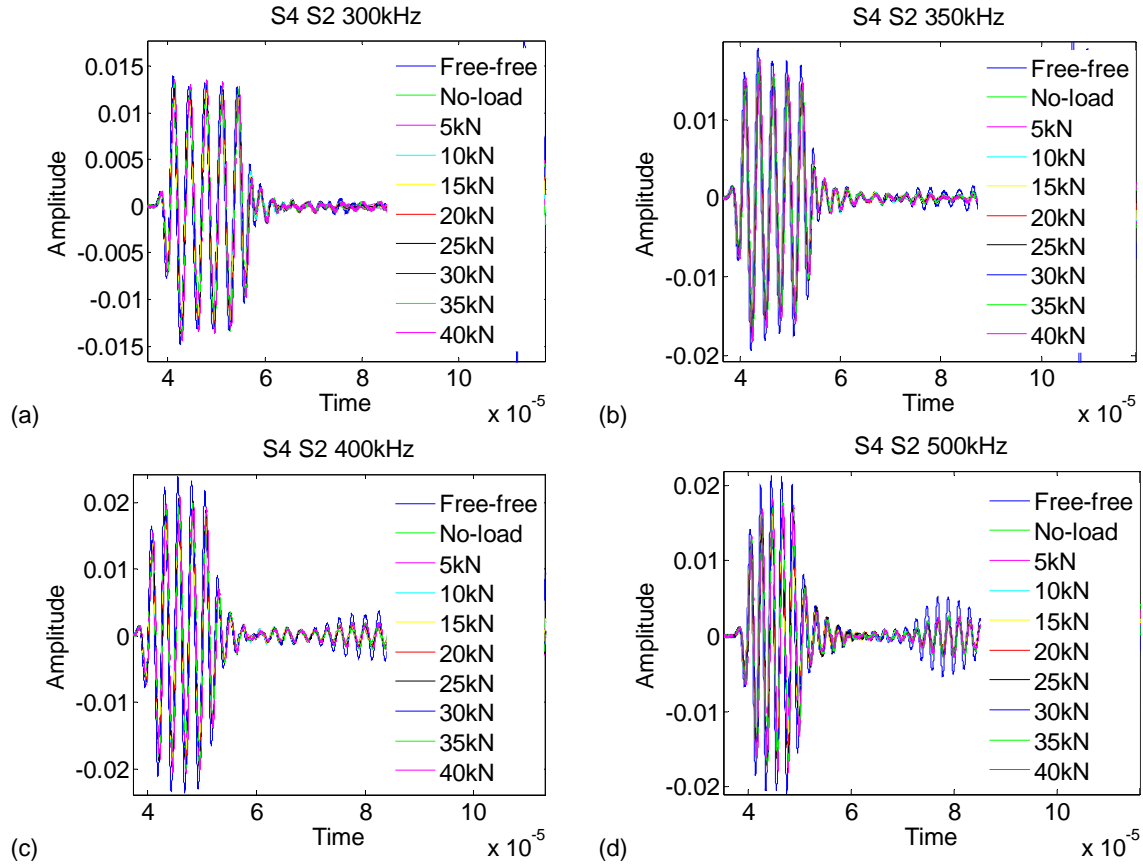
Figure 12 Ultrasonic signals obtained with sensor pair S4 (transmitter) - S2 (receiver) for various load conditions and four excitation frequencies: (a) 300 kHz, (b) 350 kHz, (c) 400 kHz, (d) 500 kHz.
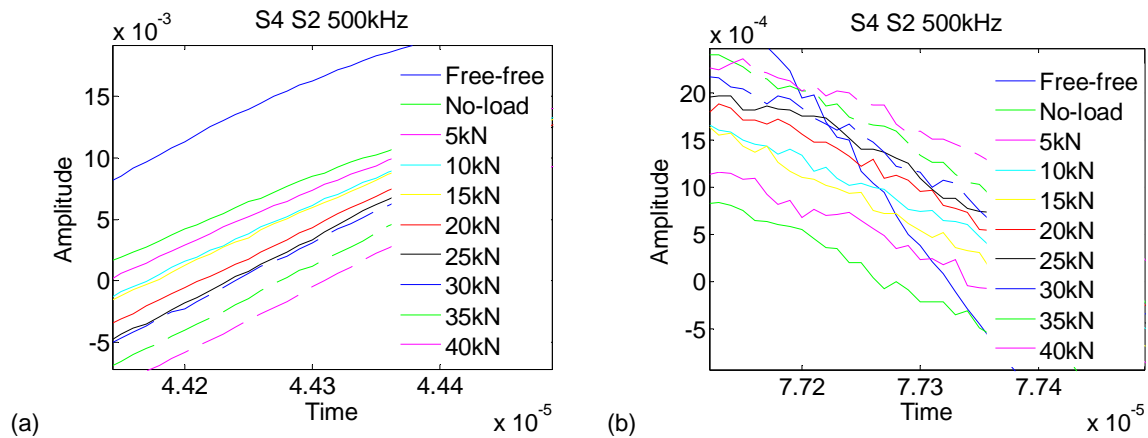
Figure 13 Details of the S4-S2 acousto-elastic response at 500 kHz: (a) S_0 mode, (b) A_0 mode.
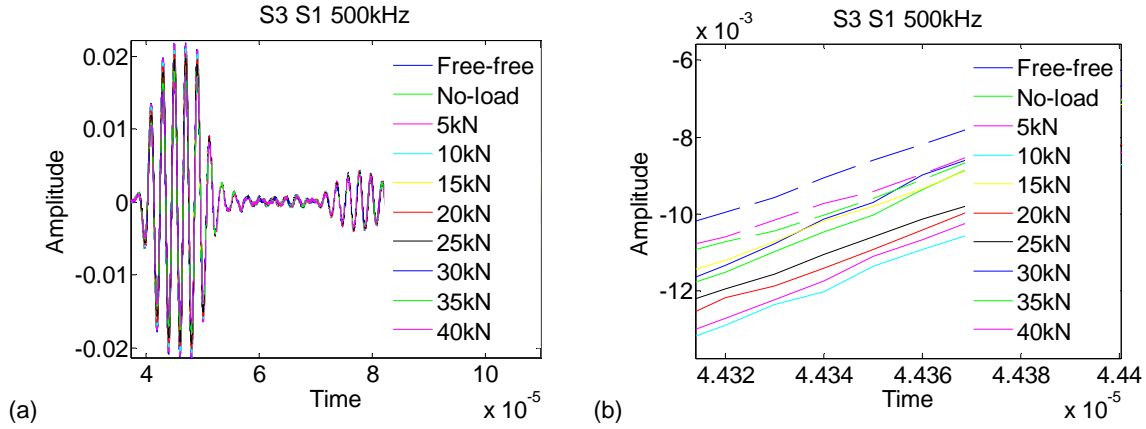
Figure 14 Acousto-elastic response of the sensor pair S3-S1 at 500 kHz: (a) signal records at various load conditions, (b) details of S_0 mode.
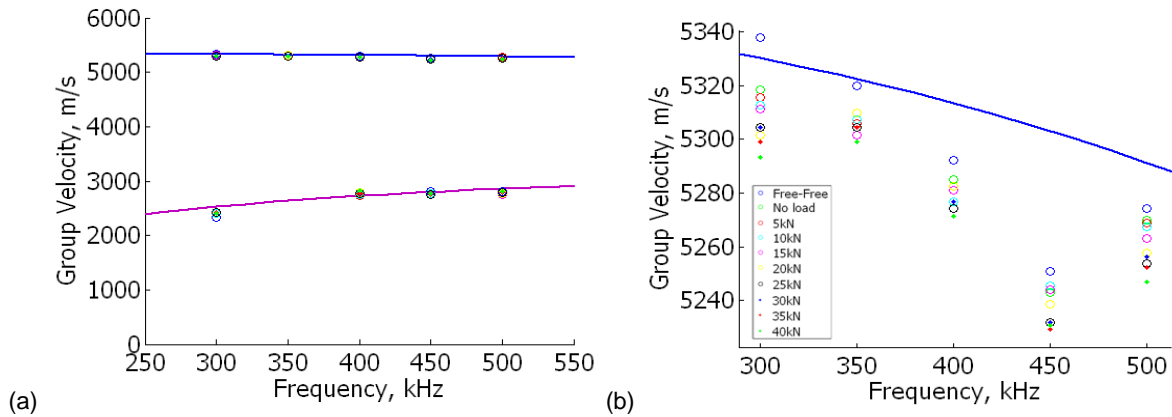
Figure 15 Theoretical (solid lines) and experimental (points) sound speeds extracted using the cross-correlation method: (a) dispersion curves, (b) details of the S_0 mode dispersion.

4.1.2   Results of the Acousto-Elastic Test

Examples of the elastic waveform recorded during the tensile test are presented in Figure 13. This figure illustrates the effect of static stress on the elastic wave propagating in the direction of the applied stress. The records obtained for several excitation frequencies show changes in the signal arrival due to the load. The first pulse in the record corresponds to the S_0 wave propagation mode and the second, smaller, pulse is the A_0 mode. It is interesting to note that A_0 is not excitable at all frequencies as predicted by Giurgiutiu (2005) [50] and contributes at frequencies above 400 kHz. The signal delay due to applied stress is observed at all frequencies and in both S_0 and A_0 ultrasonic pulses. Details of the signal delay due to applied load are illustrated in Figure 13. The S_0 mode shows a consistent signal time delay at increasing loads. Higher load causes the larger the time delay. The difference between "no-load" and "40 kN" is the time delta of $\Delta_1 = 22 \cdot 10^{-8}$ seconds. It is evident that propagation of the S_0 mode depends on the static stress level and the time delay correlates very well with the magnitude of applied load. A comparable behavior was observed for the A_0 guided wave mode. From Figure 12d one may observe that amplitude of the A_0 pulse is noticeably lower than the S_0 pulse. As a result, contribution of noise is much more noticeable in the A_0 wave

as illustrated in Figure 13b. Although the A_0 mode shows notable correlation between the applied load and the A_0 pulse delay, the stability of results is less obvious than in the S_0 case.

When the elastic wave is propagated in the direction perpendicular to the applied load, the acousto-elastic effect is much less pronounced for both S_0 and A_0 modes. Figure 14 illustrates the acousto-elastic response of the sensor pair S3-S4 representative of this experimental scenario. From this figure, it is difficult to infer dependence of the pulse delay on the level of the applied load although smaller delays are noticeable for high loads and larger delays are observable for comparatively low loads. It should be noted that the time delta between extreme conditions in Figure 14b is $\Delta_2 = 6 \cdot 10^{-8}$ seconds, which is three times smaller than Δ_1 obtained for elastic waves propagating in the direction parallel to the applied load.

Figure 13 suggests consistent decrease of sound speed at increasing levels of the applied load. To evaluate changes in sound speed due to the applied loads, we utilized a well known correlation method [16] in which a sound speed is calculated from position of maximums of Hilbert envelopes of a cross correlation function of transmitted and received signals. The results of such evaluation are presented in Figure 15 along with the theoretically calculated dispersion curves. A zoomed-in portion of the dispersion curve showing details of a downward shift of the sound speed for S_0 guided wave mode is given in Figure 15b. Although a downward shift of the sound speed at increasing stress levels is apparent in Figure 15b, it is not as consistent as Figure 13a implies. The reason for this discrepancy is that the cross-correlation procedure alters the shape of the elastic wave pulse and generally would produce less accurate results than the phase comparison methods. The majority of phase methods, however, utilize non-dispersive signals and further considerations are needed to apply such detection schemes to dispersive waves.

4.1.3   *Numerical modeling of acousto-elastic effects*

4.1.3.1.   Theoretical Considerations

Development of reliable methodologies for damage detection in complex structures requires thorough understanding of wave dynamics in components subjected to local stress variation. To date, theoretical developments in acousto-elasticity were focused on bulk wave propagation in infinite medium subjected to particularly oriented stress.

$$\rho \frac{\partial^2 u_i}{\partial t^2} - \mu \frac{\partial^2 u_i}{\partial x_k^2} - \left(K + \frac{\mu}{3} \right) \frac{\partial^2 u_l}{\partial x_l \partial x_i} = F_i \tag{8}$$

and

$$F_i = \left(\mu + \frac{A}{4}\right)\left(\frac{\partial^2 u_l}{\partial x_k^2}\frac{\partial u_l}{\partial x_i} + \frac{\partial^2 u_l}{\partial x_k^2}\frac{\partial u_i}{\partial x_l} + 2\frac{\partial^2 u_i}{\partial x_l \partial x_k}\frac{\partial u_l}{\partial x_k}\right) +$$
$$+\left(K + \frac{\mu}{3} + \frac{A}{4} + B\right)\left(\frac{\partial^2 u_l}{\partial x_i \partial x_k}\frac{\partial u_l}{\partial x_k} + \frac{\partial^2 u_k}{\partial x_i \partial x_k}\frac{\partial u_i}{\partial x_l}\right) +$$
$$+\left(K - \frac{2\cdot\mu}{3} + B\right)\frac{\partial^2 u_i}{\partial x_k^2}\frac{\partial u_l}{\partial x_l} + \left(\frac{A}{4} + B\right)\left(\frac{\partial^2 u_k}{\partial x_i \partial x_k}\frac{\partial u_l}{\partial x_i} + \frac{\partial^2 u_l}{\partial x_i \partial x_k}\frac{\partial u_k}{\partial x_l}\right) +$$
$$+\left(B + 2C\right)\frac{\partial^2 u_k}{\partial x_i \partial x_k}\frac{\partial u_l}{\partial x_l}$$

(9)

In the equation above where u_i, u_l are components of a strain tensor $u_{ik} = \frac{1}{2}\left(\frac{\partial u_i}{\partial x_k} + \frac{\partial u_k}{\partial x_i} + \frac{\partial u_l}{\partial x_i}\frac{\partial u_l}{\partial x_k}\right)$, μ is a shear modulus and K is bulk modulus of elastic solid.

Nonlinear effects are modeled using a volumetric force term F_i, which includes third-order nonlinear parameters A, B, and C. Alternative models may be developed using a set of Murnaghan indexes, l, m, n, which account for nonlinear acoustic effects and have a direct correspondence with nonlinear parameters A, B, and C. Steady state variant of Eq. (1) is

$$-\rho\omega^2\mathbf{u} - \nabla\sigma = \mathbf{F}v \tag{10}$$

and stress

$$\sigma = \left(\mathbf{s}\cdot(\mathbf{I} + \nabla\mathbf{u})\right), \quad -i\omega = \lambda \tag{11}$$

where

$$\mathbf{s} = \frac{\partial W_s}{\partial \epsilon} \quad W_s = \tfrac{1}{2}(\lambda + 2\mu)\left(I_1^\epsilon\right)^2 - 2\mu I_2^\epsilon + \tfrac{1}{3}(l + 2m)\left(I_1^\epsilon\right)^3 - 2m I_1^\epsilon I_2^\epsilon + n I_3^\epsilon$$

(12)

is the strain energy function for hyper-elastic material. The strain is

$$\epsilon = \tfrac{1}{2}\left[(\nabla\mathbf{u})^\mathsf{T} + \nabla\mathbf{u} + (\nabla\mathbf{u})^\mathsf{T}\nabla\mathbf{u}\right]$$

(13)

Lame elastic moduli

$$\mu = \frac{E}{2(1 + v)}, \qquad \lambda = \frac{Ev}{(1 + v)(1 - 2v)} = \kappa - \frac{2}{3}\mu$$

(14)

Due to complexity of the analytical solution, our efforts were directed to numerical modeling using the above mentioned equations.

Comsol® package allows for modeling of hyper-elastic material and incorporation of nonlinear effects via Murnaghan indexes. Our approach involves modeling of the pre-stressed state first and then accounting for acousto-elastic effect using new state of stress and hyper-elastic material. Since Murnaghan expansion describes nonlinear material behavior using third order constants (indexes), wave propagation modeling using typical linear material must be considered first and compared to different material models.

4.1.3.2.   Numerical model for linear elastic wave propagation

A simple structure – a thin aluminum plate was considered and model parameters such as numerical damping, elastic wave frequency, finite element size and distribution were investigated.

The model illustrated in Figure 16, assumes a thin aluminum plate in 2D geometry and plane strain condition. The plate is 0.3 meters long and 0.0011 meters thick. A 3 count excitation is appllied via elastic force acting on the surface, close to the end of the beam. Time-dependent solver with unity of numerical damping was utilized in all studies.
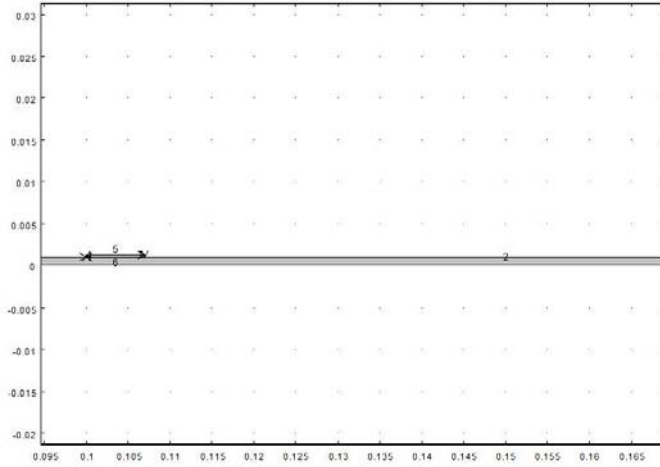
Figure 16 2-D model of the wave propagation in thin aluminum plate

The first mesh consisted of free triangular elements and no refinements were made. One parameter for creating a mesh is the resolution for thin areas. This was applied across thin portion of the plate. The first mesh had a resolution of 1 element across the thin area. The next two meshes presented below have no refinments but the resolution was changed to 2 and 4 elements per thig region for each case. The last three meshes presented are the ones which result from refining the first mesh. Subsequent refinements are labeled as 1, 2 and 3 refinements. On the current PC, issues due to limited computer memory were noticed and no further refinements were possible while modeling using current hardware. Each modification of the mesh resulted in differet element size and elements per plate thicknes as shown in Table 1.

Table 1   Finite element sizes resulted from mesh adjustments.

	element size (m)	elements thick
no refinements	0.0015	1
no refinements resolution 2	0.00078	2
no refinements resolution 4	0.00037	4
1 refinement	0.00072	2
2 refinements	0.00039	4
3 refinements	0.0001919	8

Numerical studies were conducted at two frequencies f1=200 kHz and f2=500 kHz. Assuming sound speed for symmentric S0=5350 m/s, and anisymmetric A0=2900 m/s modes, we arrive to λ_{S0f1}= 0.0267 m, λ_{S0f2}= 0.0107 m, λ_{A0f1}= 0.0145 m, λ_{A0f2}= 0.0058 m.
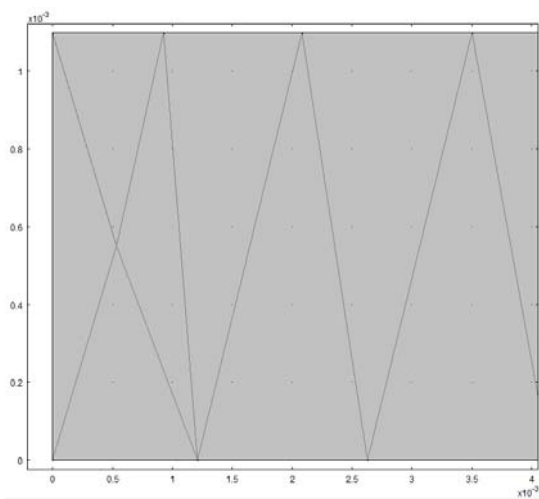
(a) No refinements
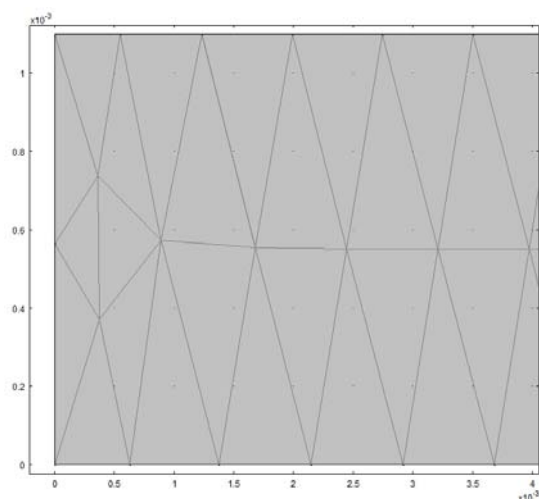
(b) No refinements-resolution 2 thick
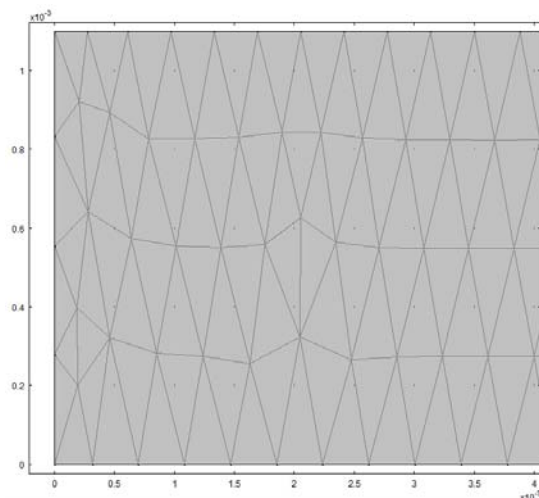
(c) No refinements-resolution 4 thick
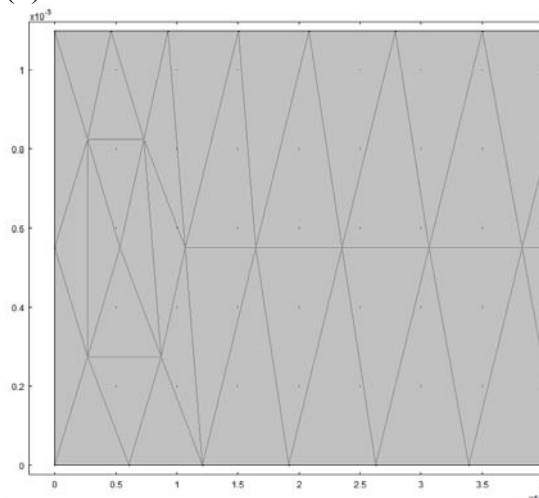
(d) 1 refinement
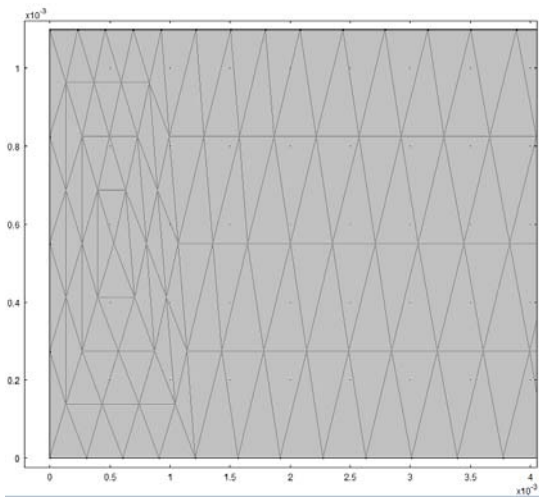
(e) 2 refinements
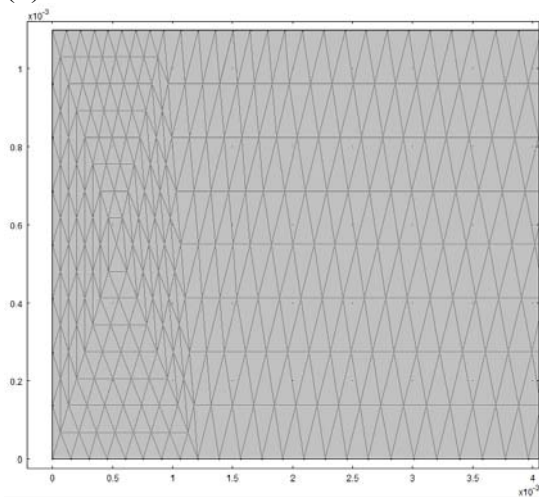
(f) 3 refinements

Figure 17 Various meshes used in the numerical study.
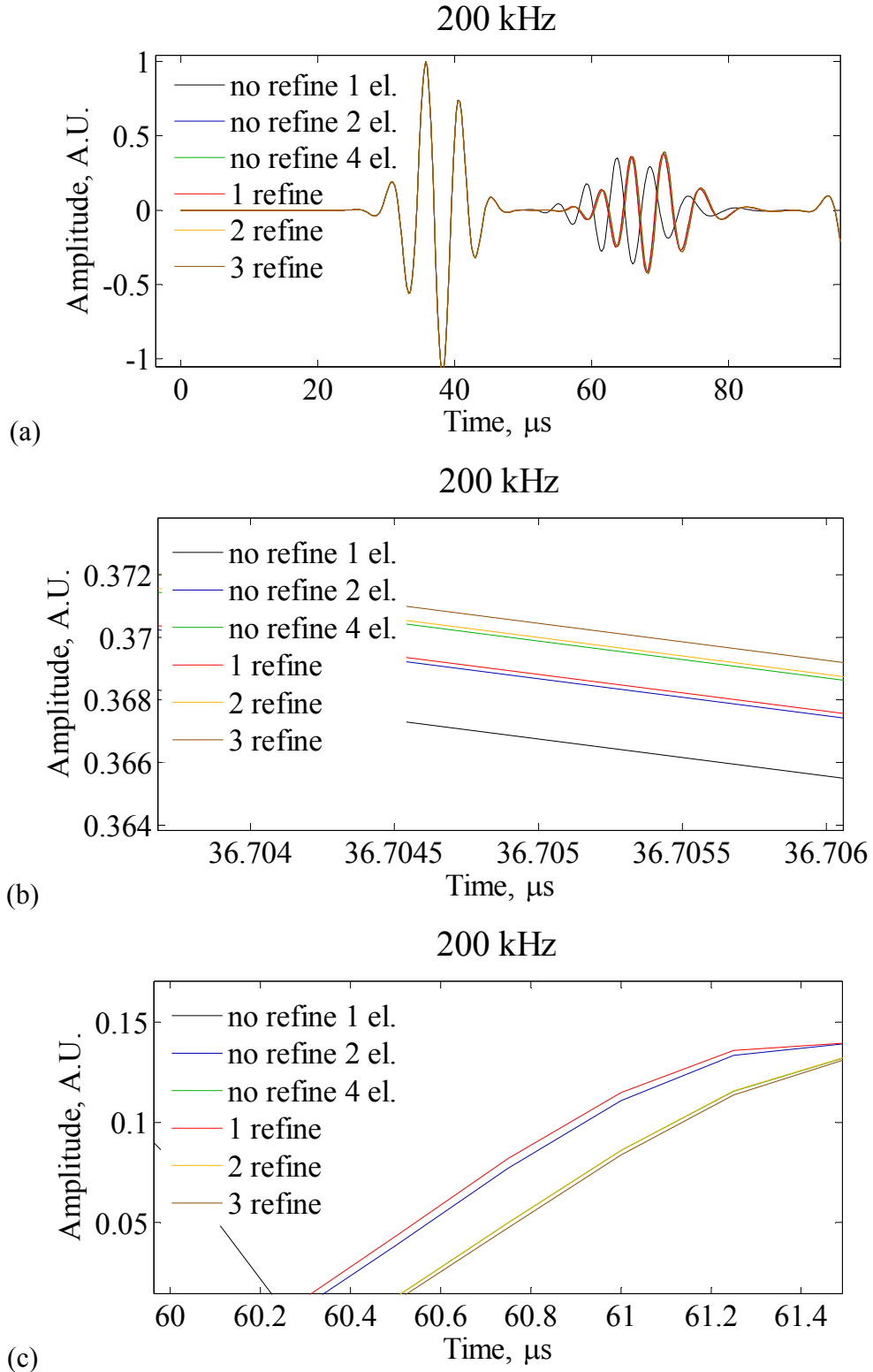
Figure 18 Results of finite element modeling of 200 kHz elastic wave pulse propagating in a thin plate: (a) simulated signal, (b) close-up on a S0 component, (c) close-up on A0 component.

This suggests about 10 to 20 elements per wavelength for 200 kHz pulse and less than 10, (actually 9.66) to 3.7 for 500 kHz. Clearly 200 kHz pulse is at the limit of proper settings and 500 kHz pulse is noticeably below this requirement especially for A0 mode. For proper wave reconstruction, a typically suggested number per elastic wavelength is 20.

Figure 18 illustrates a typical record obtained as a result of a numerical model for 200 kHz pulse. Very low variability of data for different number of elements and degrees of refinement is observed for first S0 pulse (figure a). For the S0 mode, a phase difference signals obtained with coarse and the finest meshes reaches $\Delta S1=0.0025$ micro seconds. The difference between the finest mesh and a refinement just below the finest mesh is $\Delta S2=2.9372e-004$ micro seconds. Interestingly, 1 element per thickness substantially impacts manifestation of A0 mode which is almost 90 degrees out of phase with data obtained for finer meshes. One needs at least 2 elements per plate thickness or refinement to adequately represent the wave propagation at 200 kHz. For an A mode, the difference between the finest mesh and a refinement just below the finest mesh is $\Delta A1=0.0141$ micro seconds.

A distinctly different situation occurs when a 500 kHz pulse is used. The difference between coarse and fine meshes in this case reaches $\Delta S3=0.0067$ micro seconds; and the difference between very fine and the fines meshes $\Delta S4=2.1467e-004$ micro-seconds. The antisymmetric A mode exhibits substantial variability and for best meshes reaches $\Delta A2=0.0422$ micro seconds.

It should be mentioned that experimental studies have shown that the difference between "no-load" and "40 kN" structural conditions evaluated with piezoelectric sensors, are $\Delta 1=0.22$ micro-seconds for elastic wave propagating parallel to the allied stress and $\Delta 2=0.06$ micro-seconds for elastic wave propagating perpendicular to the load. Therefore, for 200 kHz S0 and A0 pulses the mesh gives variability at least an order of magnitude less than observed in acousto-elastic experiments. A 200 kHz model may be used in the acousto-elastic models. However, for 500 kHz data, variability is slightly more than an order of magnitude of the acousto-elastic effect. And using such a frequency for acousto-elastic numerical studies in the current model is questionable.

Another aspect of the numerical modeling is a number of time instants produced by a numerical solver per one wavelength. This is similar to a sample rate in signal processing. If the number of samples is small, than a minuscule phase shift may not be noticed or detected. Figure 19Figure 20 illustrates that a waveform for 200 kHz shows around 21 samples per period and 500 kHz presents only 9 samples per period. Even more, Figure 20 suggests very coarse sampling for A0 mode. Such a sampling may be considered for a linear measurement scheme with a finite element model using refined meshes, but it is not adequate for nonlinear measurements, including acousto-elasticity. Therefore, models with refined meshes and with pulse of 200 kHz and below are recommended.

(a)

(b)

(c)
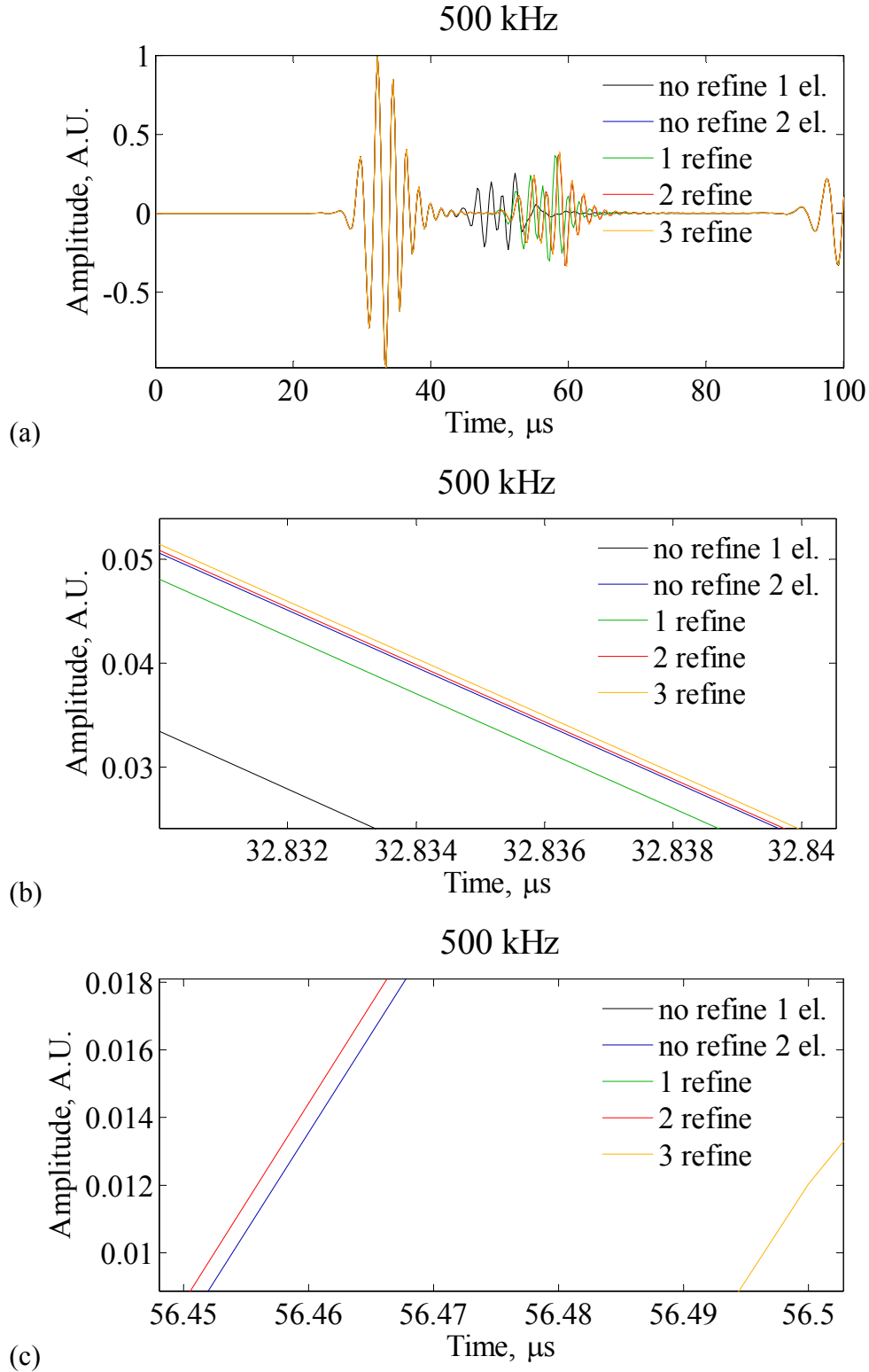
Figure 19 Results of finite element modeling of 500 kHz elastic wave pulse propagating in a thin plate: (a) simulated signal, (b) close-up on a S0 component, (c) close-up on A0 component.
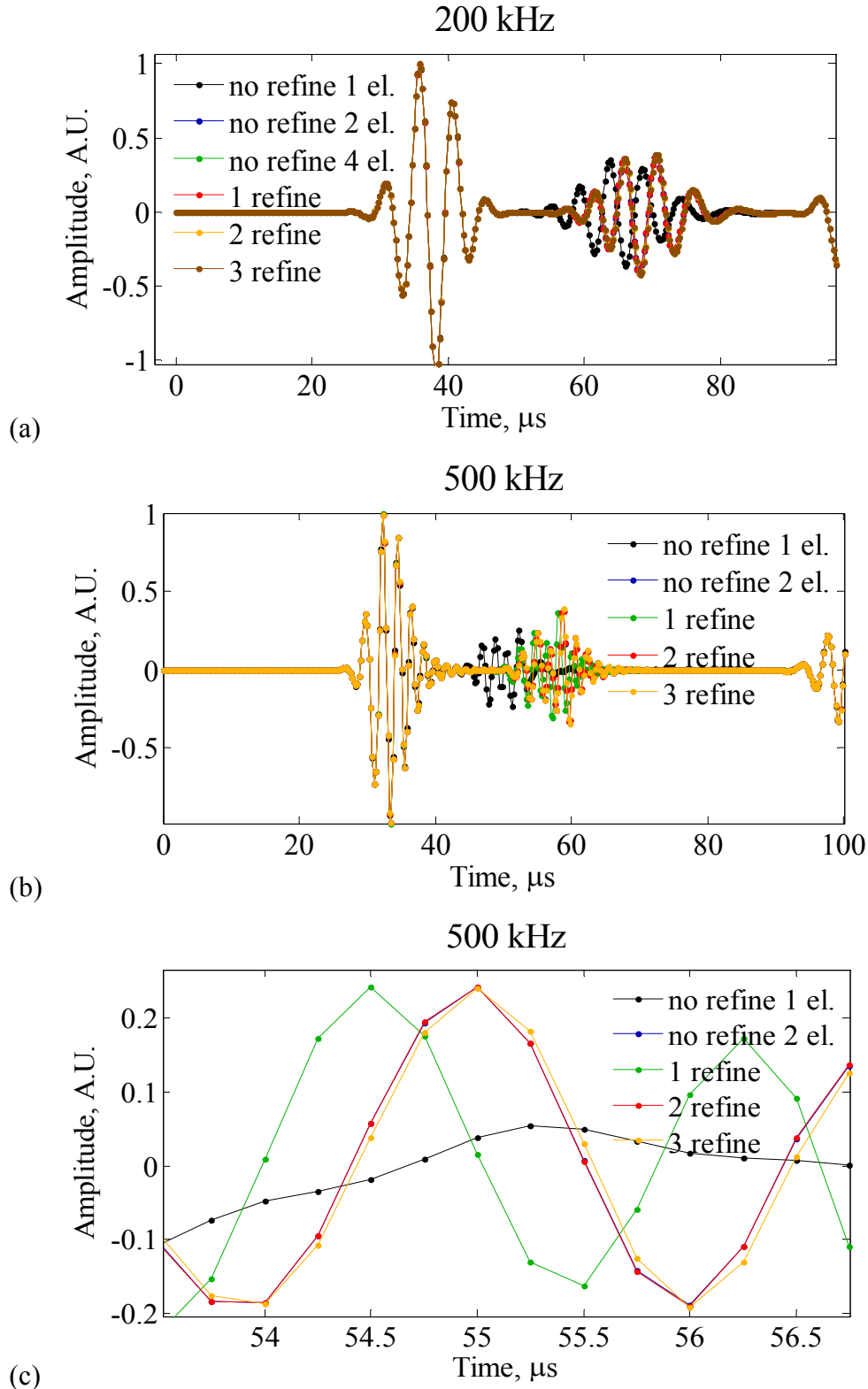
Figure 20 Examples of sampling for numerically modeled elastic wave signals in a thin plate: (a) 200 kHz signal, (b) 500 kHz signal, (c) close-up on A0 component of 500 kHz signal.

It is interesting to note that initial Comsol numerical modeling of wave propagation in thin plates produced noticeable discrepancy between experimental, analytical and numerical data. Improvements in modeling were not possible initially due to lack of computing resources and PC performance. To mitigate this issue, a high-speed PC dedicated to numerical analysis was acquired and models were refined. Our efforts allowed us to overcome previous limitations of Comsol modeling of guided wave propagation. Simulations were run for input frequencies from 100 to 600kHz in 100kHz increments. The old and new Comsol simulation results are presented in Table 2. Illustration in Figure 21 reveals each Comsol model versus the theoretical dispersion curve for the S0 mode and suggests adequate matching of numerical and analytical models.

Table 2 Wave Speeds for S0 modes in Comsol

Frequency (kHz)	Comsol S0 (old)	Comsol S0 (new)
100	5216	5506
200	5111	5363
300	4960.8	5373
400	4729	5356
500	4720	5345
600	4583	5353
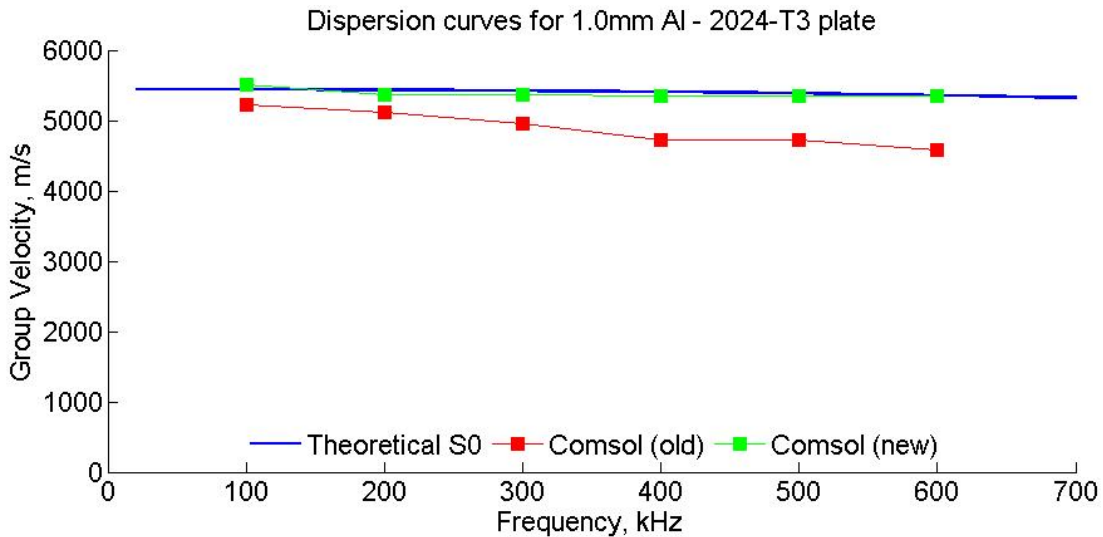
Figure 21 Dispersion curves obtained with theoretical (analytical), old and new numerical models.

4.2 Acousto-elastic Assessment of Bolted Plates

Figure 22 Load washer, www.omega.com.

In order to develop fundamental understanding of the acousto-elastic behavior of bolted thin-walled structures and application of the acousto-elasticity for detection of loosened bolts, a set of experiments with bolted thin plates were conducted. In complex structures, a typical interface assessment scenario would consist of finding one loosened bolt among many properly tightened bolts. To accommodate for this condition, a specimen consisting of two aluminum 6061 plates (thickness 2.42mm) joined with a row of 12 bolts was considered (Figure 23).

Table 3 Torque levels exerted by the torque wrench and corresponding axial loads measured by the load cell.

Torque (ft-lb$_f$)	Measured Axial Load (lb$_f$)
0	0
15	2125
20	2840
25	3725
30	4566
35	5000

In the acousto-elastic tests, it is important to know the stress exerted on the structure by the bolted joint. To our opinion, devices allowing for setting a certain torque and applying it to the bolt may not be accurate enough to indicate the actual stress exerted by the bolt. For this reason, s particular device – load washer was considered for measurement of stress in the joint. A washer-type load cell was purchased, installed and calibrated to facilitate measurement of the actual stress in the structure exerted by a single bolt. The Omegadyne LCWD-5k depicted in Figure 22 is a washer-type load cell for measuring compressive axial loads. The unit requires an excitation voltage of 10 V, and generates an output of 21.5741 mV when compressed to its design load of 5000 lb$_f$, according to the manufacturer's specifications. The no-load reading is approximately zero mV, and output increases linearly with increasing load. In use, the load cell is installed on a bolt with a flat washer underneath the cell and a spherical washer on top of it to ensure uniform axial loading. The 10 V excitation is supplied by a regulated power supply, and the output voltage is read using a National Instruments PXI-5142 digitizer. A PC running LabVIEW is used to interpret the signal from the digitizer, convert the mV output into a force reading, and display the reading. The conversion equation is: $F = 5000 lb_f \left(\frac{X\, mV}{21.5741\, mV} \right)$. To reduce the effects of random noise in the signal, the LabVIEW VI was designed to keep a running average of the last 25 data points, and display this number as the load reading, while sampling continuously. This level of average was found experimentally to provide the maximum reduction in load reading fluctuation under static load, without introducing appreciable delay into the presentation of dynamic loading (i.e. without compromising real-time accuracy of the load reading). Using the torque wrench currently used in our laboratory, the loads indicated in Table 3 were measured at the various torque steps applied to a bolted joint during an SHM experiment. Based on the manufacturer's specifications, the accuracy of the axial load measurements with Omegadyne LCWD-5k is ± 25 lb$_f$.

In the acousto-elastic test, the bolted plate specimen was placed on foam to implement the free-free boundary condition. The plates were instrumented with two circular PWAS (diameter – 7 mm, thickness 0.25 – mm) bonded with the cyanoacrylate adhesive. The RITEC RAM-5000 ultrasonic testing system was utilized to generate 5 count ultrasonic pulses. Sensors S2 and S1 were used respectively to transmit and receive the elastic wave signals at 400 kHz.
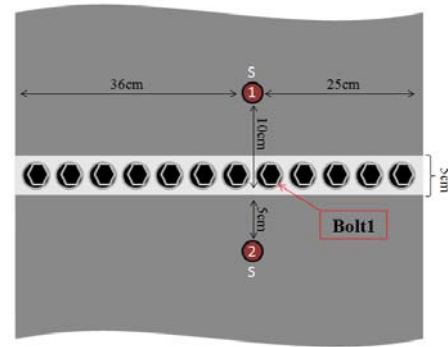
Figure 23 Bolted plate specimen and sensor layout.

Initially, all bolts in the joint were "fully tight" at 35 ft-lbs. Then, to simulate various conditions of the joint, a torque wrench was used to apply specific torques on one of the bolts situated on the wave propagation path between sensors S1 and S2 as indicated in Figure 23. First, the bolt was loosened to establish the "finger-tight" condition, which approximately corresponded to 0.1 ft-lbs. Subsequently, the torque levels were increased to 15 ft-lbs, 25 ft-lbs, and 35 ft-lbs. The elastic wave signals corresponding to the indicated levels of torque were recorded with the 16 bits, 100 Ms/s high-speed digitizer. Elastic wave pulses exemplifying the extreme "finger-tight" and 35 ft-lbs conditions are presented in Figure 24(a)(b). According to the figure, ultrasonic signals corresponding to "finger-tight" and 35 ft-lbs cases substantially differ in both time of arrival (or signal phase) and amplitude. It is suggested that both of these features can be employed to detect a loosened bolt.
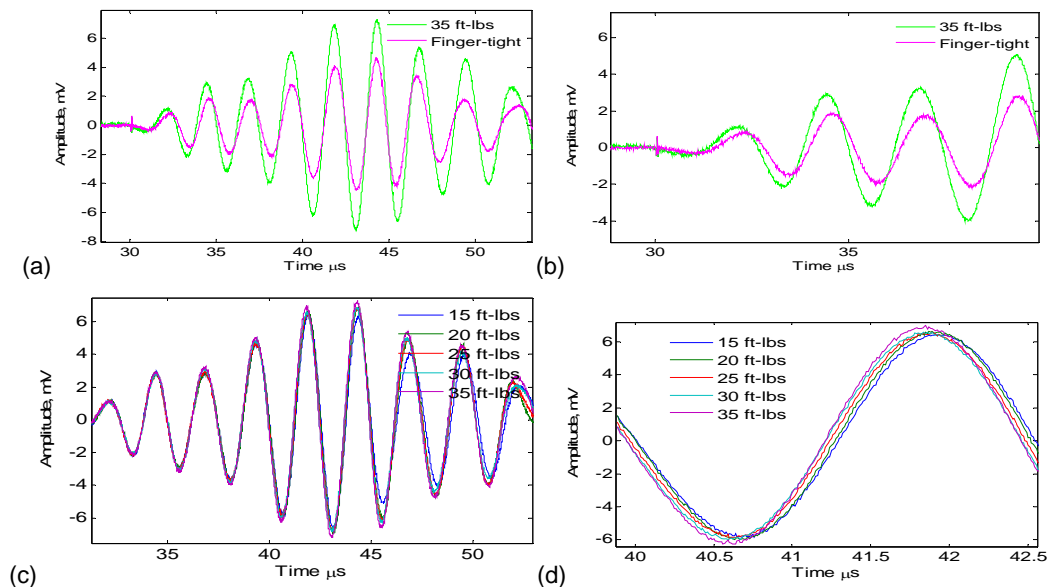
Figure 24 Elastic wave signals acquired in the bolted panel test: (a) the first pulse corresponding to "finger-tight" (FT) and 35 ft-lbs conditions on bolt 1, (b) zoomed-in portion of signal in (a), (c) ultrasonic signals obtained at various load levels and (d) zoomed-in portion showing stress-induced phase shift.

Figure 24c and 7d present details of ultrasonic signals corresponding to various levels of torque applied to bolt 1. The figure indicates a consistent time delay (or signal phase shift) proportional to changes in the applied load. However, as the toque level on bolt 1 approaches the torque on other surrounding bolts, the phase shift becomes less pronounced as illustrated by conditions of 30 ft-lbs and 35 ft-lbs in Figure 24d. Hence, as anticipated, small differences in torque levels with respect to other bolts would be possible but difficult to detect. In contrast, large variation of torque and extreme conditions such as "tight" and "loose" bolts produce clear differences in phase and amplitude of the ultrasonic waves. The experiment with bolted plates has also demonstrated potential to evaluate a torque drop on one of the bolts.

4.2.1 *Principles and Realization of the Phase Scan Baseline-Free Method*

The acousto-elastic method described above utilizes a baseline of the intact (undamaged) conditions of the structural joint. This approach is effective in detecting and even locating the "loose" bolt as discussed in Doyle et. al., (2008) [51]. However, the need for a baseline limits utility of the acousto-elastic damage detection. To mitigate requirement of the baseline, relative ultrasonic measurements were considered. In particular, each structural condition was assessed using ultrasonic signals with four different initial phases. The initial phase of an excitation signal supplied to PWAS was shifted by 90 degrees, and resultant elastic waveforms were measured. For convenience, scanning of the initial phase at 0, 90, 180, and 270 degrees was implemented. An effect of phase scanning on the received signal is illustrated in Figure 25, where ultrasonic signals are shifted by 90 degrees. Figure 25 was obtained for "loose" and "tight" condition of a single bolt in a bolted joint connecting two thin aluminum plates. All other bolts in the joints were set to "tight". The figure visually indicates difference between top (loose) and bottom (tight) signals corresponding to these experimental scenarios. However, in the proposed baseline-free phase-scan method, signals with different initial phases for each condition are compared. It is anticipated that the "damaged" case could yield more difference to signals of different phase than the "undamaged" case. In order to infer this difference, signals with 180 degrees phase shift are added. The level of a harmonic signal in the resultant difference is evaluated using spectral analysis as presented in the example below. Based on the level of the residual signal, a decision is made on the condition of the joint.
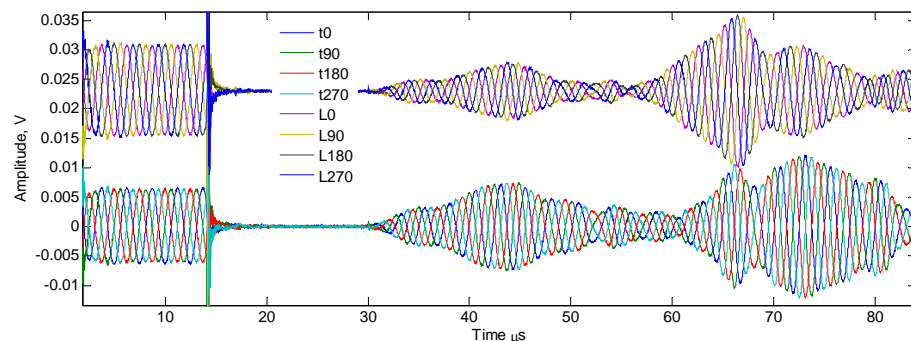
Figure 25 Elastic wave signals collected on a bolted plate specimen under "tight" and "loose" condition of bolt 1. Each group of records consists of signals with four different initial phases.

In the proof-of-concept experiment, all bolts in the joint were subjected to 35 lb-ft torque. One bolt, directly on a line (left) between sensors S2 and S1 was removed and an Omegadyne LCWD-5k load cell with equivalent bolt was placed in this location. Several levels of torque according to Table 3 were applied to the bolt in the load cell. Sensor S2 was used as a transmitted and sensor S1 as a receiver of elastic wave signals with different initial phases. An excitation signal was a 5 count pulse with a central frequency of 400 kHz. As a result, 4 signals (0, 90, 180, and 270 degrees) were obtained for each load level in the joint.
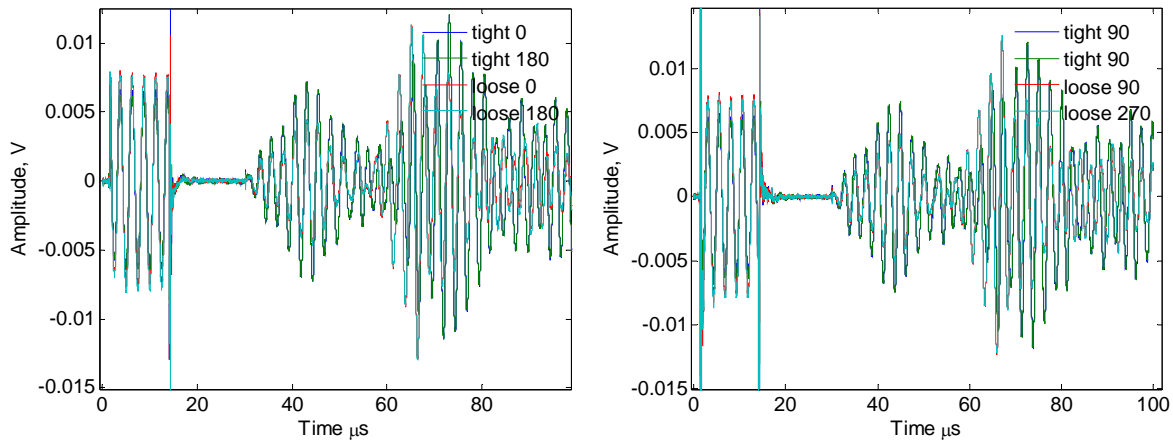
Figure 26 Elastic wave signals collected on a bolted plate specimen under "tight" and "loose" condition of one bolt in the joint. Each figure indicates processing of 180 degrees out-of-phase signals.

Results of subtraction of signals with 0 and180 degrees and 90 and 270 degrees of initial phase are illustrated in Figure 27 for different stress conditions in the bolted joint. Data for "tight" condition (35 ft-lbs) is the same for all figures. "Loose" condition indicates the torque level in the figure title (e.g. 30 ft-lbs for figure (a)). As it could be seen in the figure, the "finger tight" condition shows much larger amplitude of the out-of-phase signals. To quantify difference in amplitude of these signals, we calculated their spectral characteristics (using FFT) shown in Figure 28. An advantage of using spectral characteristics is that such characteristics provide amplitude of spectral component at transmitted frequency of 400 kHz and, in addition, show evolution of spectrum due to different stress conditions. The latter may be considered as an addition parameter in discriminating torque levels.
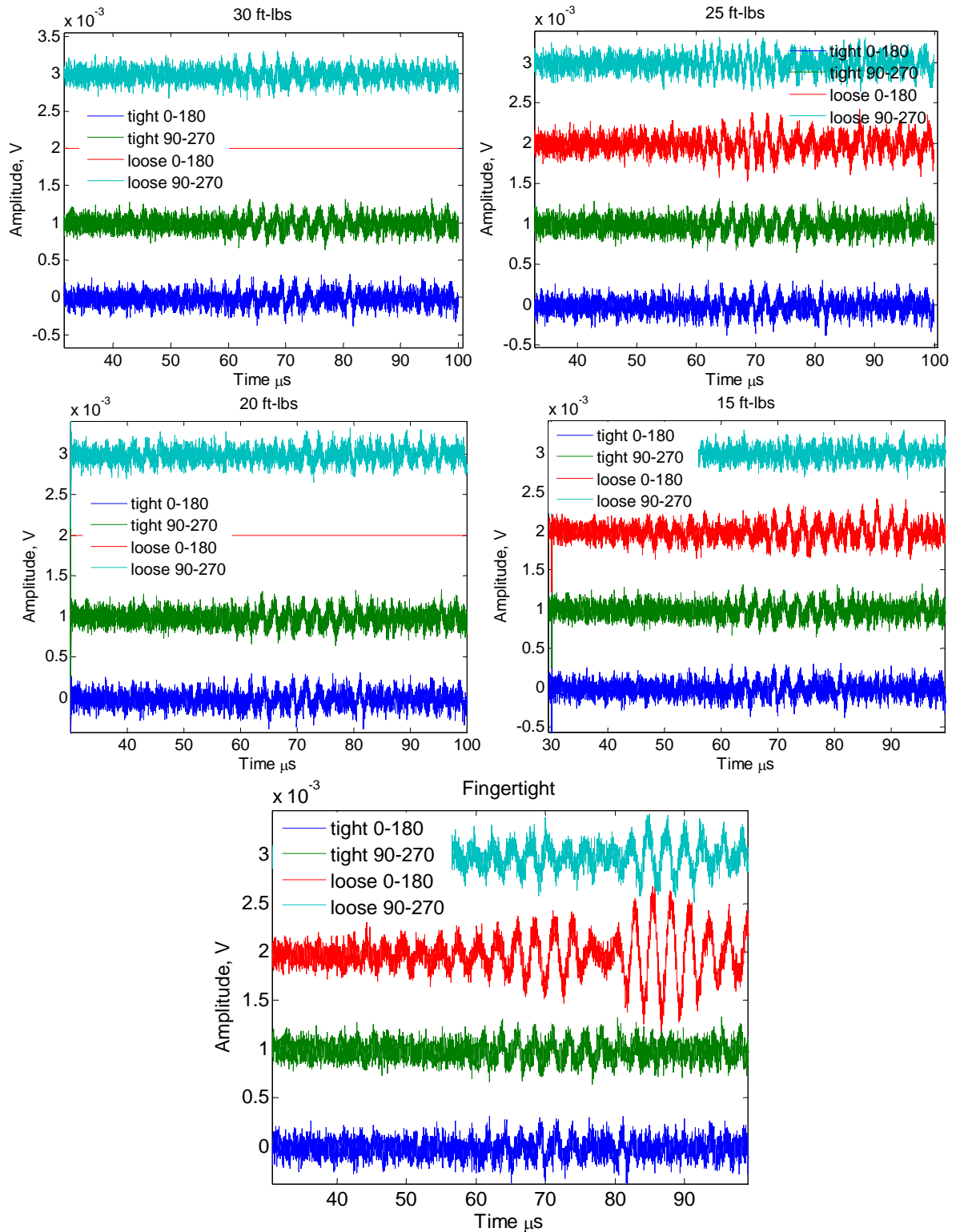
Figure 27 Results of subtraction of out-of-phase signals for different stress conditions in the bolted joint. "Tight" is the data for 35 ft-lbs, "loose" is data for the stress condition indicated in a title of each plot.
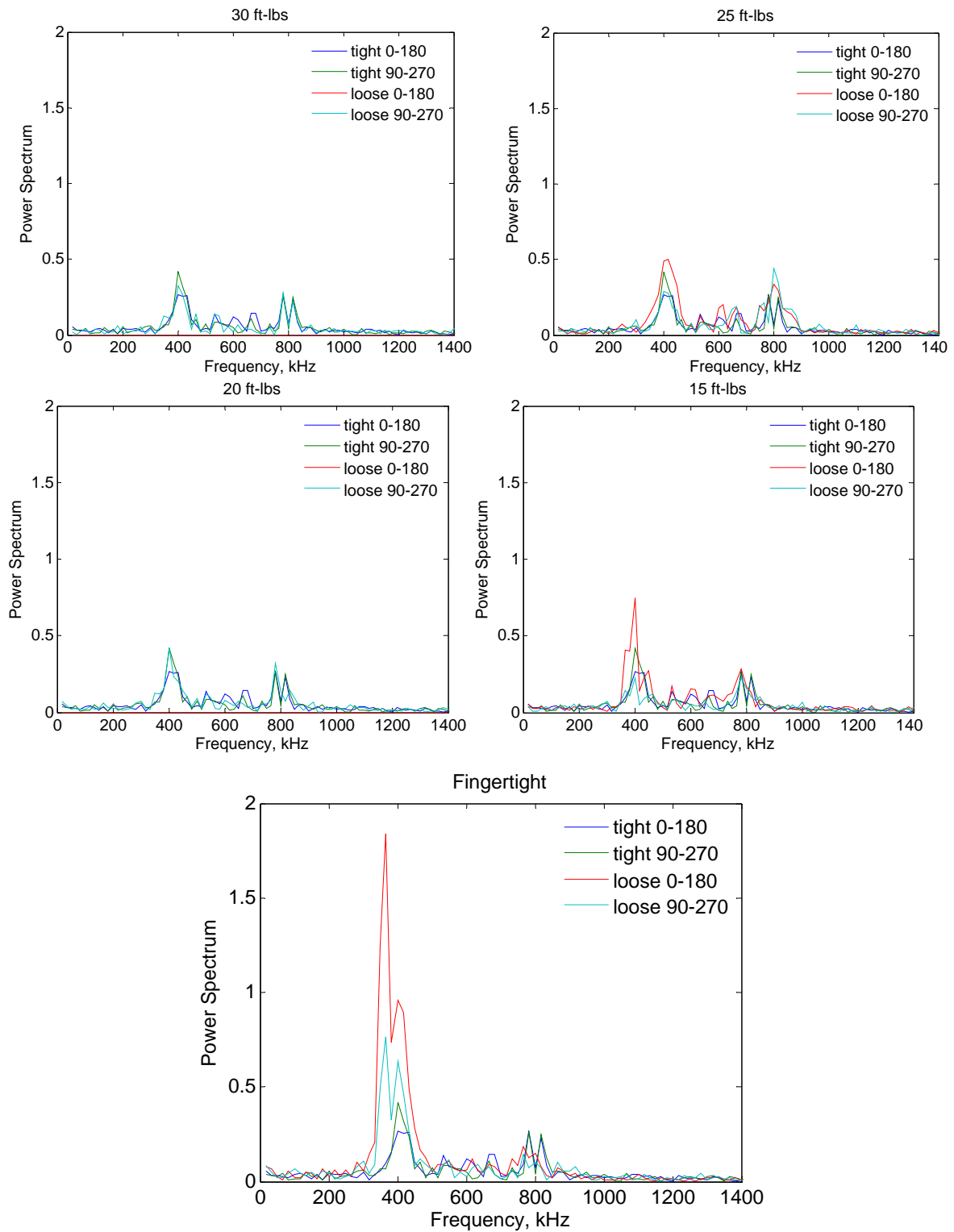
Figure 28 Power spectrums of time-domain records illustrated in previous figure.

An algorithm for baseline-free detection of a defective joint could incorporate assessment using a threshold. For example, a threshold in the proof-of-concept experiments may be set to 0.5 amplitude of the spectrum in Figure 28. Figure 28 suggests indistinguishable cases for joints subjected to 35 ft-lbs and 30 ft-lbs respectively. The 25 ft-lbs case shows some difference, but probably not significant enough to warrant reliable discrimination of two torque levels. Minor differences were observed for the case of 20 ft-lbs. However, the case of 15 ft-lbs shows noticeable difference exceeding the 0.5 threshold. The finger-tight (i.e. loose bolt) case is reliably distinguished from the "tight" 35 ft-lbs condition. Proof-of-concept experiments has shown capability of the baseline-free amplitude scan method to detect the "loose bolt" condition and discriminate between high (35 ft-lbs) and low (15 in-lbs) torque levels. It is suggested that although discrimination capabilities of the phase scan baseline-free method is lower than the acousto-elastic method with the baseline, it indicates potential for assessing not only binary ("tight" and "loose") scenarios, but also distinguishing high and low torque conditions.
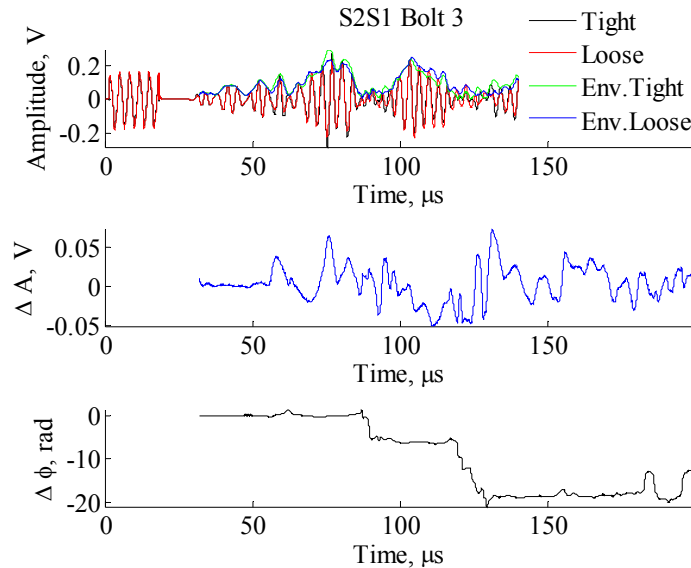
Figure 29 Typical acousto-elastic experimental results for a thin-walled specimen.

4.2.2 *Phase and Amplitude Signals Parameters for Thin Plates*

The experimental thin-walled structure consisted of two thin (2.42 mm thickness) aluminum 6061 plates fastened together with 12 1" 3/8-16, grade 8, hex flange bolts. The plates were subjected to free-free boundary conditions. Two PWAS were installed with cyanoacrylate adhesive: one on the top plate and another on the bottom plate. Piezoelectric sensors were made from APC-851 piezoelectric ceramic with electrodes allowing for one-sided access (i.e. configuration with feedback electrode). During tests, sensor 2 on the bottom plate transmitted a 5-pulse 300 kHz signal, which propagated through the bolted joint and was received by sensor 1 on the top plate. Equipment, software, and data acquisition procedure used in the tests were similar to the setting described in Doyle et al. (2010) [52]. To reduce contribution of noise, a waveform representing average of 150 signals was recorded. The

first test was conducted with all of the bolts fully torqued to 35 ft-lbs. Once the data was collected, bolt 3 was loosened and the test was run again at this condition. Bolt 3 was then re-tightened back to 35 ft-lbs and data was collected again. This process of loosened and re-tightening continued for bolts 4-8. The collected data was then analyzed with both the instantaneous phase method and the zero-crossing method.

Figure 29 illustrates typical experimental results for "tight" and "loose" condition of a particular bolt. To obtain amplitude and phase information, Hilbert transform was applied to the signal record and amplitude and phase were calculated using Eq. (4). Envelopes of signal amplitude are presented on the top portion of Figure 29 along with collected raw data. The differences between signal envelops corresponding to "tight" and "loose" conditions of the joint are presented on the medium portion of the same figure. Noticeably, this difference becomes pronounced as a clear change in magnitude of the difference around late 50 μs – early 60 μs, indicating location of a loose bolt. Phase of the signal was unwrapped in accordance with an algorithm described above and implemented with Matlab's `unwrap(x)` function. The phase difference between "tight" and "loose" test scenarios is illustrated in the bottom portion of Figure 29; the curve suggests considerable changes in late 50 μs – early 60 μs. Another interesting feature inferred from the phase plot in Figure 29 is information on phase leading or lagging with respect to baseline (i.e. "tight") signal. Noticeably in the temporal waveforms on Figure 29 top, a record corresponding to "loose" bolt condition first lead (around 60 μs) and than lags (around 70 μs) the baseline "tight" signal. A summary of changes in amplitude and phase for "tight" and "loose" conditions of several bolts in the joint is presented in Figure 30. As it can be seen in the figure, position of initial phase shift depends on location of a "loose" bolt. Immediate changes are noticeable for bolts 5 and 6 which are on the direct wave propagation path between sensor 2 and sensor 1. Data for bolts 4 and 7 show shift at later time, as the elastic wave is reflected from these joints and travels longer distance. Interestingly, pairs of bolts (5-6, 4-7, and 3-8) are symmetric with respect to direct wave propagation path and hence exhibit changes of opposite sign in Figure 30. It should be noted that amplitude data generally follows results of phase calculations, but is less accurate in indicating position of a loose bolt. In contrast to phase, amplitude is less effective in detecting immediate changes in waveforms for bolts 5 and 6 on a direct wave propagation path between the sensors.
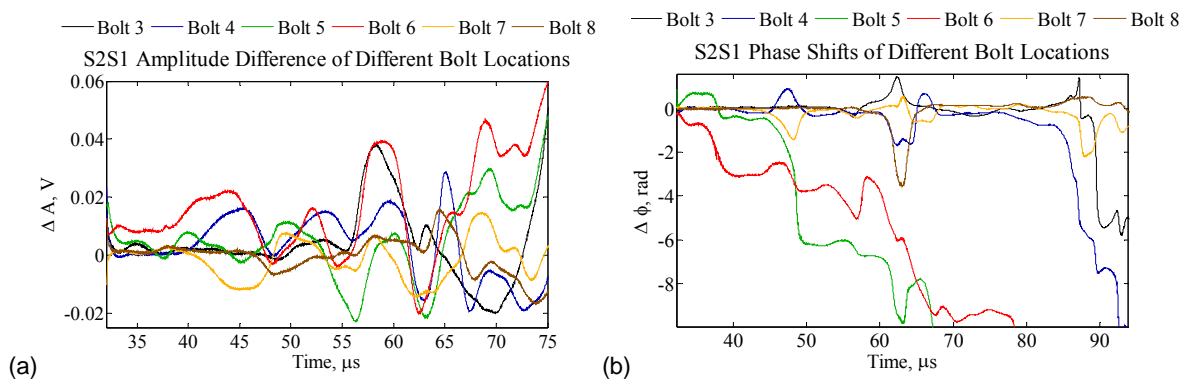
Figure 30 Amplitude change (a) and phase shift (b) for "tight" vs. "loose" condition of the indicated bolts in the joint.
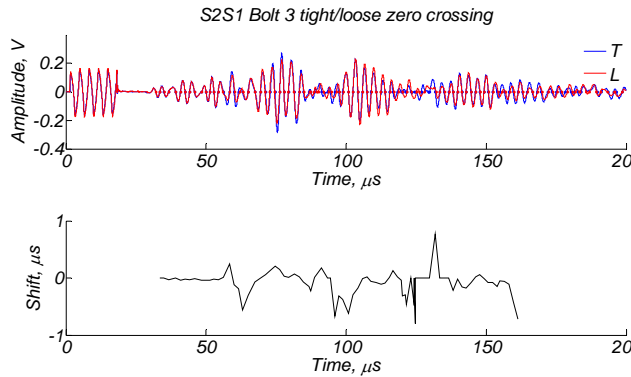
Figure 31 Experimental data (top) and a shift between zero crossings in signals corresponding to "tight" and "loose" condition of bolt3.
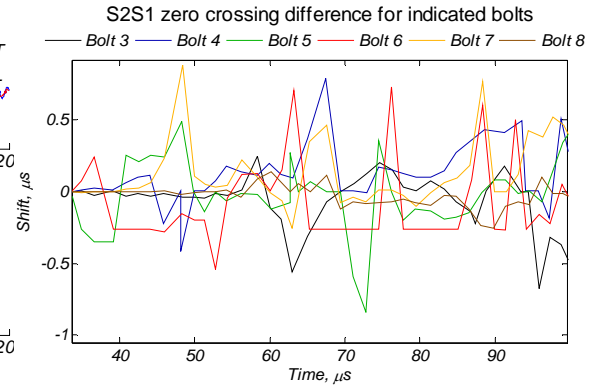
Figure 32 Summary of zero crossing difference for indicated bolts.

An alternative approach to determining phase changes in a signal is the zero crossing method described above. Raw waveforms are presented in Figure 31. The time shift in Figure 32 is calculated as difference between zero crossings in signals corresponding to "tight" and "loose" conditions. Remarkably, results of zero crossing processing are in excellent agreement with the instantaneous phase data; even symmetry of the shift for pairs of bolts is preserved.

4.2.3 Reference-free phase scan method and instantaneous parameters

Damage detection methods discussed above involved comparison of measured data to a "reference" or "baseline" representing "tight" or "undamaged" condition of the bolted joint. To reduce dependence on the reference data, a reference-free method was developed (Zagrai et al., 2010). The method consists of sequential transmission of elastic signals with opposite phases (e.g. 0, $\pi/2$, π, $3\pi/2$), which manifest identical signal features for expansion and contraction cycles of the propagating elastic wave. In the linear system, these features will cancel out upon summation. In nonlinear system, however, features will not cancel out completely due to acousto-elastically induced differences in expansion and contraction portions of waveforms. Illustration of the method is presented in Figure 33. Upper and lower waveforms in Figure 33a correspond to raw signals collected for "tight" and "loose" conditions of bolt 5 of the plate specimen discussed above. Sensors S2 and S1 were used to transmit and receive elastic wave signals. The "tight" condition of the joint corresponded to 35 ft-lbs while the "loose" condition of the joint corresponded to "finger-tight" bolt 6. Noticeable in the figure, amplitude of the initial pulse in the "tight" data is larger than in the "loose" data; this observation is also reflected in Figure 33b representing instantaneous amplitude calculated from the raw data using equation 4. Instantaneous phase was determined with the second equation 4 and unwrapped for continuous representation in Figure 33c. In the reference-free method, we consider a difference between the amplitudes and phases for signal pairs with the following initial phases: 0, π and $\pi/2$, $3\pi/2$. The amplitude differences are presented in Figure 34a and instantaneous phase differences are presented in Figure 34b. The figure suggests that amplitude difference is larger for "loose" condition rather than for "tight" condition. Hence, a threshold may be implemented to

distinguish between these cases. Instantaneous phase data shows even more pronounced difference that improves the detection capabilities of the method. Therefore, concurrent use of amplitude and phase information is recommended.
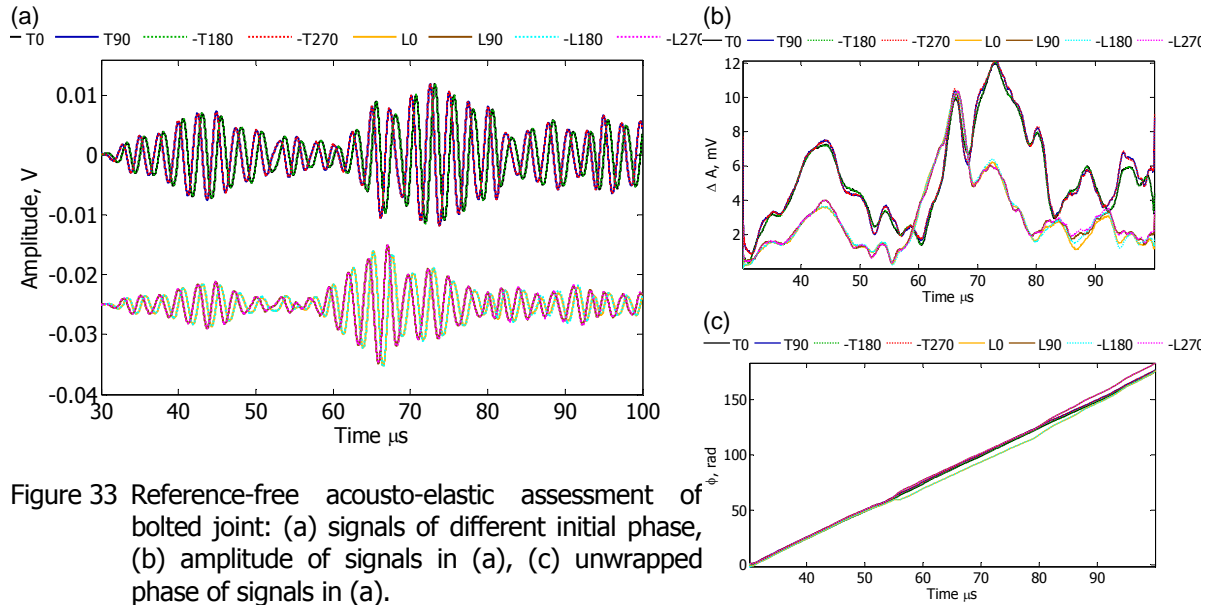
Figure 33 Reference-free acousto-elastic assessment of bolted joint: (a) signals of different initial phase, (b) amplitude of signals in (a), (c) unwrapped phase of signals in (a).
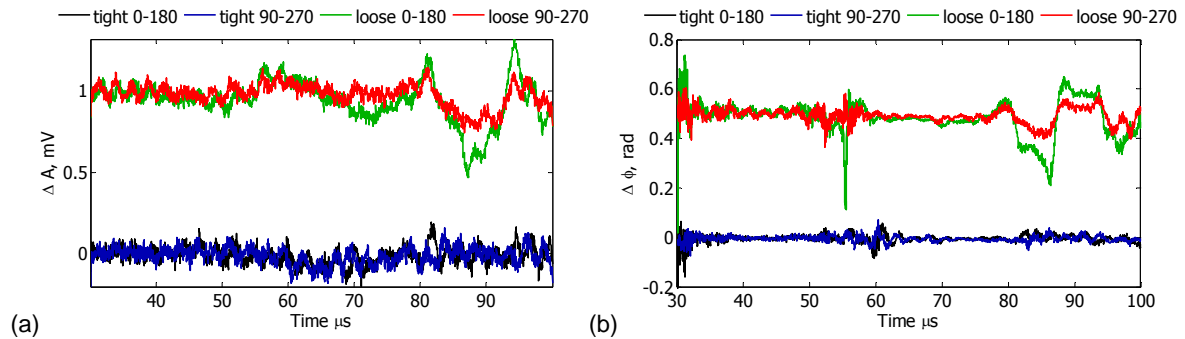
Figure 34 Difference between instantaneous amplitudes (a) and phases (b) for signals shifted by п.

4.3 Assessment of Bolted Joints In Satellite Panels of Complex Geometry

Experiments with specimens of relatively simple geometry have shown applicability of phase and amplitude features in condition monitoring of bolted joints. Transition to a specimen of complex geometry was considered and several studies illustrating performance of the acousto-elastic method for assessment of structural integrity were conducted.

4.3.1 Influence of signal excitation level on phase detection

Acousto-elasticity is a nonlinear phenomenon in which the manifestation depends on condition of an excitation signal. One of the most critical parameters of the excitation signal is its amplitude. If amplitude of the excitation signal is too low, manifestation of acoustic nonlinearity may be weak and difficult to detect. Therefore, studies on the effect of excitation levels on the magnitude of the phase shift are of paramount importance to the practical realization of acousto-elastic SHM. Below we present results of an experimental study on the effect of signal amplitude on the acousto-elastic detection of loose bolts in a realistic satellite panel.
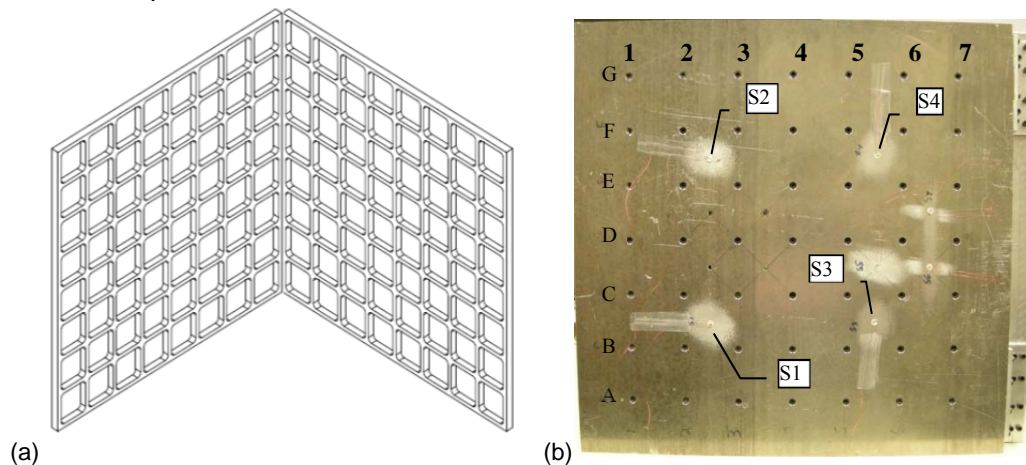
Figure 35 (a) Inside view of a satellite panel showing isogrid; (b) front view of the panel with location of bolts and sensors.

A realistic satellite panel was built to resemble two sides of a real satellite. Each side was comprised of two isogrid plates bolted together as depicted in Figure 35a. The plates were made of aluminum 6061-T6 and measured 18"x18"x0.5" with an isogrid milled on one side consisting of 64 cutouts. Each cutout was 2"x2"x0.875"and spaced 0.25" from the next. The plates were then bolted together with the isogrid on the inside using 49 1" #8-32 socket cap screws. The top plate had 49 0.164" through holes with a 0.64" counter bore with a diameter of 0.27". The bottom plate was given 49 holes to line up with the top plate however; they were threaded for #8-32 bolts. In order to properly specify bolt location, the columns and rows were labeled 1-7 and A-G as shown in Figure 35b. Four circular feedback PWAS were then installed in a rectangular grid using a cyanoacrylate adhesive and were labeled as illustrated.

During a test, PWAS were excited at different voltage levels in order to transmit elastic waves of different amplitudes. A 3 count 350 kHz pulse signal was supplied to sensor S1 which generated a wave traveling towards S2, which was used as a receiving sensor. The

test was run for two conditions of the joint. For the first conditions all of the bolts were tightened to a torque of 35-40 in-lbs. The excitation level for each test was set at different levels on the RITEC system. The first test was run at the output level 5, which corresponds to 64 volts, and was increased by 5 for each subsequent test up to level 30 corresponding to 187 volts. Once all the excitation levels had been run for the "tight" condition, bolt D4 was loosened and the data was collected again.
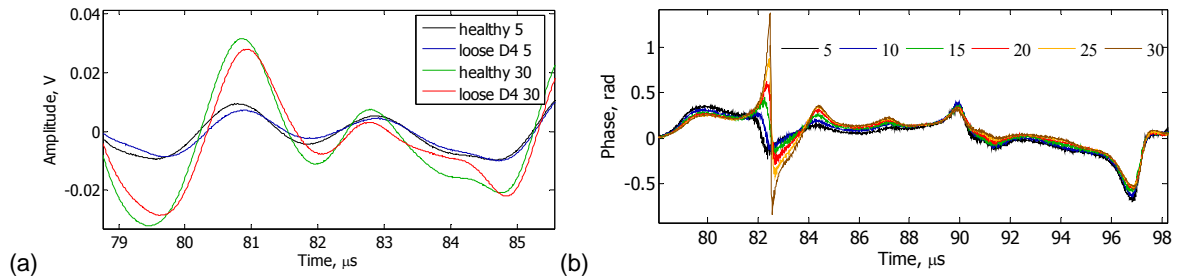
Figure 36 (a) Healthy (tight) and loose waveforms for excitation level of 5 and 30, (b) effect of excitation level on instantaneous phase shift between tight and loose waveforms.

The results of the test indicate that the excitation level does have an effect on the amount of phase shift in the elastic waveform. Figure 36a illustrates a zoomed portion of the waveforms. Noticeably in the figure, waveforms acquired at high excitation level of 30, suggest larger difference in amplitude and phase features than waveforms acquired at low (5) excitation level. Experimental data for intermediate levels follow this trend. Instantaneous phase differences for the signals corresponding to the "tight" and "loose" conditions of the joint are presented in Figure 36b. It can be observed that the amount of visible shift from the tight to loose case changes for each excitation level. The peaks which occur at the time 82.5 μs show that the most shift occurred in the test run at 30, which is a unitless excitation level in Ritec system. As the level is decreased the amount of shift also decreases for this section of the plot. However, it should be noted that at around 90 μs the lower excitation levels produce more phase shift which decreases as the excitation level increases. This discrepancy may be related to the mutual orientation of the wave propagation vector and stress in the joint. In general, it was observed that the higher the excitation level, the larger the phase shift. However, high excitation levels could contribute to sensor fatigue and levels in a range 15 to 20 (110 to 130 volts) are generally recommended.

4.3.2 *Detection of a missing bolt in a satellite panel*

One of possible damage scenarios in a complex structure with bolted joints is a missing bolt. A series of tests were performed to observe an effect of a missing bolt and its location on the amplitude and phase of an elastic wave transmitted from sensor 1 to sensor 2. A harmonic 5 count 300 kHz pulse was applied to transmitter S1. Acoustic signal was received by S2 and averaged 150 times to reduce noise. The first measurement was performed with all of the bolts tightened to 35-40 in-lbs. Once the data was recorded the bolt, D1, was removed. The wave was again propagated from sensor 1 to 2 and the data was collected. The bolt was then replaced and retightened. In the next step, bolt D2 was removed. Data was collected for this condition and the bolt was replaced and retightened. The process continued for bolts D3, D4, D5 and D6. The location of bolts and sensors are illustrated in Figure 35b.

An example of signals collected in one of experiments is shown in the top portion of Figure 37. Also shown in the figure are the temporal distributions of instantaneous amplitude and phase differences between "healthy" and "no bolt" conditions. A summary of these differences for all of the experimental scenarios is presented in Figure 38. It should be mentioned that results of zero-crossing processing matched with Figure 38.
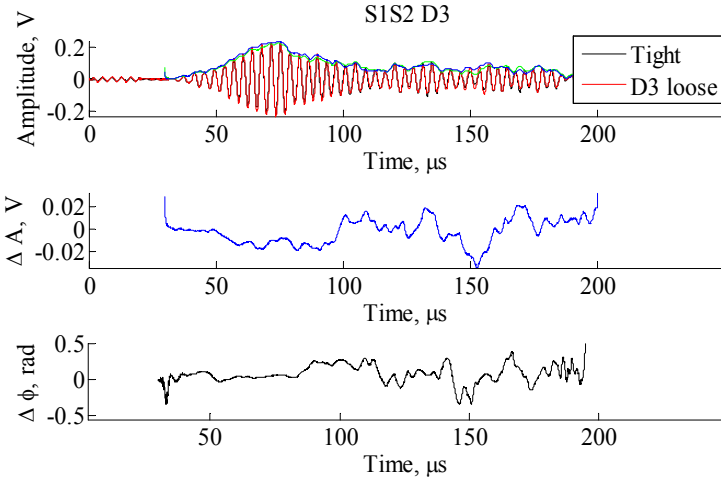
Figure 37 Signals collected for tight and no-bolt conditions of bolt D3 (top), difference in signal amplitude (middle) and phase (bottom).

(a)   (b)
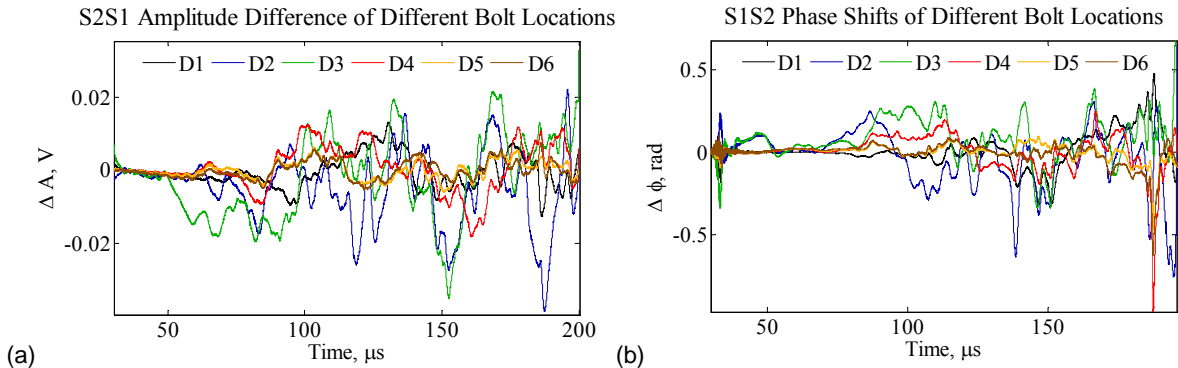
Figure 38 Amplitude and phase difference for indicated missing bolt.

Although amplitude and phase data for the missing bolt experiment show elements of similarity, in general, they do not match. Because of noticeable changes in 45-50 µs range, the instantaneous phase allows for detection of a missing bolt located close to direct wave propagation path between the sensors. In contrast, the instantaneous amplitude does not suggest activity below 60 µs. Sound speed also appears to vary depending on presence of bolt, which results in different time of occurrence for signal features in Figure 38.

4.3.3   Detection of a loose bolt in a satellite panel

Detection of a loose bolt is the one of the critical tasks of an on-board SHM system. To investigate suitability of the instantaneous amplitude and phase in determining location of a loose bolt, several experiments have been conducted that involved collecting data for tight and loose conditions of a particular bolt on a panel. The tight condition corresponded to the case when all bolts on a panel were properly torqued.
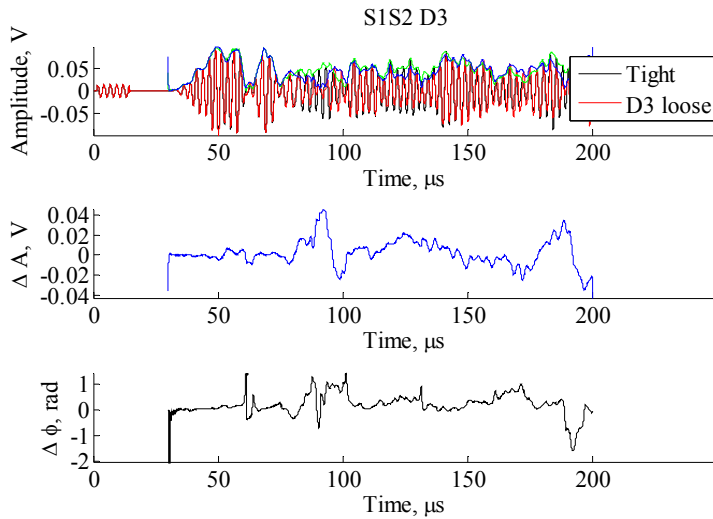
Figure 39 Signals collected for tight and loose conditions of bolt D3 (top), difference in signal amplitude (middle) and phase (bottom).

Sensors S1 and S2 were utilized as a transmitter and receiver of elastic waves. First, all bolts were properly torqued and the waveform corresponding to this condition was collected. Then bolt D3 was loosened to "finger-tight" state (several in-lbs) and an elastic wave was transmitted and recorded. Hence, in this experiment, the bolt was not removed from the panel. Upon collecting the data, the bolt was re-torqued to establish tight condition. Example of waveforms collected in the experiments are presented in Figure 39. Instantaneous amplitude and phase showing differences between the signals corresponding to the "tight" and "loose" conditions are shown in Figure 39bc. As it can be seen in the figure, changes occur not immediately, but after some time because bolt D3 is slightly off the direct wave propagation path between the sensors. The experiment was repeated for bolts D1, D2, D4, D5, D6 and results are reported in Figure 40a and 16b. Noticeable in the figure, the instantaneous amplitude data matches well with the instantaneous phase data, although there is a little discrepancy in the time of relative changes. Consideration of the phase shifts in Figure 40b and wave propagation distances for bolts D2D3, D1D4, D5, D6 (0.1707m, 0.2231m, 0.3018m, 0.3912m) suggests a sound speed of slightly above 3 km/s, which indicates propagation of anti-symmetric mode approaching Rayleigh velocity limit.
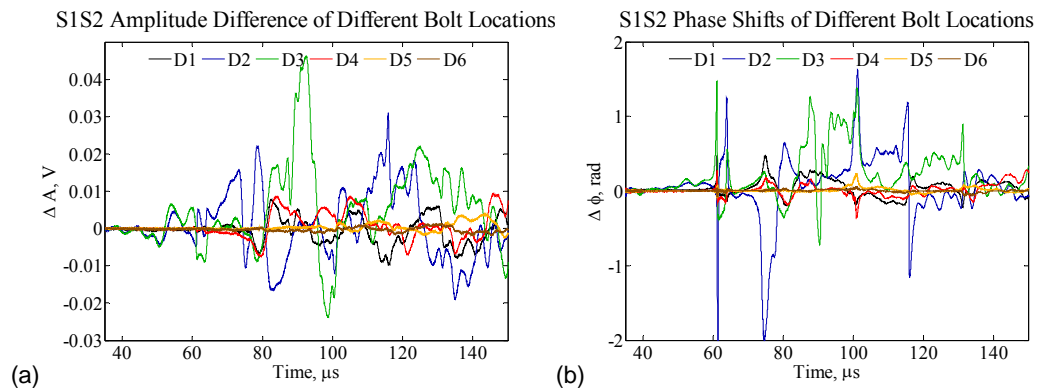
Figure 40 Amplitude and phase difference for indicated loosened bolt.

Figure 41 Sensor layout on a satellite panel utilized in a reference free acousto-elastic testing.

4.3.4   Reference-free acousto-elastic method in complex satellite structures

The final portion of work on complex satellite panel was devoted to investigation of performance of the reference-free phase scan acousto elastic method. The study is important to understand applicability and limits of the reference-free method in complex structures with isogrids. The experimental satellite panel described above consisted of satellite side panels with isogrid. Material of the panels is aluminum 6061. The two isogrid plates make one panel when the plates are joined with 49 bolts. A photograph of a panel with sensor layout is presented in Figure 41. The distances from sensor to sensor and sensor to bolts are shown in the figure. The distances were measured from the outside perimeter of the sensor or bolt.

All experiments were conducted by applying the 3count 350 kHz voltage signal to APC 851 piezoelectric sensor (7 mm diameter with feedback electrode) bonded to the panel with M-Bond 200 cyanoacrylate adhesive. Reference-free phase scan method was implemented by first transmitting a 3 count burst with 0 degree initial phase, and then repeating experiment for 90, 180, and 270 initial phases. Tight and loose conditions for bolts corresponded to approximately 30-35 ft-lbs torque (tight) and 1-5 ft-lbs torque (loose), the latter was implemented by finger-tightening the respective bolt. Experimental data was subjected to 5 points moving average filter to reduce noise. Reference-free processing consisted of calculating a Hilbert Transform of the collected signals, extracting amplitude and phase information for signals shifted in 180 degrees and considering respective difference between amplitude and phases in 180 degrees shifted signals. It is anticipated that a loose joint may show higher nonlinearity in the received signal and this effect may be captures in the phase signature. Depending on wave propagation conditions, amplitude difference may or may not manifest this nonlinearity. Particular details for each setup are presented below.
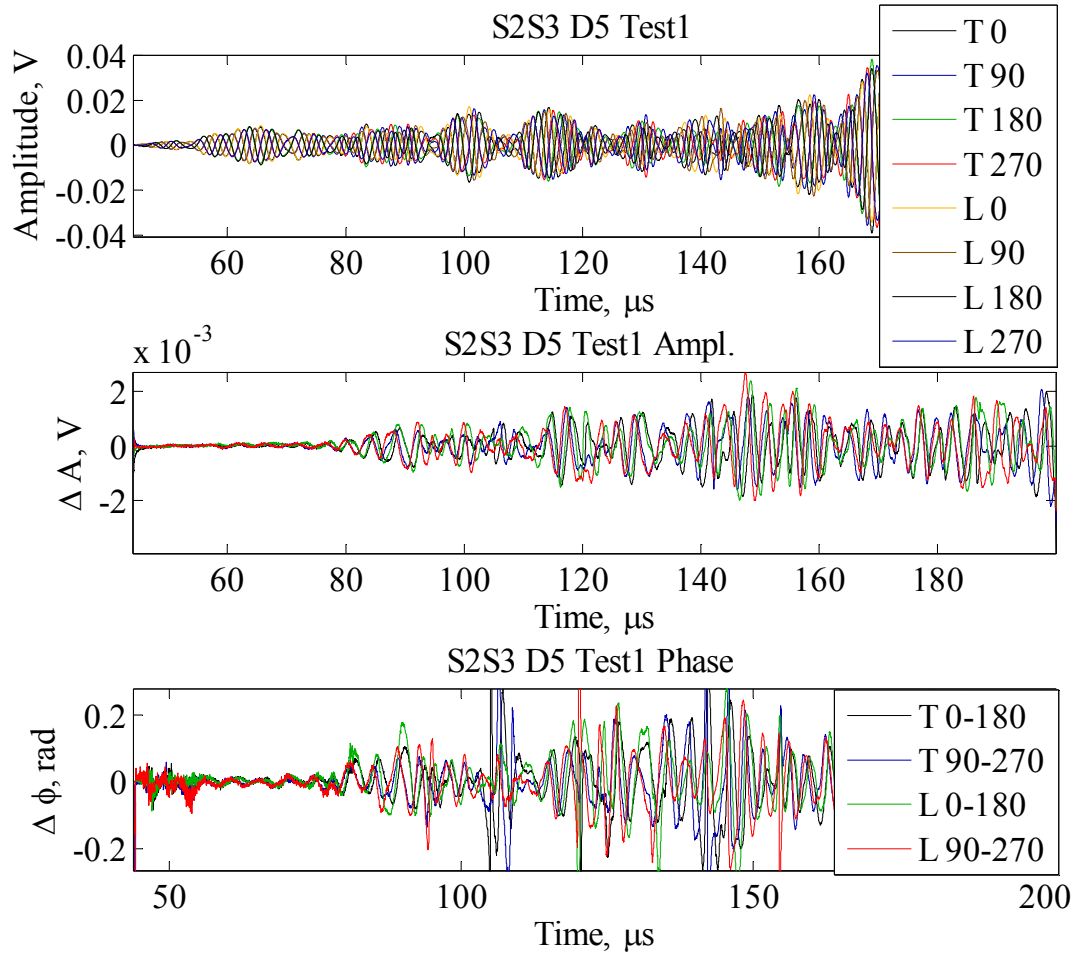
Figure 42 Sensor S2S3 signals for tight and loose bolt D5.

4.3.4.1. S2-S3 Diagonal Wave Path

Sensor S2 and S3 are located on the diagonal path for wave transmission. The elastic wave was generated with sensor S2 and received with sensor S3. Experiments involved loose and tight conditions of bolts D3 and D5. Please note that wave paths for these bolts are symmetric with respect to diagonal and hence elastic waves must arrive at the same time. However, bolt D3 is closer to transmitting sensor S2 and D5 is close to receiver S3, i.e. wave path to D5 is longer. Results of the experiments are illustrated in Figure 42and Figure 43. In Figure 42, analysis is presented for healthy (tight) and damaged (loose) conditions of the bolt D5. As is can be seen in the figure, noticeable amplitude and phase changes occur in the 80 μs region after arrival of the initial pulse. It is suggested that this occurs because neither bolt D5 nor D3 are on the exact diagonal line between sensors; these sensor are located some distance from the diagonal. It is interesting to note that due to symmetry of the D3 and D5 location, elastic wave arrive at the same time and changes in the signal important for damage detection (between 80 μs to 100 μs) also occur at approximately the same time for both of these bolts. Amplitude difference for π shifted signals is larger in the case of a loose bolt D5 rather than in the case of a tight bolt D5. Although this difference is rather

small, it may be used to distinguish "tight" and "loose" conditions of the bolt. However, the difference between these cases is much more pronounced when phase information is considered. Combination of both amplitude and phase may be used for detection of a loose bolt. Experimental data for bolt D3, however, shows little, if any, difference for amplitude of "loose" and "tight" cases. These is small difference in phase for these conditions, but much smaller than for bolt D5. One possible explanation for this discrepancy is that bolt D5 is closer to the receiving sensor and a nonlinear acousto-elastic behavior in that region may have more pronounced contribution in the receiving sensor signature. In contrast, nonlinear contribution of "loose" D3 is dispersed while a wave propagates longer distance to the receiving sensor.
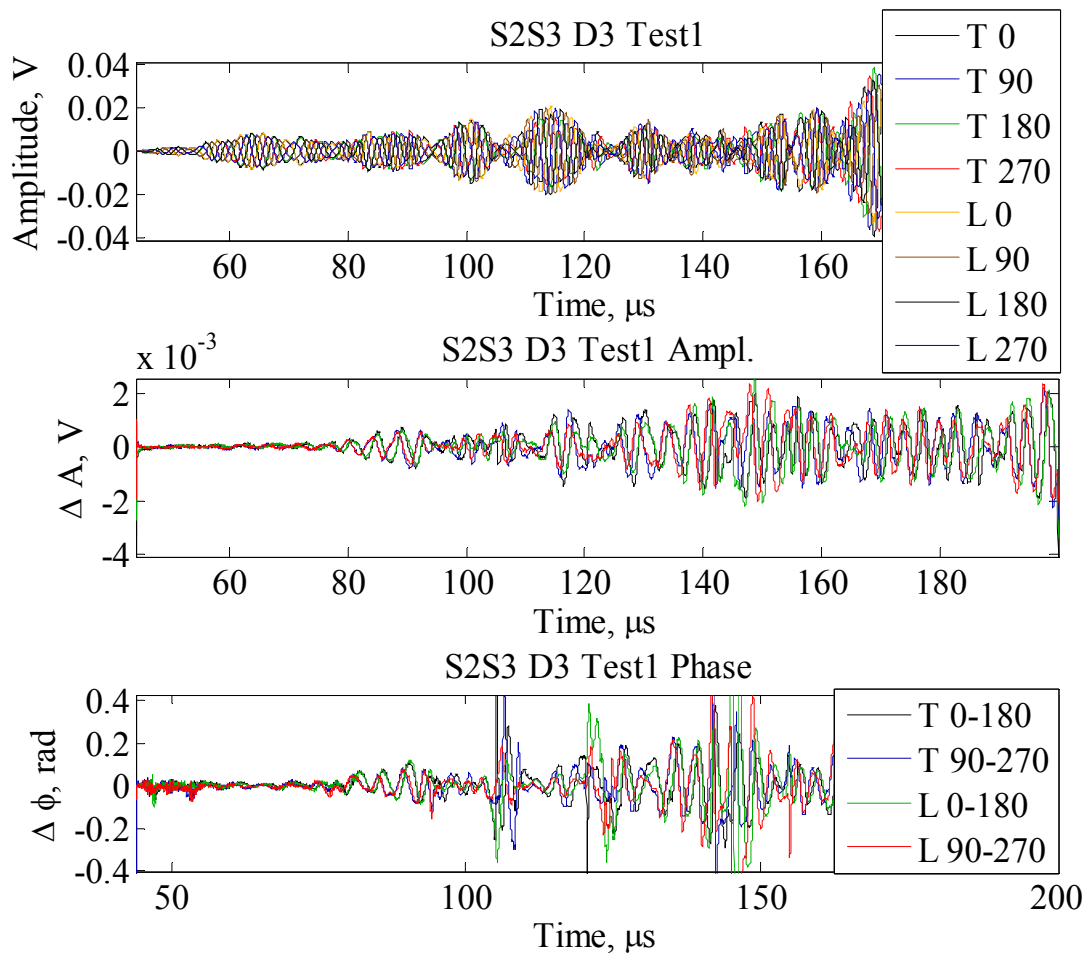
Figure 43 Sensor S2S3 signals for tight and loose bolt D3.

4.3.4.2. S2-S4 Wave Path

In the next set of tests, effect of bolts D3 and D5 on elastic wave propagation between sensors S2 and S4 was investigated. Excitation parameters and test procedures were the same as for the test described in the preceding section of the report. The collected signals are presented in Figure 44 and Figure 45. Analysis of the figures suggests that the difference for "tight" and "loose" scenarios in the reference-free phase scan method is too small to warrant reliable detection of loose bolts D3 and D5. We attribute this situation to rather far location of these bolts from a direct wave propagation path between S2 and S4. When signals corresponding to "loose" and "tight" conditions are compared directly, and difference between amplitude and phase features for these conditions is calculated, contribution of both bolts are seen around 120 µs. Figure 46 and Figure 47 illustrate this result. Difficulty in processing in the range of 80 µs to 100 µs is also seen in the figures as signal amplitude gets too low and instantaneous phase and amplitude changes may be misinterpreted as contribution due to loose bolt.
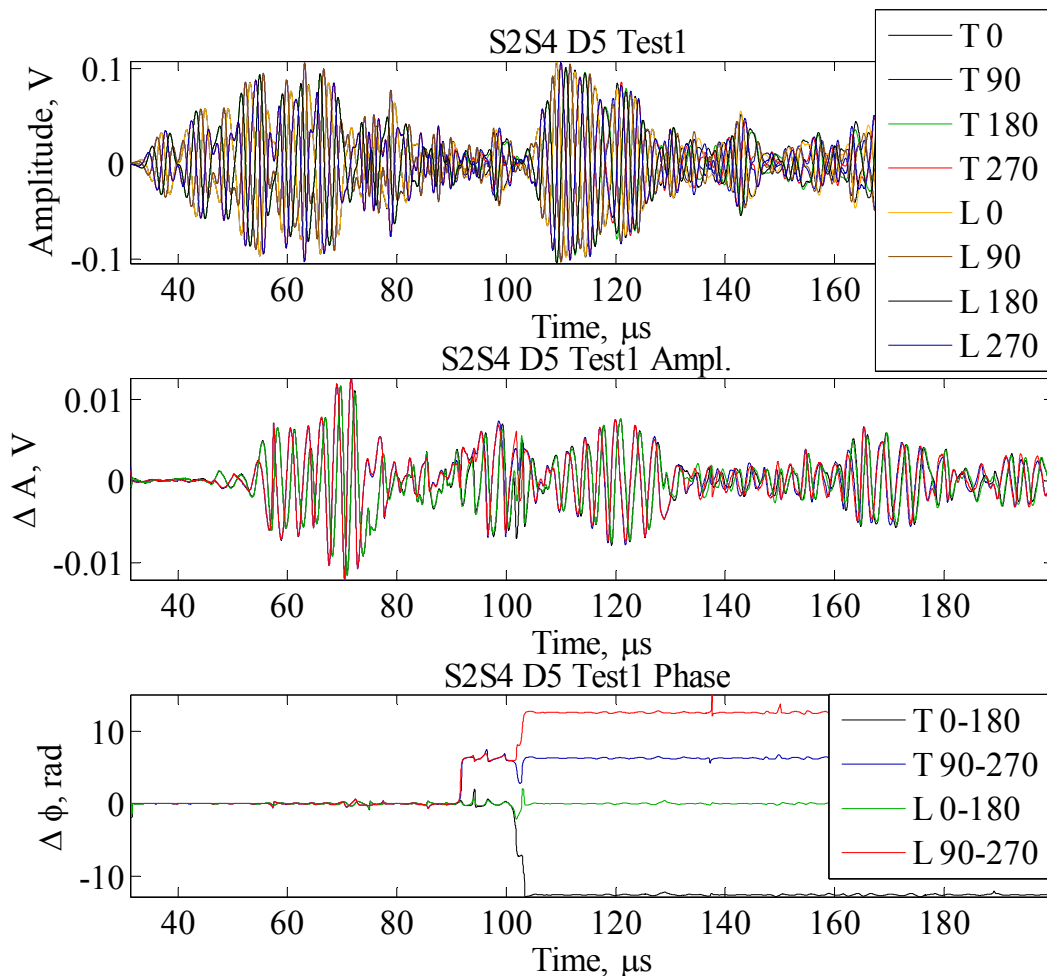
Figure 44 Sensor S2S4 signals for tight and loose bolt D5.

Approved for Public Release; Distribution Unlimited.

46
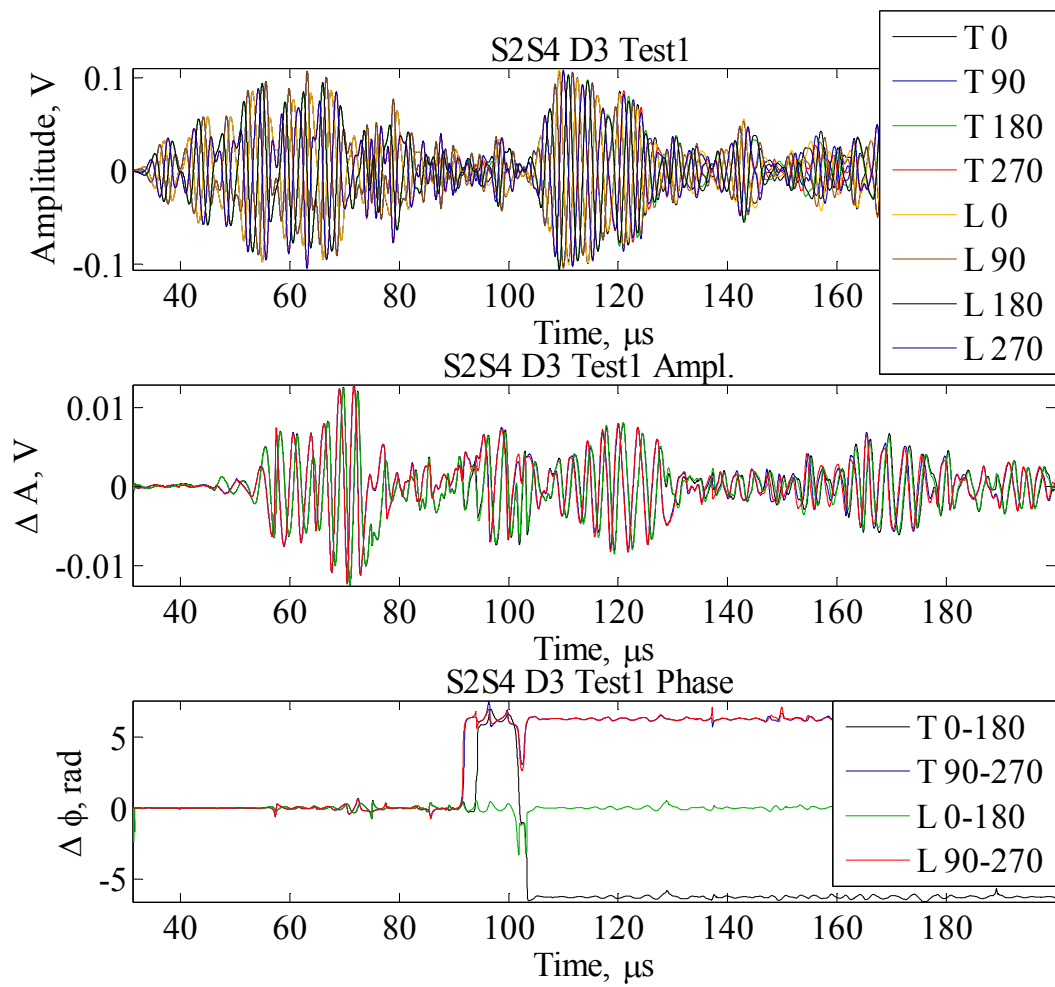
Figure 45 Sensor S2S4 signals for tight and loose bolt D3.
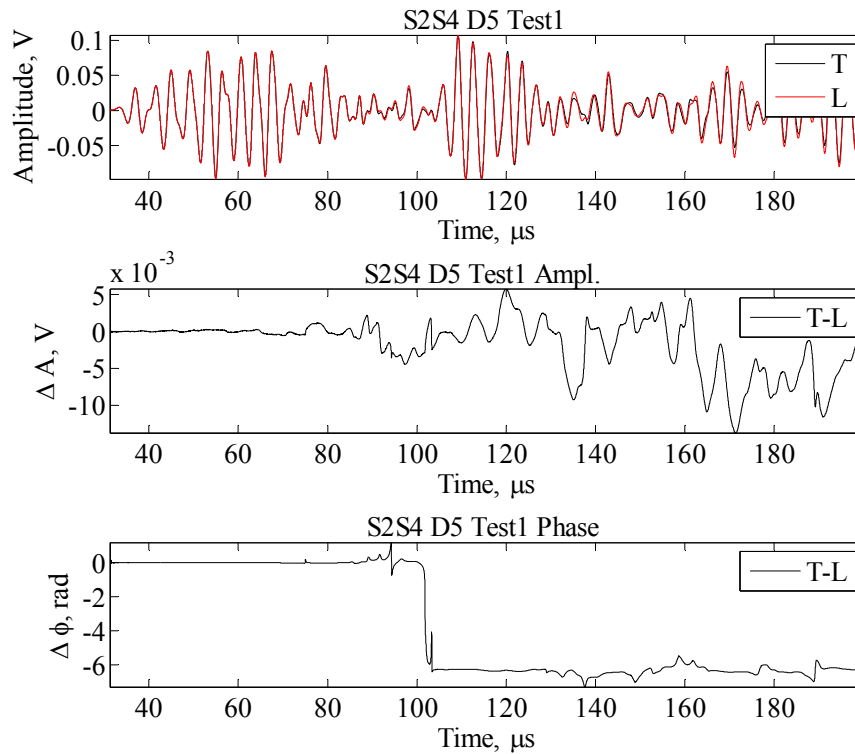
Figure 46 Sensor S2S4 signals for tight and loose bolt D5 – direct comparison.
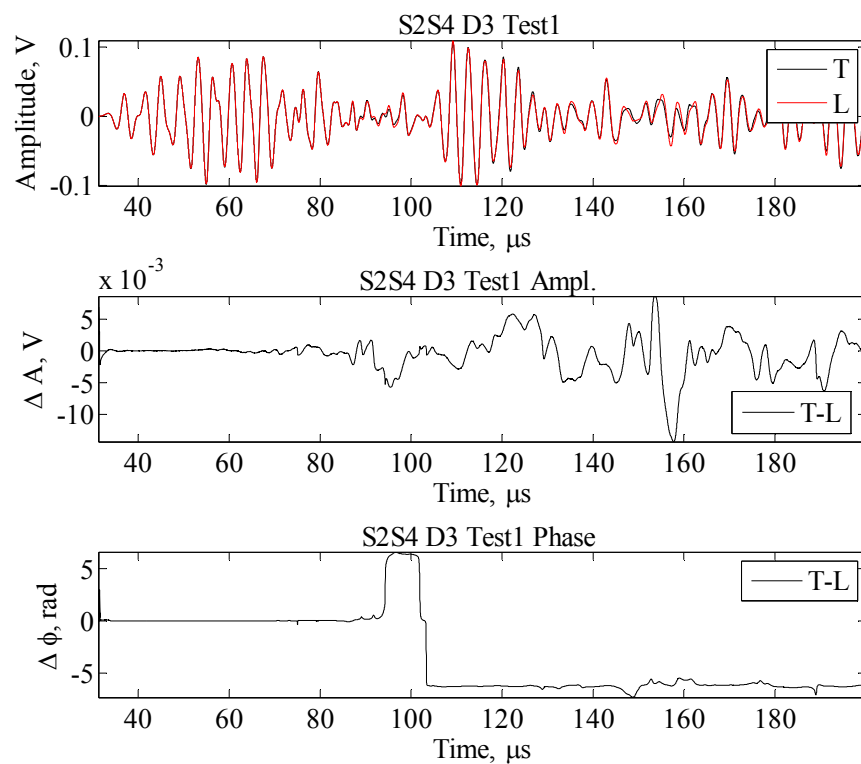
Figure 47 Sensor S2S4 signals for tight and loose bolt D3 – direct comparison.

Approved for Public Release; Distribution Unlimited.

48

4.3.4.3.   S3-S4 Wave Path

Wave propagation path between sensors S3 and S4 provides almost direct transmission of the elastic wave. Bolt D5 is slightly off this direct transmission path and its effect should be reflected at the beginning of the collected signal. The transmitted wave is a 3 count burst of 350 kHz, which was applied to study "loose" and "tight" condition of bolt D5. Reference-free phase scan method was considered, in which the burst was transmitted with 0, $\pi/2$, π, and $3\pi/2$ initial phases. To illustrate contribution of bolt D5, Figure 48 and Figure 49 present experimental results obtain in two experiments for initial 0 phase signal transmitted through "loose" and "tight" bolt D5. As it could be seen in the figures, contribution of bolt D5 is noticeable in the region of 40 µs to 60 µs, and later at 80 µs. These results were obtained in several tests, which indicate consistency of D5 manifestation.
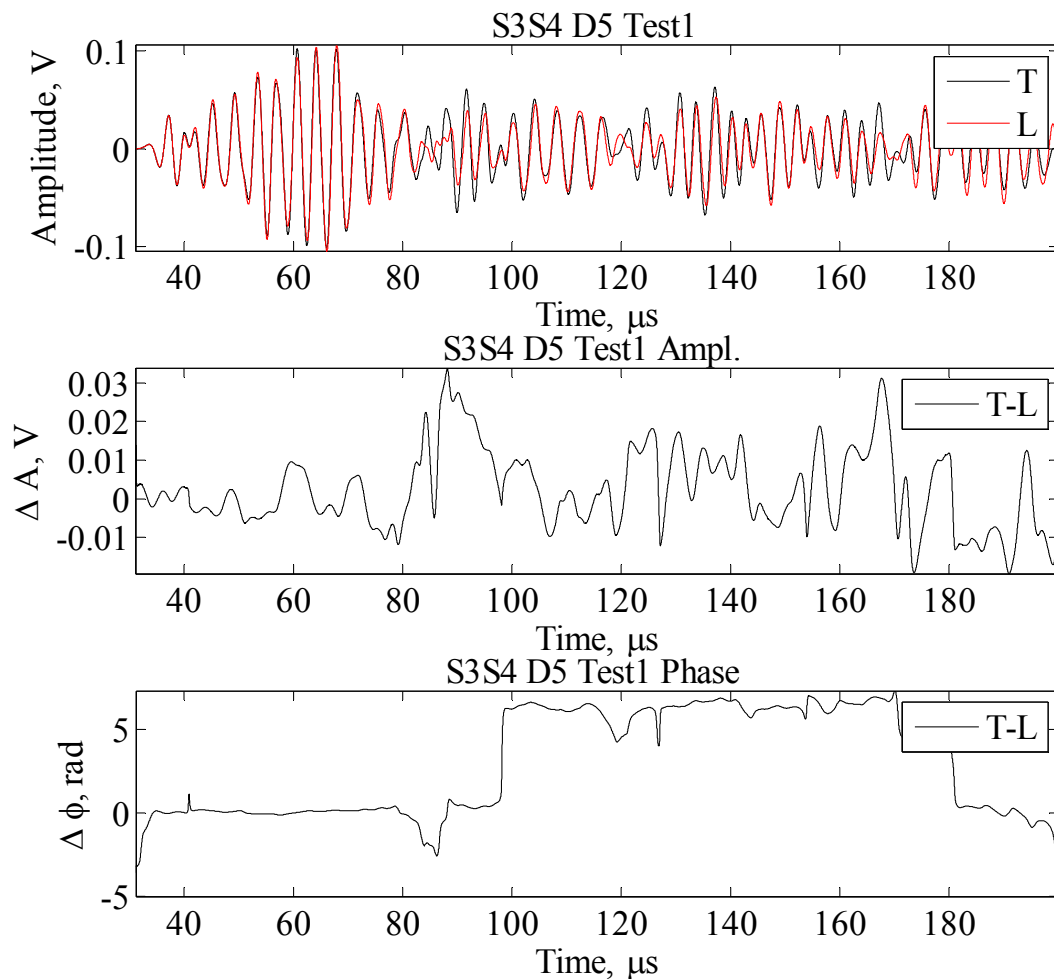
Figure 48 Sensor S3S4 signals for tight and loose bolt D5 – direct comparison Test1.
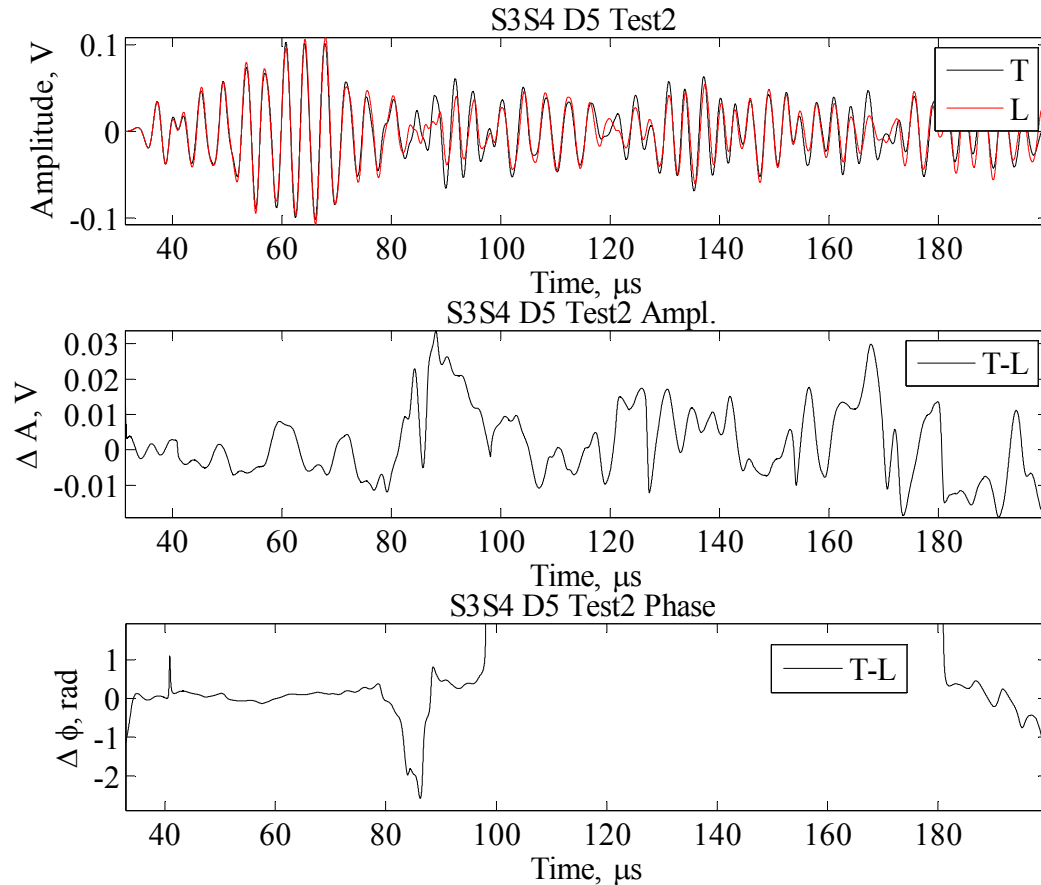
Figure 49 Sensor S3S4 signals for tight and loose bolt D5 – direct comparison Test2.

Reference-free damage detection was implemented by rotating initial phase of the transmitted signal as described above. Signals for each initial phase were recorded, Hilbert transform calculated and relevant amplitude and phase information extracted. Results for the reference-free phase scan method are presented in Figure 50 - Figure 52 for 2 tests with bolt D5 and one test with bolt D3. As it can be seen in the figures, there is practically no difference between "tight" and "loose" conditions of D5 for the amplitude feature. However, the phase feature shows some difference at 40 μs and very pronounced difference at 80 μs. Hence, if a loose bolt is located rather close to direct wave propagation path between sensors, it may be detected with reference-free phase scan method. Results for "loose" and "tight" condition of bolt D3, located much further away from direct wave propagation path between sensors, show indistinguishable differences in both amplitude and phase features. Therefore, a loose bolt located relatively far away from the direct path may not be identified using reference-free phase scan method. This result was expected because any reference-free method would show reduced sensitivity to damage when evaluated against results provided by direct comparison between "tight" and "loose" conditions, i.e. subtraction of "loose" data feature from "tight" data feature. Nevertheless, it is suggested that the reference-free method may be applicable to shorter distances and may require calibration to determine a threshold in the phase feature to distinguish between "tight" and "loose" conditions of the structural bolt.
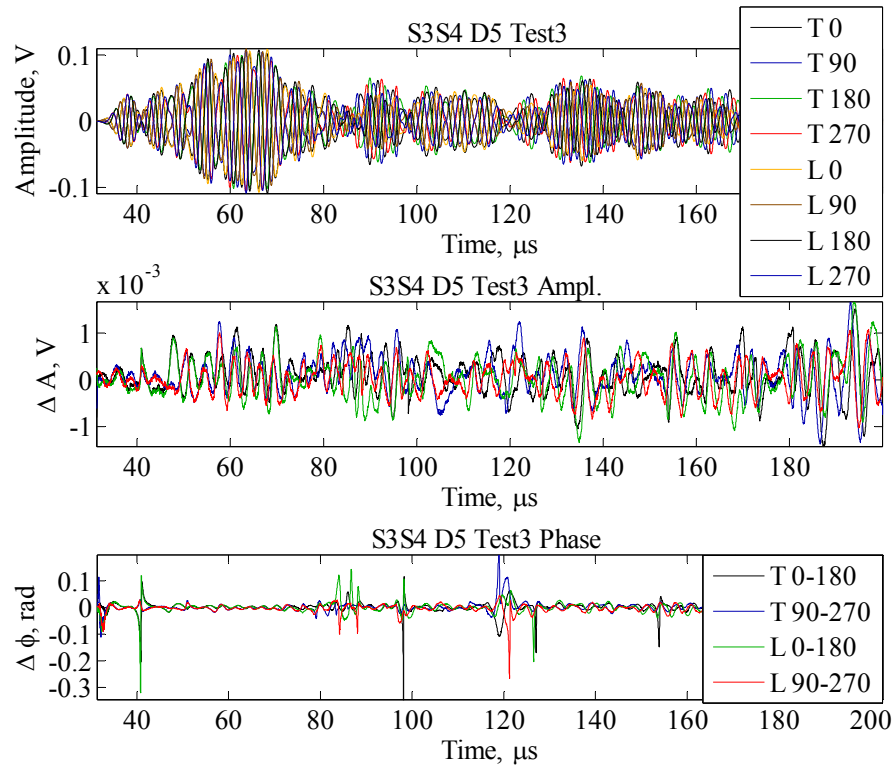
Figure 50 Sensor S3S4 signals for tight and loose bolt D5 – Test3.
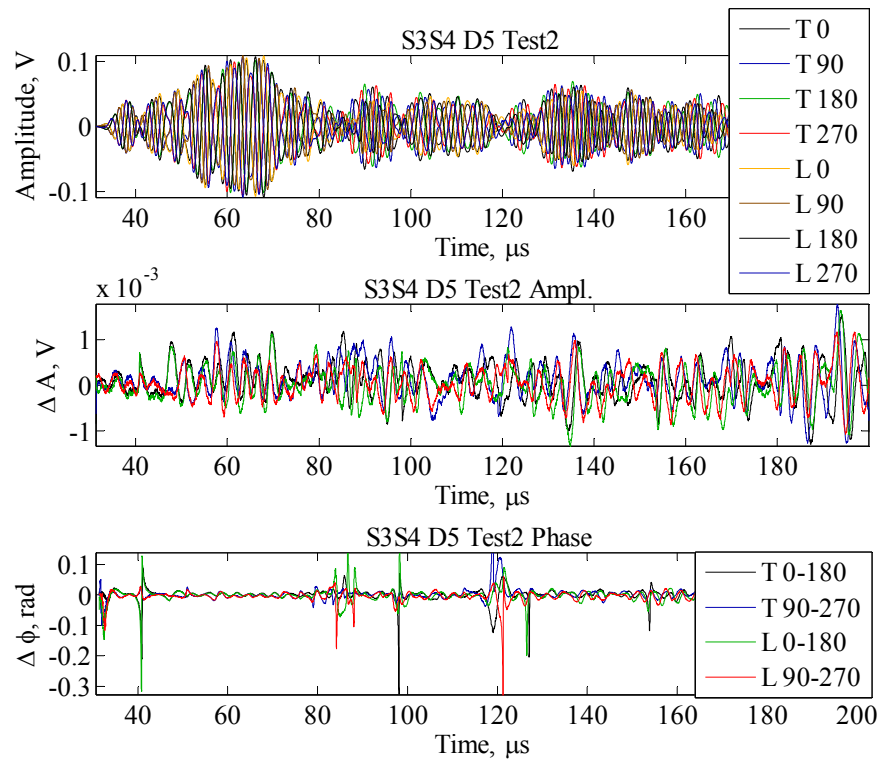
Figure 51 Sensor S3S4 signals for tight and loose bolt D5 – Test 2.
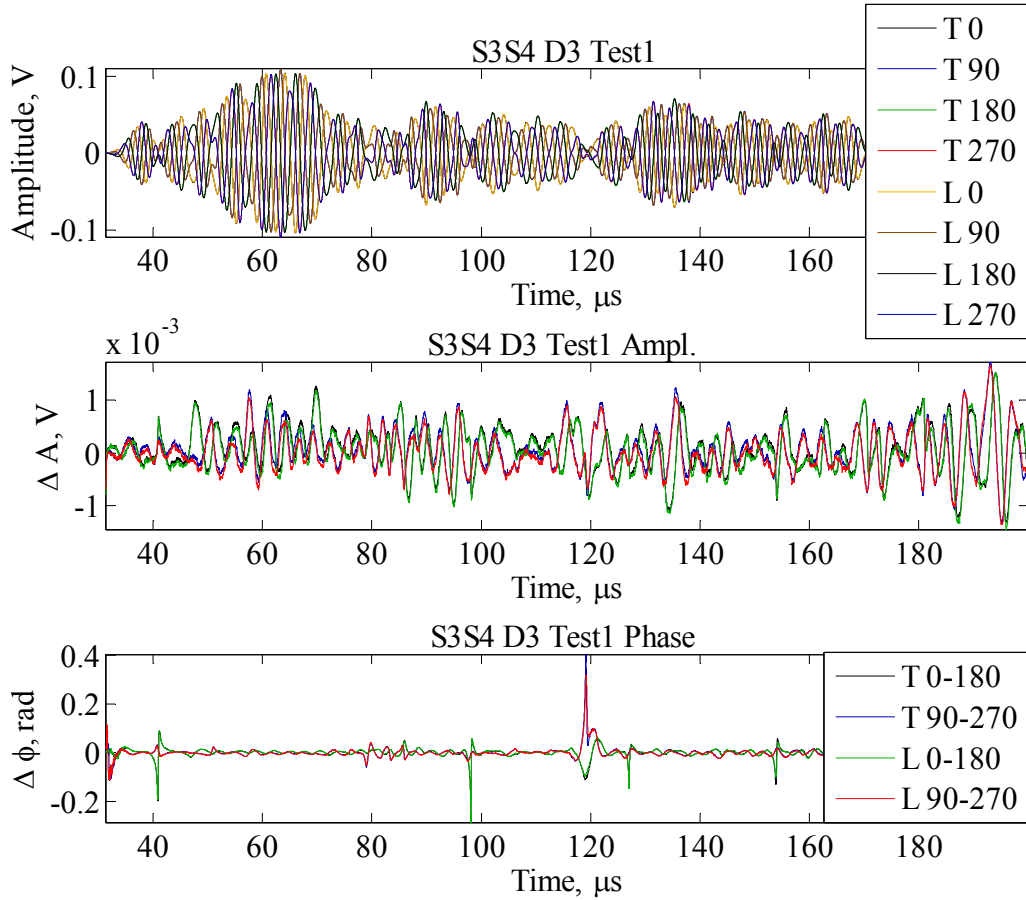
Figure 52 Sensor S3S4 signals for tight and loose bolt D3 – Test 1.

4.3.5 Standard Deviation Statistics of Reference-Free acousto-elastic satellite panel Tests

In sections above, we discussed a reference free acousto-elastic method for detection of loose bolts in a satellite panel depicted in Figure 41. Three different transmitter/receiver pairs were used in the experiment: S3S4, S3S2 and S2S4. The excitation signal was Ritec's 3-count, 300 kHz pulse with amplitude of 110 volts. Recorded data was averaged 150 times to eliminate noise in the signal. Data was collected for four different pulses with different initial phases (e.g. 0, $\pi/2$, π, $3\pi/2$). In order to further reduce the noise, experimental data was subjected to 5 points moving average filter. The experiment consisted of propagating the acoustic wave and recording the received signal first for all bolts being tightened to 35-40 in-lbs. The bolt labeled D3 was then loosened to a finger-tight, 1-5 in-lbs, and data was collected for this "loose" condition. Following this test the bolt was fully tightened again and data was collected again. The same bolt, D3, was loosened again, and once again data was taken. This process continued until ten data sets had been collected for each the "tight" and "loose" conditions. Once the tests ran for D3 were completed the experiment was run again for D5 being loose.
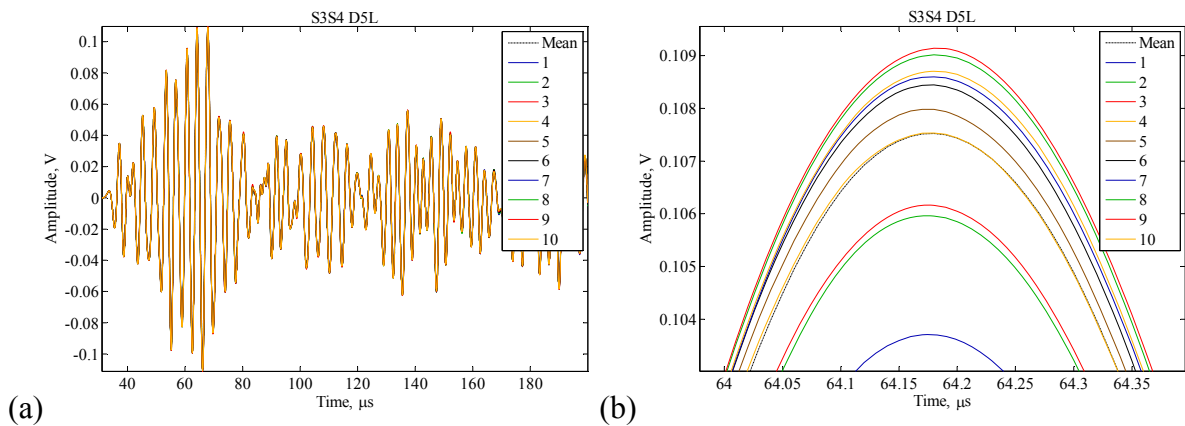
Figure 53 (a) Signals and average signal for S3S4 D5 loose; (b) zoomed in portion of the signal.

In the process of analyzing waveform's statistics, an interesting phenomenon was uncovered. It was noticed that the "loose" waveforms seemed to have more deviation between each other. A plot of all the 0 initial phase waveforms, along with their average, for the "tight" condition of S3S4 for the D5 test is shown in Figure 53a. On the first glance, the signals seem to be identical but when a portion of the graph is zoomed in on, as in in Figure 53b, the deviations in the data are clearly observed. To classify this variation the standard deviation was calculated for the collection of data sets representing "tight" condition of bolted joints. Similar procedure was then repeated for the "loose" condition.

Once standard deviations were calculated for the two conditions the plot of mean signals with associated standard deviations depicted in Figure 54 was created. By examining a zoomed portion of the graph, displayed in Figure 55, it is noticeable that most deviation occurs at the peaks of the signals. Another more interesting and useful observation is that the "loose" standard deviation is greater than that of the "tight" condition. This suggests that the loose bolt allows for more fluctuations and interface changes affecting wave propagation through the joint. A new method of loose bolt detection was then proposed based on this phenomenon.

To emphasize this observation, we plotted the magnitude of standard deviations against time. This is done in Figure 56 for the same D5 case for S3S4. The standard deviation corresponding to the "loose" case is clearly greater a majority of the time. The maximum "loose" deviation, $\sigma_{loose} = 0.0022$, is greater than the "tight" deviation, $\sigma_{tight} = 0.0016$. The average deviation of the "loose" case was calculated to be 0.0004382. This value is 13.81% higher than the $avg\ \sigma_{tight} = 0.0004382$.

The trend of the "loose" case having a greater standard deviation than the "tight" case remains true for all the tests. The standard deviation results for the remaining tests are shown graphically in Figure 57-Figure 61. These results support the proposed technique of using standard deviations of a series of collected data to determine whether or not a bolt is loose.

Approved for Public Release; Distribution Unlimited.
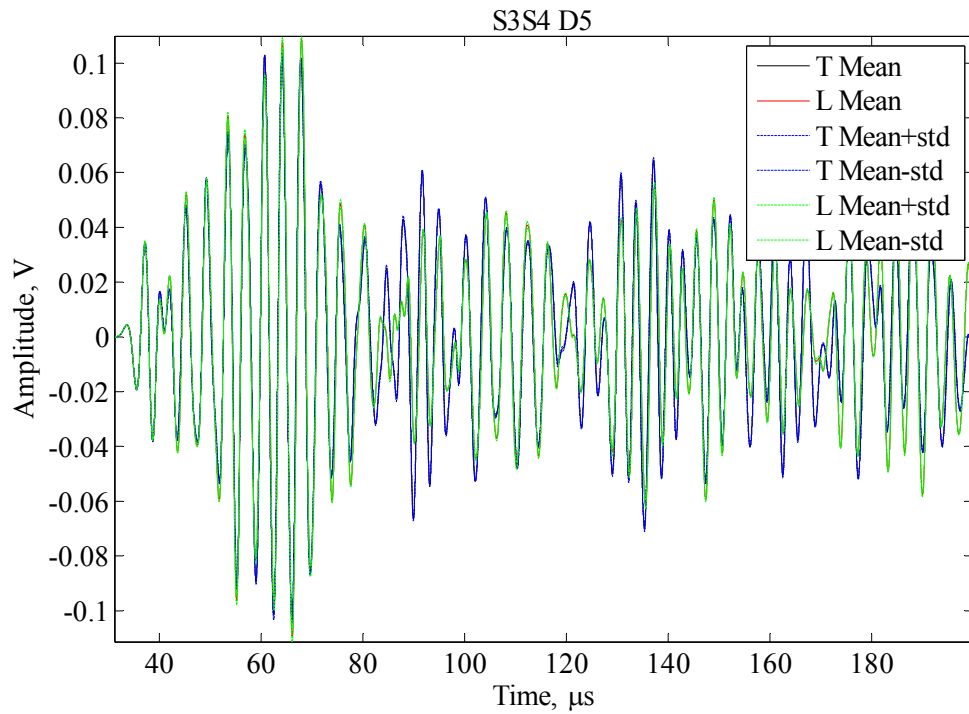
Figure 54   Average signals with standard deviation for S3S4 D5 "loose" and "tight" conditions
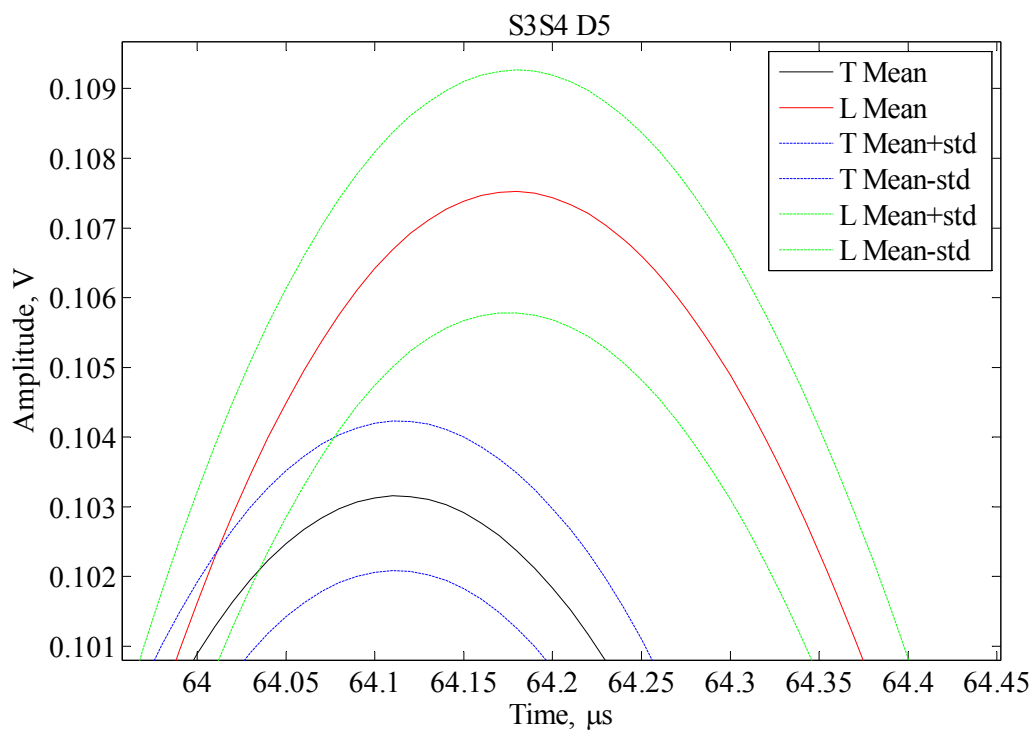
Figure 55   Zoomed in portion of average signals with standard deviation for S3S4 D5 "loose" and "tight"

Approved for Public Release; Distribution Unlimited.
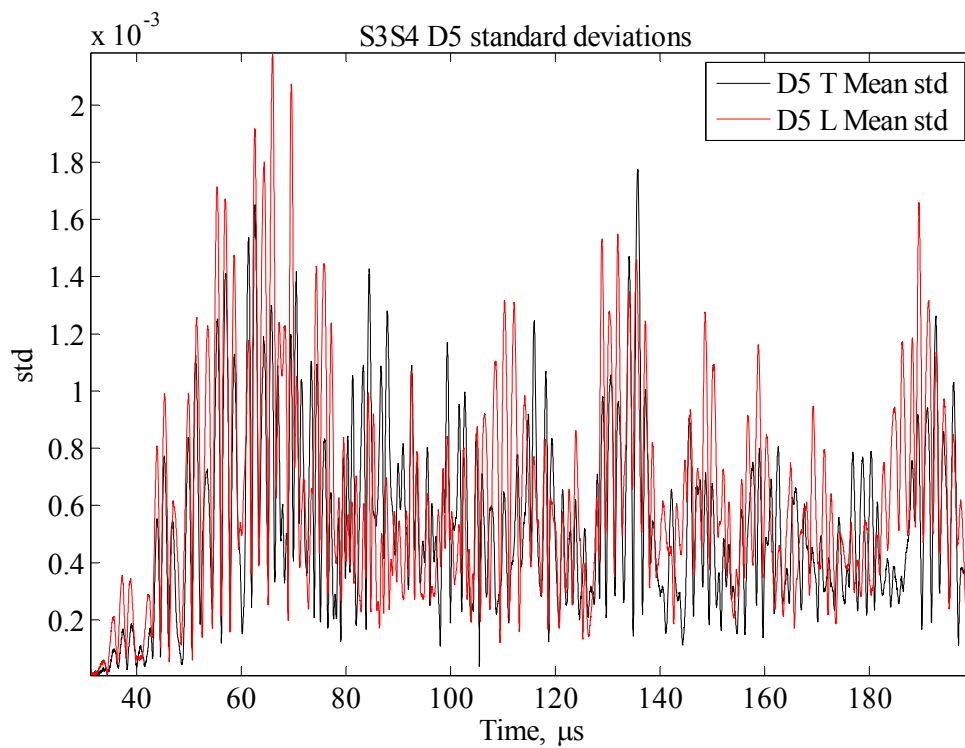
Figure 56   Standard deviations for S3S4 D5 test.
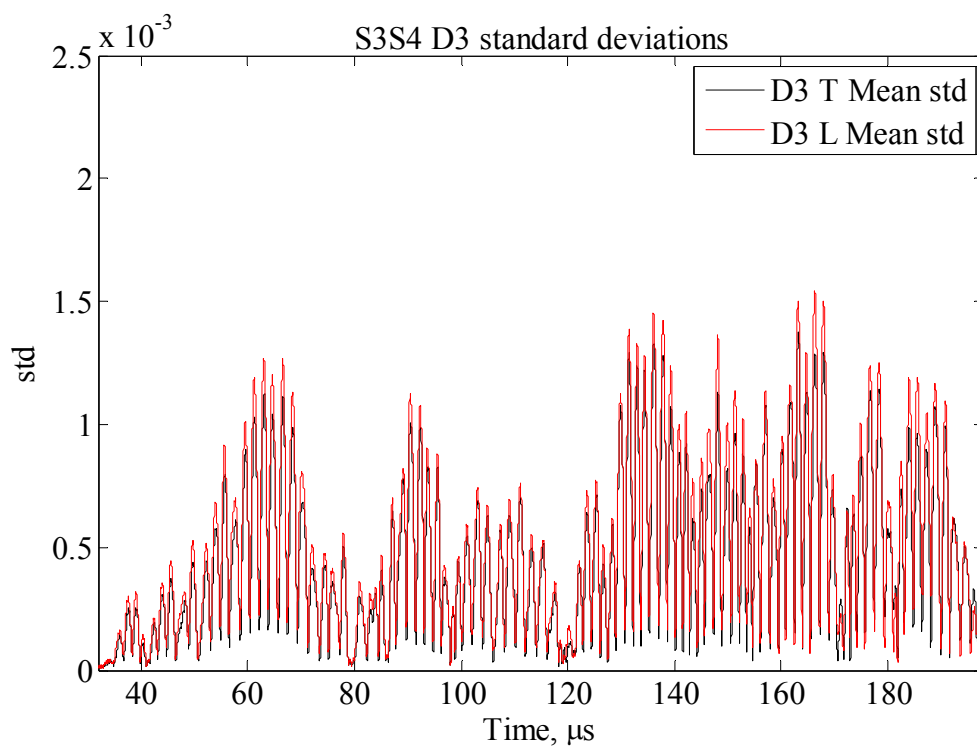
Figure 57   Standard deviations for S3S4 D3 test.
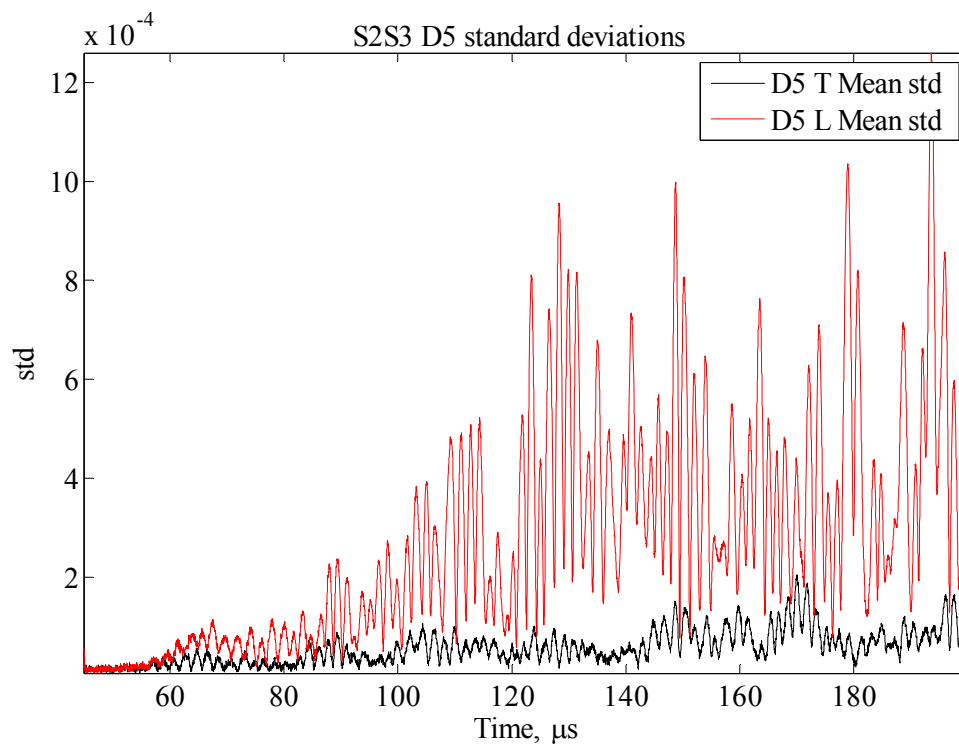
Figure 58   Standard deviations for S2S3 D5 test.
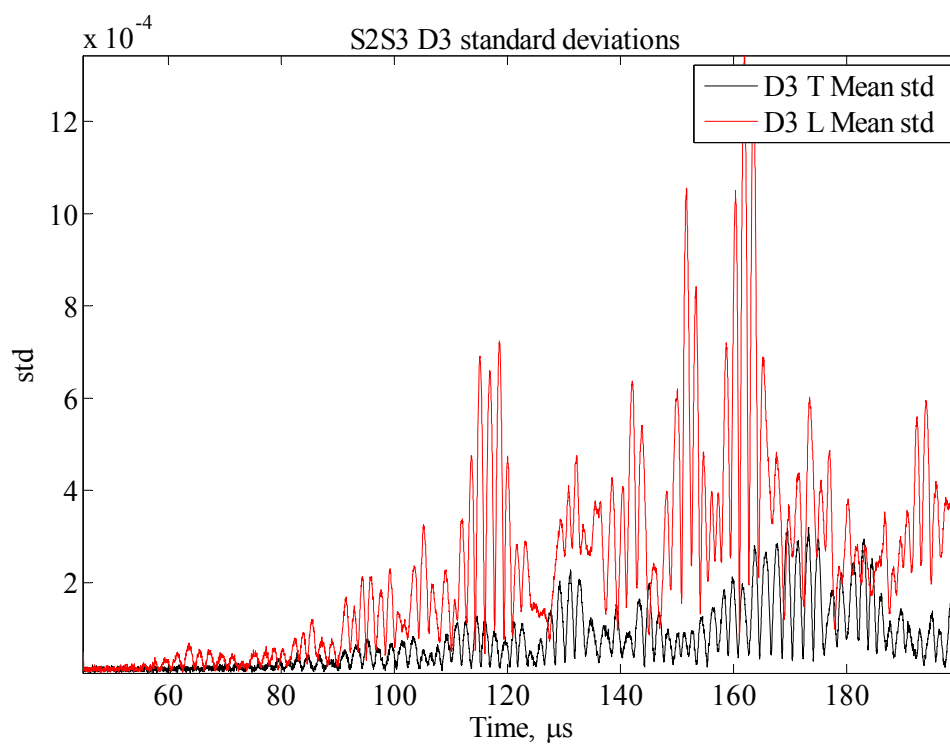
Figure 59   Standard deviations for S2S3 D3 test.
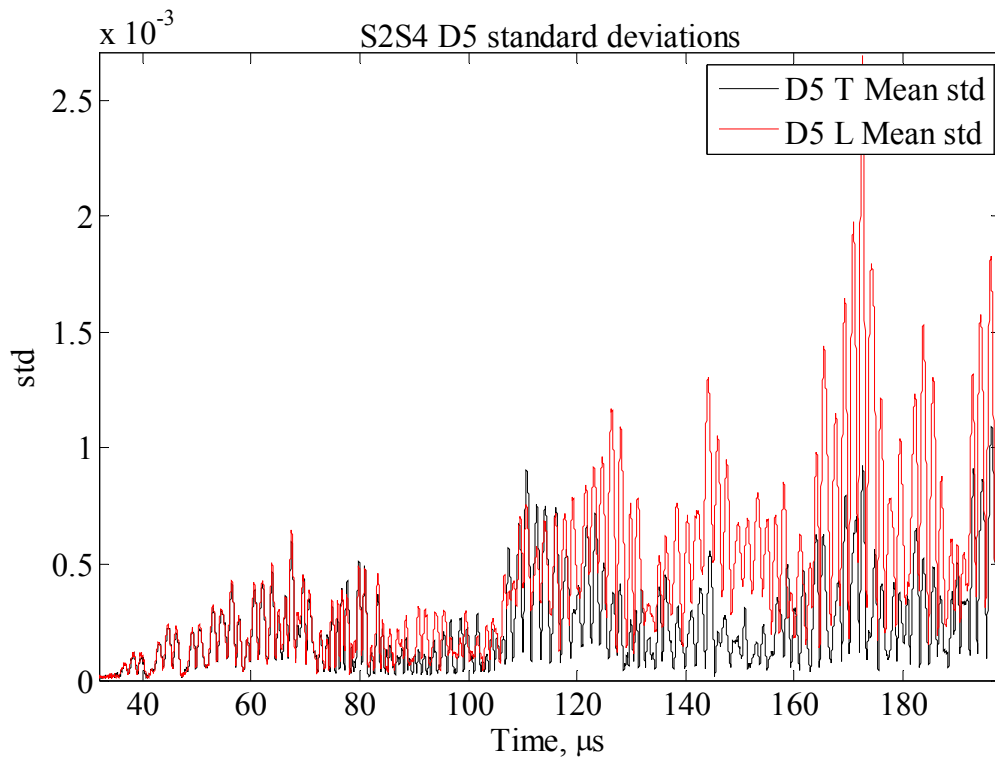
Figure 60   Standard deviations for S2S4 D5 test.
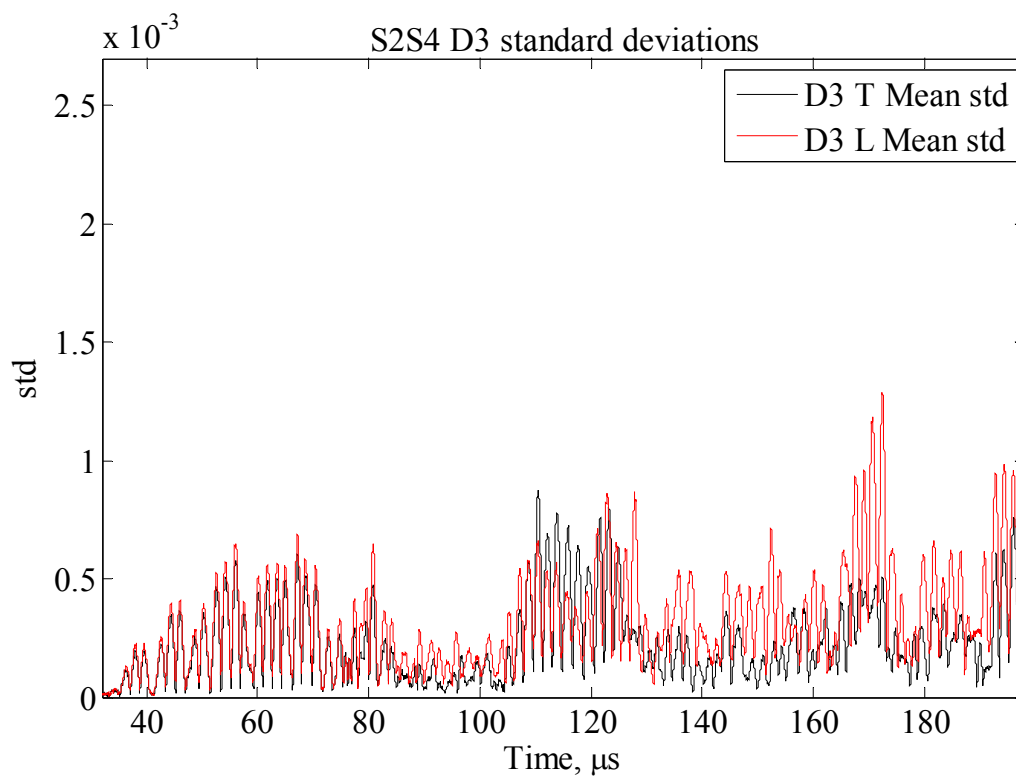
Figure 61   Standard deviations for S2S4 D3 test.

The average and maximum standard deviations from each conducted test are displayed in Table 4 and Table 5 respectively. In addition, the tables show the percent increase from the "tight" to "loose" condition.

Table 4   Average standard deviations for "loose" and "tight" conditions for each sensor path and bolt location.

Path	avg std T	avg std L	% average std increases for loose
S3S4 D3	0.0004382	0.00049875	13.81789137
S3S4 D5	0.00052447	0.0006284	19.8161954
S2S4 D3	0.00022876	0.00032561	42.33694702
S2S4 D5	0.00023931	0.00044743	86.96669592
S2S3 D3	0.000074216	0.00023244	213.1939204
S2S3 D5	0.000056553	0.00027568	387.471929

Table 5   Maximum standard deviations for "loose" and "tight" conditions for each sensor path and bolt location.

Path	max std T	max std L	% max std increases for loose
S3S4 D3	0.0014	0.0015	7.142857143
S3S4 D5	0.0018	0.0022	22.22222222
S2S4 D3	0.00031929	0.0013	307.1533715
S2S4 D5	0.000204	0.0013	537.254902
S2S3 D3	0.00087616	0.0013	48.37472608
S2S3 D5	0.0011	0.0027	145.4545455

4.4 Experimental Validation of the Acousto-Elastic Method on PNP Satellite

4.4.1 Description of NMT Experiments on the PNP Satellite

4.4.1.1. Layout of Experimental Sample

The sample in the experiments is a flight-like PNP satellite panel, which contains actual components necessary for satellite operation. The testing was conducted on an isogrid panel containing three components illustrated on Figure 62 below. The components were bolted to the surface of the panel. The isogrid panel was connected to another isogrid panel through two bolted joints each featuring three bolts.

Piezoelectric wafers (PZT) with UNF electrodes were bonded to the isogrid panels using 3M 2216 epoxy. Originally, nine sensors were attached to the panel. However, during high-power acousto-elastic testing, two sensors showed significant signs of damage, and were therefore not used in the tests described herein. To compensate for the damaged sensors, six additional sensors were attached to the plate. The sensors were placed on top of small pieces of Kapton tape, and were bonded to the tape with cyanoacrylate adhesive. This installation was anticipated to reduce the likelihood of electric leakage into the plate and to reduce the likelihood of sensor breakage. Additionally several sensors were staked to the plate, and are indicated in the figure.
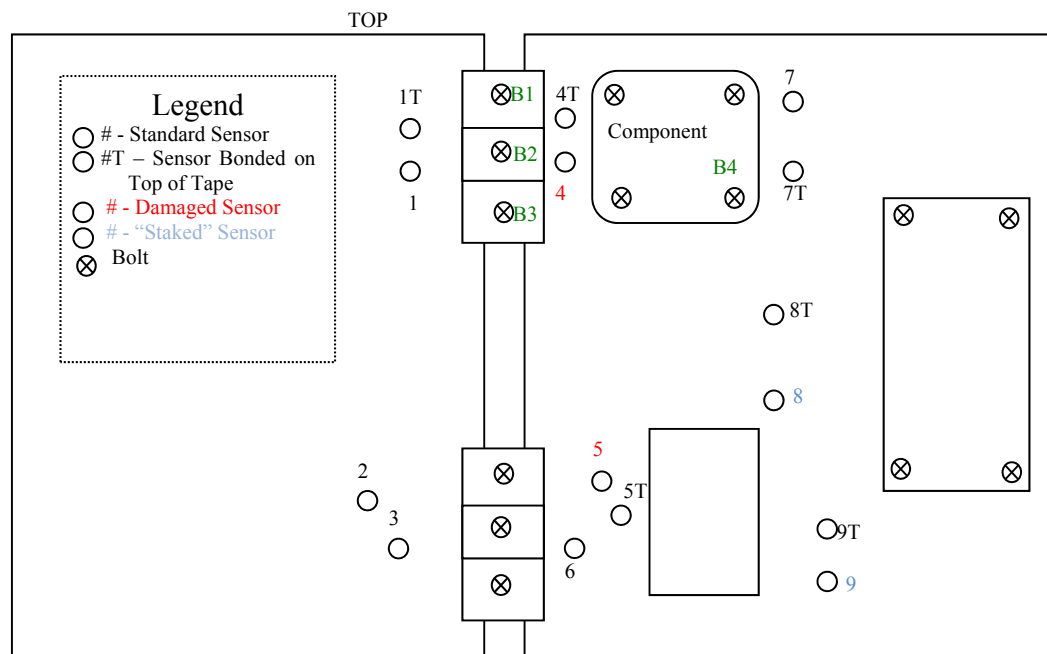
Figure 62 Layout of experimental sample in PNP satellite tests.

4.4.1.2. Description of experiments.

4.4.1.2.1. Initial Phase and Amplitude Scans

The initial tests were intended to investigate performance of phase and amplitude scan techniques in evaluating the torque on the bolts in three bolts joint. Five different torque settings were used: tight (24 in-lbs of torque), completely loosened (but not removed), 8 in-lbs, 16 in-lbs, and 24 in-lbs (or re-tightened). To achieve consistent levels of torque, the bolts were loosened completely before adjusting to the new torque value. In other words, when going from 16 in-lbs to 24 in-lbs, the bolt was loosened completely and then tightened to 24 in-lbs. The transmitter-receiver pair for this set of tests was 4T as the transmitter and 1 as the receiver. The received signals were not subjected to filtering and smoothing. Instead, a received signal was averaged 100 times to yield a relatively clean waveform recorded for further processing.

The phase scanning consisted of utilizing a transmitted signal with different initial phases: 0 degrees, 90 degrees, 180 degrees, and 270 degrees. In the amplitude scan, five amplitude settings were used: -22, -12, -4.33, 0.67, and 5.33 (Auto-Fine). Received and transmitted signals were recorded for each torque value. The frequency used was 290 kHz. However, several signals with the excitation frequency 300 kHz were recorded due to an issue with the Explorer_2.vi unintentionally reconfiguring the RITEC system. In subsequent tests, the RITEC settings were loaded into the RITEC control software after the Explorer_2.vi was started and running to ensure proper software setting.

In experiments, a receiver gain was set to 38 dB with the exception of the loose bolt case, where the gain was increased to 50 dB because of drastically reduced signal amplitude. For the phase scan measurements, a signal amplitude setting of -20 (Auto-Fine) was used. All signals in the amplitude scan were signals with 0 degrees initial phase. The record length for each recorded signal was 0.00015s, at 100 Ms/sec.

4.4.1.2.2. Shaker Phase and Amplitude Scans

This test was conducted with the satellite mounted on a large shaker. Two damage scenarios were explored. In the first test, a single bolt (the lowest bolt) in the top 3-bolts bolted joint was loosened completely. In the second test, a B4 bolt on the component (marked on the diagram in Figure 62) was loosened. Between each case, the entire satellite was shaken using the shaker for about 3-5 minutes.

In the on-shaker tests, two sensor pairs (4T to 1 and 4T to 7) were used to transmit and receive elastic waves. For the 4T to 1 sensor pair, the same signal settings were used as in the previous tests for initial phase and amplitude scans. For the 4T to 7 set, the frequency was changed to 320 kHz, and 50 averages were taken instead of 100. The rest of the signal settings were similar to previous tests. Experimental configurations and respective sensor pairs are summarized in Table 6. It should be noted that the sample was left overnight between the final two test conditions.

Table 6   Experimental sample condition and utilized sensors.

Sample Condition	4T-1 Used	4T - 7 Used
Undamaged (Before First Shake)	Yes	No
Undamaged (After First Shake)	Yes	Yes
Loose Joint Bolt	Yes	No
Joint Bolt Repaired	Yes	Yes
Loose Component Bolt	No	Yes
Component Bolt Repaired	No	Yes

4.4.2   Results of the PNP Satellite Pre-Shaker Tests

Experimental results discussed in this section were obtained from the PNP satellite in a laboratory environment and NOT mounted on a shaker.

4.4.2.1.   Acousto-Elastic Measurements with Baseline (Known Undamaged Condition)

The acousto-elastic response of a bolted joint connecting two panels of the PNP satellite is presented in Figure 63 and Figure 64. In the experiments three bolts in the joints were subjected to different torque levels and elastic wave signals were recorded for each condition of the joint. Figure 63 indicates a substantial difference between "undamaged" and "all bolts loose" cases. The difference is manifested in signal amplitude reduction and phase shift. Minor differences were observed for "undamaged" and "24 in-lbs" (same torque level as "undamaged") experimental scenarios. Additional details on the performance of the acousto-elastic method could be inferred from Figure 64 showing consistent phase shift for torque levels of 8, 16, and 24 in-lbs. Hence, not only "tight" and "loose" conditions can be inferred using the acousto-elastic method applied to PNP satellite, but also evaluation of the actual torque level on bolts in the joint is possible. The experimental data confirms utility of the acousto-elastic method for assessment of structural integrity of the PNP satellite.
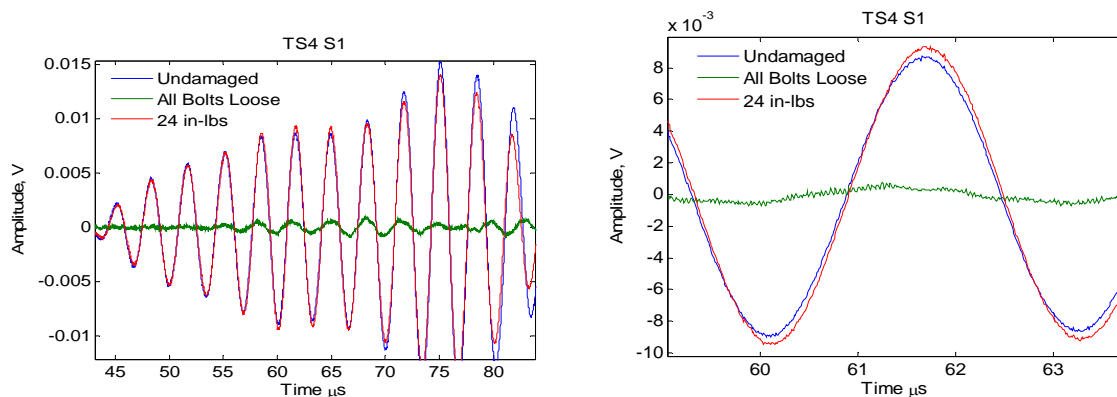
Figure 63 Elastic wave signals collected for different conditions of the bolted joint on the PNP satellite.
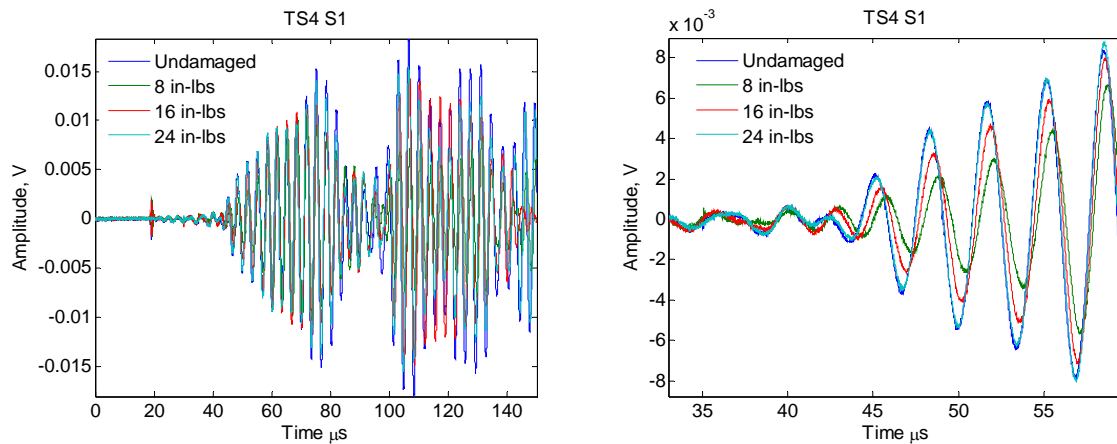
Figure 64 Elastic wave signals collected for the PNP satellite bolted joint subjected to different torque levels.

4.4.2.2. Baseline-Free Acousto-Elastic Phase Scan Method

The previously described baseline-free acousto-elastic phase scan method was utilized to assess integrity of the bolted joint connecting two panels of the PNP satellite. Signal processing for the phase scan method was similar to the thin aluminum panels test discussed above. It consisted of summing out-of-phase signals and calculating spectrum of the difference. Both, difference signals and their spectrums are given in Figure 65 to Figure 68 for different levels of torque in the joint. Figure 65 shows results for "tight" conditions only. Very small changes in temporal and spectral signatures corresponding to "tight" conditions were observed. Figure 66 and Figure 67 show minor differences in spectral amplitude and content, but these differences are not significant enough to warrant reliable detection. Finally, Figure 68 indicates notable spectral differences between signals corresponding to "tight" and "all bolts loose" conditions. However, the main difference is in dominant frequencies of the signal rather than in amplitude of a particular spectral component.
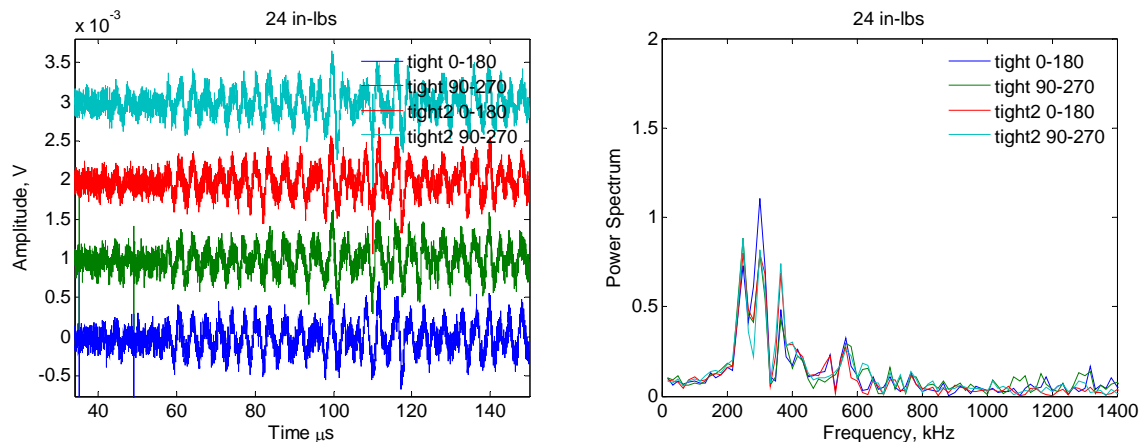
Figure 65 Signal differences and their spectrum for out-of-phase records: 24 in-lbs torque condition.
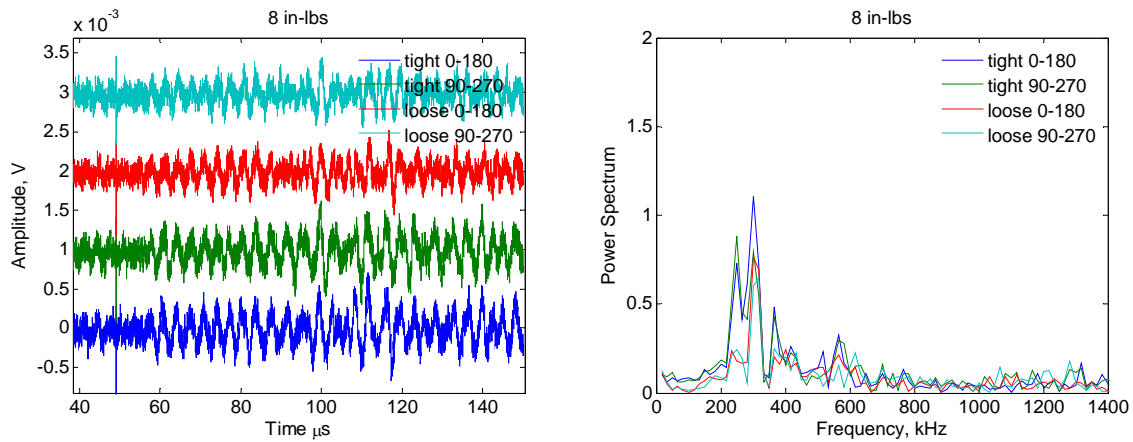
Figure 66 Signal differences and their spectrum for out-of-phase records: 8 in-lbs torque condition. "Tight" data corresponds to torque level of 24 in-lbs.
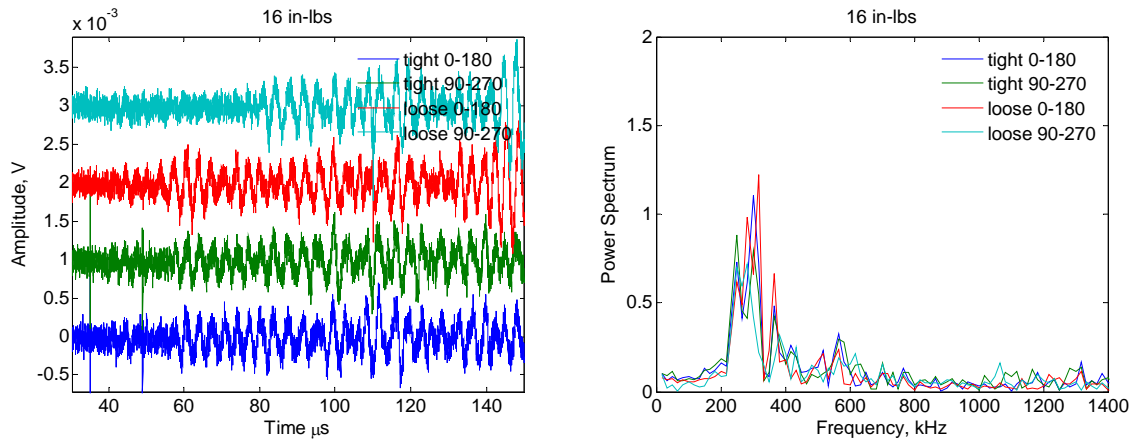
Figure 67 Signal differences and their spectrum for out-of-phase records: 16 in-lbs torque condition. "Tight" data corresponds to torque level of 24 in-lbs.
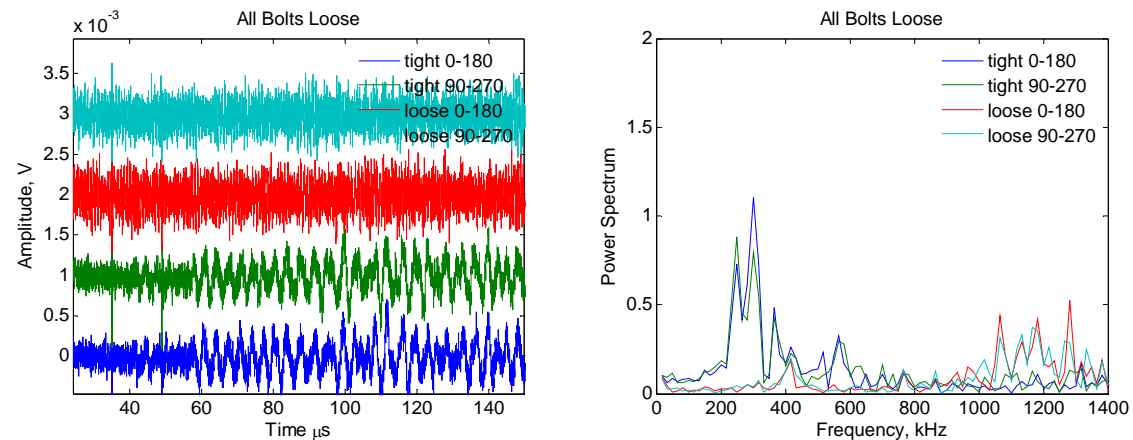
Figure 68 Signal differences and their spectrum for out-of-phase records: all bolts loose torque condition. "Tight" data corresponds to torque level of 24 in-lbs.

4.4.3 Results of the PNP Satellite ON-Shaker Tests

4.4.3.1. Acousto-Elastic Measurements with Baseline (Known Undamaged Condition).

This section describes application of the acousto-elastic method for assessing condition of PNP satellite bolted joints before and after the shaker test. The "damaged" condition in the experiment was simulated by loosening the lowest bolt in a 3-bolts joint connecting panels of the PNP satellite. Figure 69 shows signal records collected from the sensor pair TS4-S1. The zoomed-in portion of the figure indicates notable similarities for signals corresponding to "tight" condition. Amplitude and phase of the signal representing the "loose bolt" case deviates substantially from the "tight" condition and allow for detection of the loosened bolt.
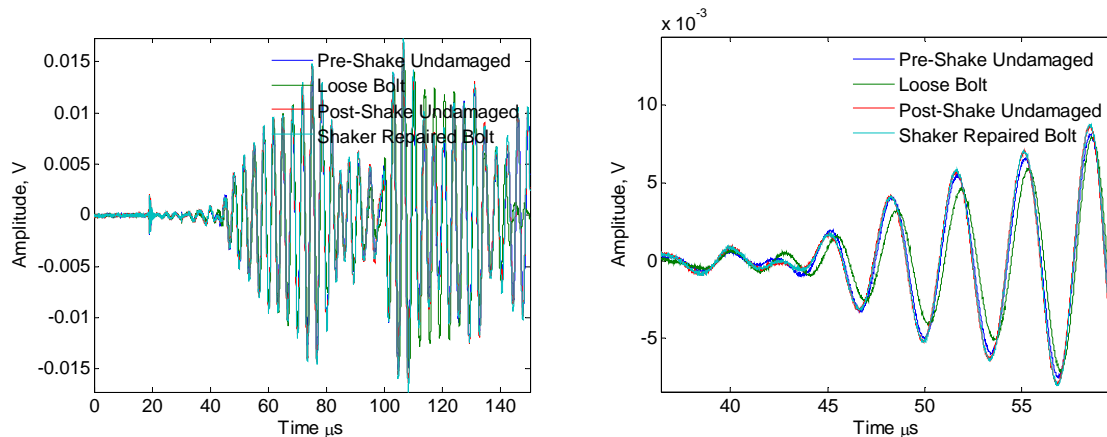
Figure 69 TS4-S1 elastic wave signals corresponding to different conditions of the PNP satellite bolted joint subjected to different torque levels.

In a next series of tests, an effect of loosening a bolt connecting one of the externally attached components was investigated. Sensor TS4 was used as a transmitter and sensor S7 as a receiver of elastic waves. Figure 70 illustrates data records corresponding to "damaged components" and three "undamaged" scenarios. It is interesting to note that initial waveform at 55 microseconds does not show signal phase differences associated with the damaged condition. However, discrepancies between signals become pronounce later at approximately 70 microseconds. It is believed that signal differences were observer later in time because the loosened bolt was not directly of the wave propagation path between sensors. Although the "damaged" case is clearly distinguishable from "undamaged" cases, the difference is rather small, which may be related to specific of component mounting on the satellite and the panel's structure. It is recommended that deviation of phase in "undamaged" cases needs to be taken into account while analyzing acousto-elastic response and establishing damage detection criteria.
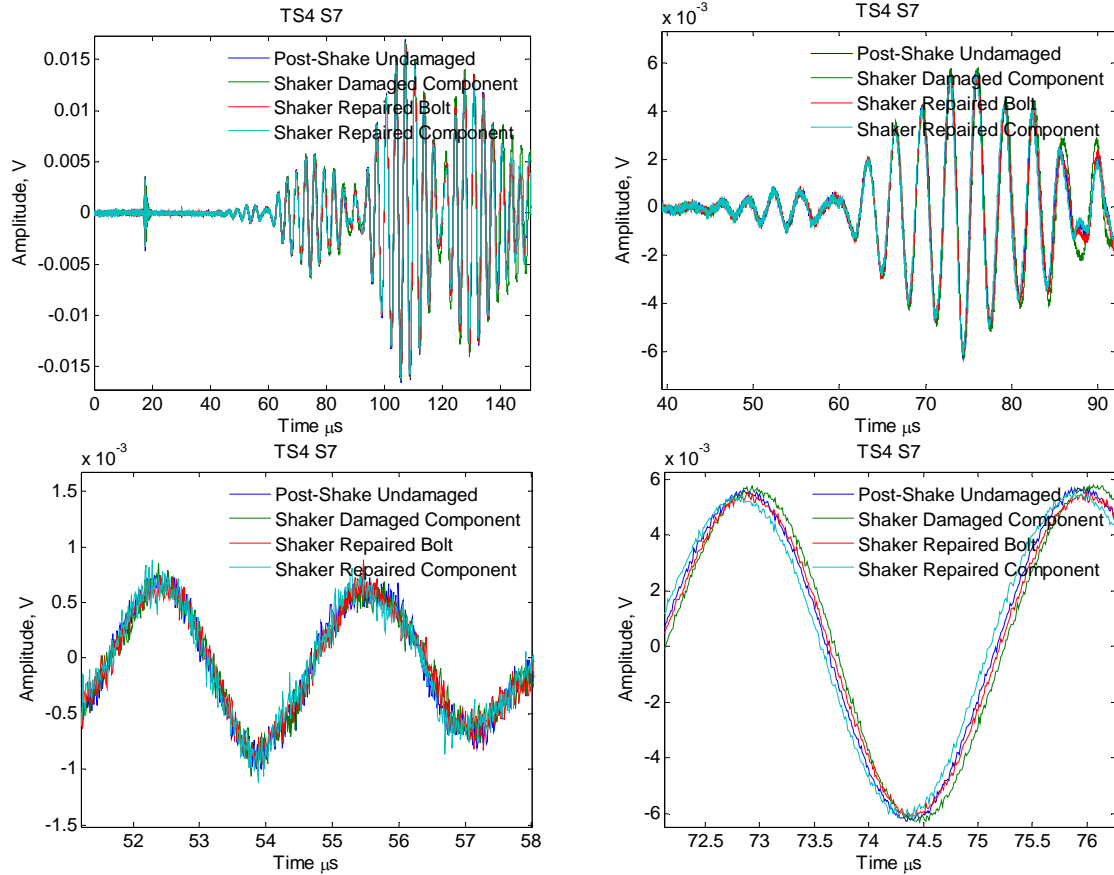
Figure 70 TS4-S7 elastic wave signals corresponding to different conditions of the PNP satellite bolted joint subjected to different torque levels.

4.4.3.2. Baseline-Free Acousto-Elastic Phase Scan Method for ON-Shaker Tests

The baseline-free acousto-elastic phase scan method was applied to assess structural integrity of PNP satellite panels positioned on a shaker. Two damage scenarios were explored: (a) loosening of lower of 3 bolts in the joint (B3) connecting the panel (sensors TS4-S1 were used in this case) and (b) loosening bolt B4 on the component attached to the satellite panel (sensors TS4-S7 were used in this case). Experimental conditions were similar to those described in the preceding section: (1) one damaged case and pre-shake, post-shake, and repaired undamaged cases for test with sensors TS4-S1 (2) one damaged case and three undamaged cases for test with sensors TS4-S7. Signal processing consisted of calculating the difference of out-of-phase signal pairs (0-180 degrees and 90-270 degrees) and inferring the power spectrum of these differences. Experimental results for sensors TS4-S1 are presented in Figure 71 through Figure 73 and for sensors TS4-S7 in Figure 74 through Figure 76. The data presented for sensors TS4-S1 indicates some potential for inferring the damaged condition, but it may not be used reliably in its current form. Undamaged conditions show similarities in the calculated responses. For the sensor pair TS4-S7, however, the phase-scan method fails to distinguish damaged and undamaged conditions,

which is of no surprise as even the acousto-elastic method with the baseline show small phase changes for these cases.
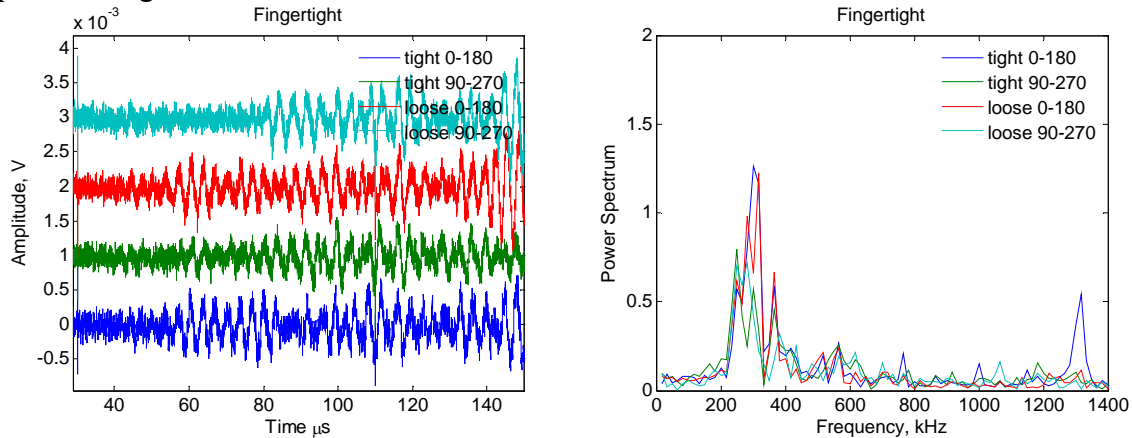
Figure 71 TS4-S1 signal differences and their spectrum for out-of-phase records. "Loose" is finger-tight torque condition. "Tight" data corresponds to pre-shaking condition at 24 in-lbs.
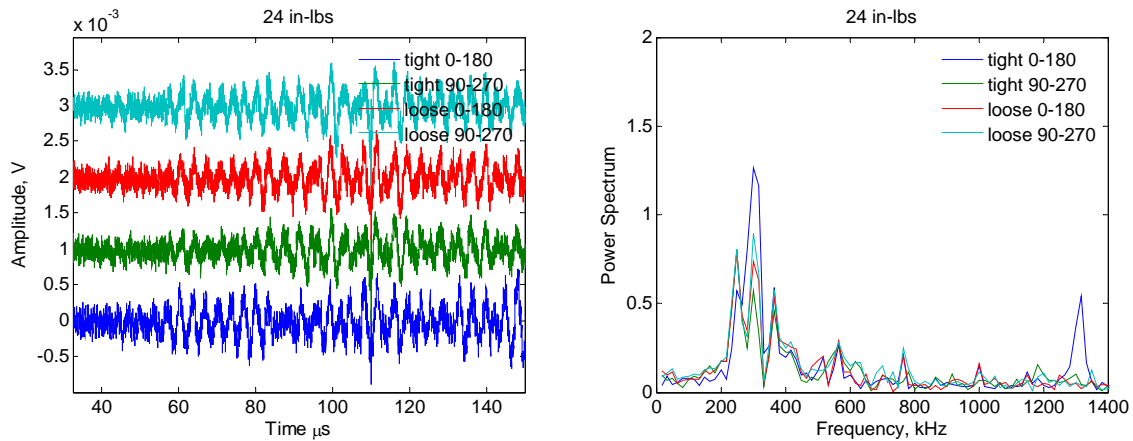
Figure 72 TS4-S1 signal differences and their spectrum for out-of-phase records. "Loose" is post-shaking condition at 24 in-lbs torque. "Tight" data corresponds to pre-shaking condition at 24 in-lbs.
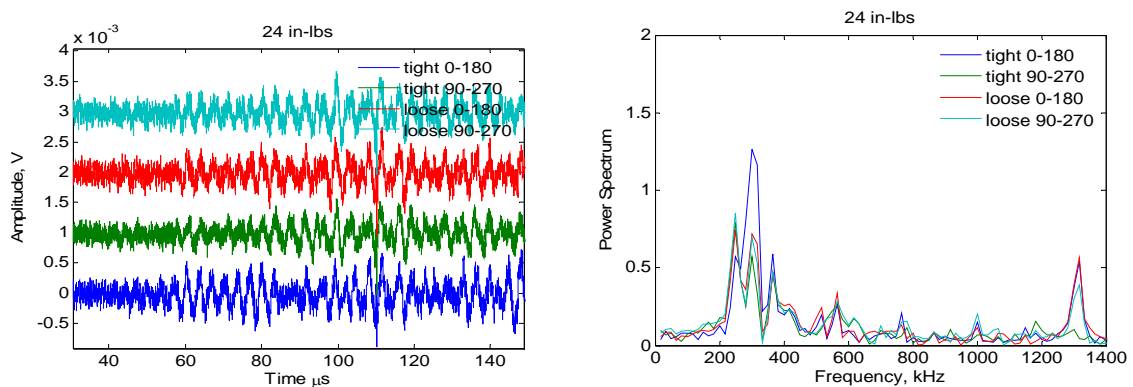
Figure 73 TS4-S1 signal differences and their spectrum for out-of-phase records. "Loose" is repaired bolt tightened to 24 in-lbs torque. "Tight" data corresponds to pre-shaking condition at 24 in-lbs.
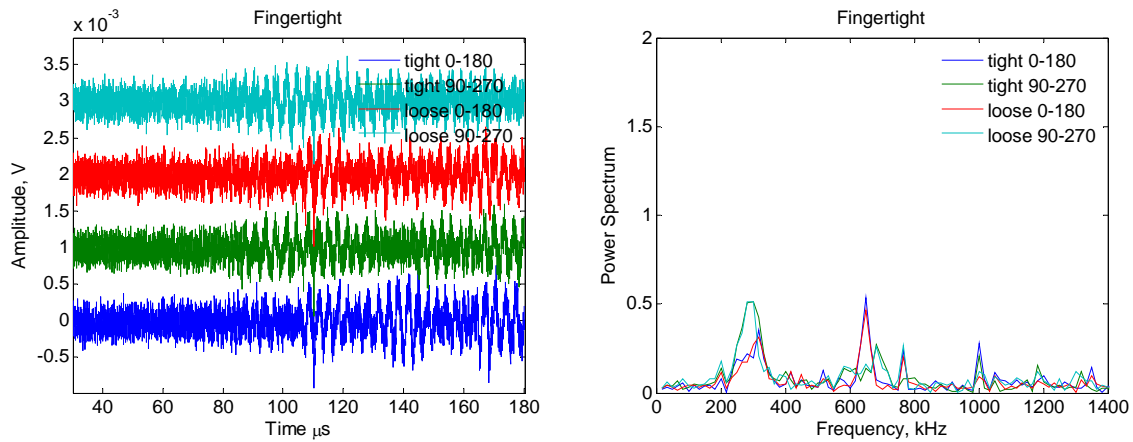
Figure 74 TS4-S7 signal differences and their spectrum for out-of-phase records. "Loose" is a finger-tight bolt in "damaged component". "Tight" data corresponds to pre-shaking condition at 24 in-lbs.
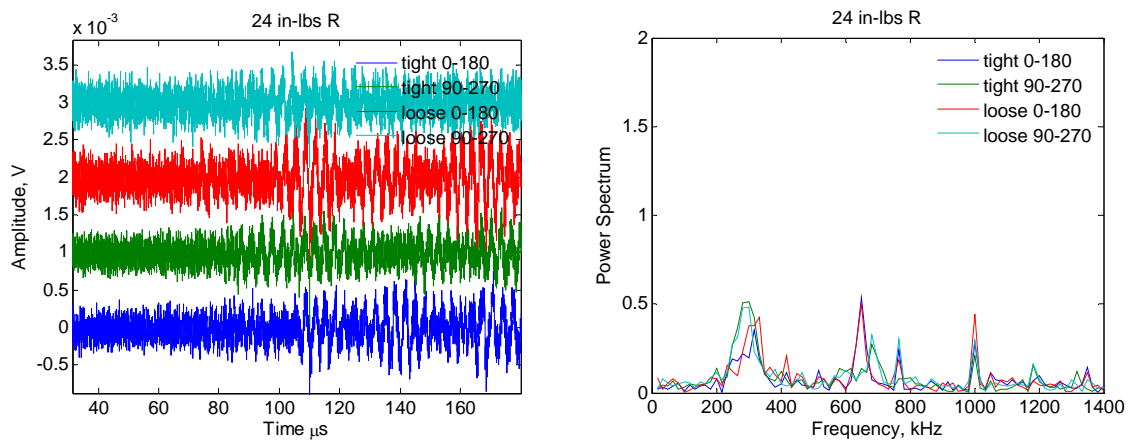
Figure 75 TS4-S7 signal differences and their spectrum for out-of-phase records. "Loose" is a repaired component condition. "Tight" data corresponds to pre-shaking condition at 24 in-lbs.
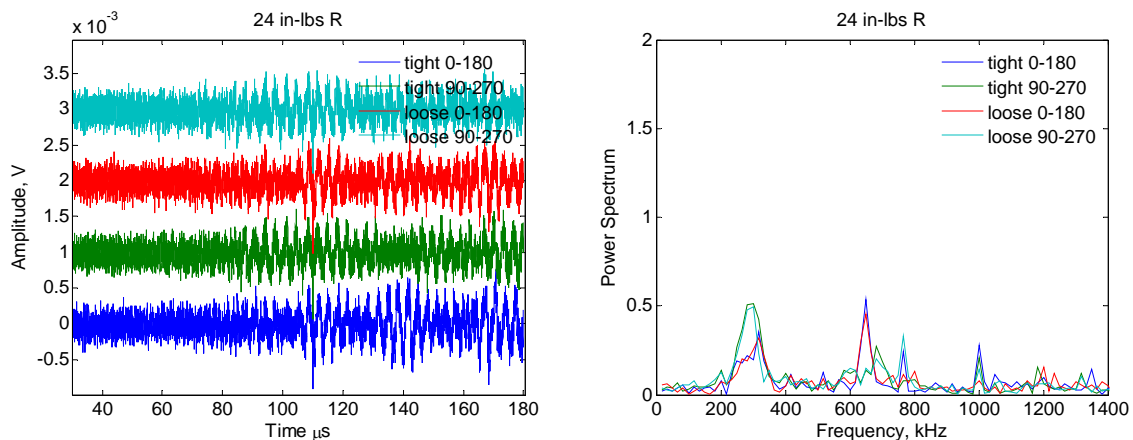
Figure 76 TS4-S7 signal differences and their spectrum for out-of-phase records. "Loose" is a repaired bolt condition. "Tight" data corresponds to pre-shaking condition at 24 in-lbs.

4.4.4 Electro-mechanical impedance thickness resonance measurements on the PNP Satellite panels

Previous studies indicated utility of the electro-mechanical impedance (EMI) method for assessment of structural integrity of satellite panels. Typically, EMI explores structural dynamic signature in the 50 kHz to 500 kHz frequency range. It is in this range that PWAS also have axial resonances may contribute into the structural dynamic signature if sensor is de-bonded. In this section, we explore a variation of the EMI technique that considers thickness rather than axial resonances of PWAS. It is possible that the coupled structure-sensor dynamics at high frequencies (MHz) could have sensitivity to structural damage. In this case, the same PWAS could offer two orthogonal damage signatures in kHz and MHz frequencies. To verify our assumption to investigate performance of the thickness resonance EMI method, we conducted a test with the sensor S1 (see Figure 62 for details).
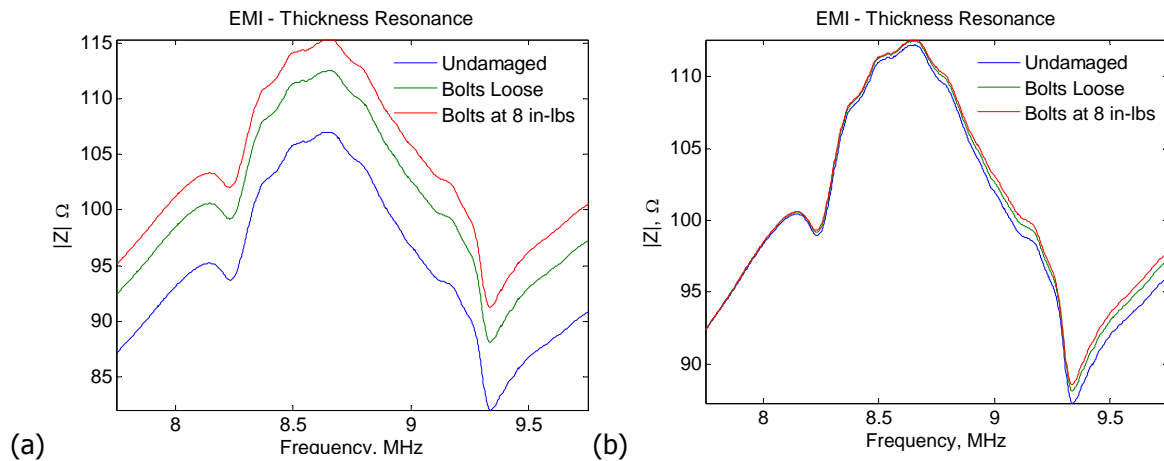
Figure 77 Electro-mechanical impedance signatures for three experimental conditions of the bolted joint on PNP satellite panels: (a) raw impedance data, (b) normalized impedances.
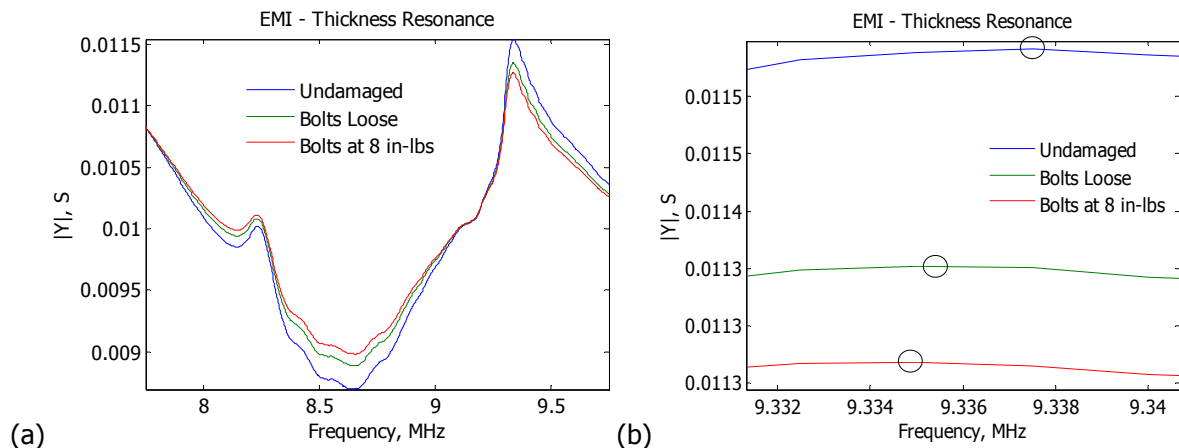
Figure 78 Electro-mechanical admittance signatures for three experimental conditions of the bolted joint on PNP satellite panels: (a) normalized admittance data, (b) zoom into the resonance region.

Impedance of the sensor was measured with HP4194A impedance analyzer in the frequency range of 7.5 MHz to 10 MHz for three conditions of the 3-bolts joint: (a) undamaged joint (24 in-lbs torque), (b) all bolts in the joints were subjected to 8 in-lbs torque, and (c) all bolts were in loose condition (finger tight).

Experimental results for all three cases are presented in Figure 77 and Figure 78. Figure 77 shows raw impedance data collected for three experimental scenarios. As it could be seen from the figure, impedance amplitude are different for each structural condition, but no correlation of impedance amplitude and stress level in the joint was observed. Shifting of maximum and minim frequencies in impedance signatures is not apparent and the data was normalized to obtain clear representation of resonance features. The normalized data is presented in Figure 77b for impedance and Figure 78a for admittance. Further zooming in the admittance maximum yields Figure 78b, which shows details of the resonance behavior for three experimental conditions. Rather noticeable change of resonance frequency was observed for the undamaged case (all bolts at 24 in-lbs). However, very little, if any, difference exist between all bolts loose and all bolts at 8 in-lbs cases. This observation implies that the thickness resonance mode of the EMI method may be sensitive to extreme conditions only. It should be noted that EMI thickness resonance measurement has shown rather low sensitivity to damage and, although distinguishing extreme cases, may not be recommended as a stand-alone technique but only in combination with more sensitive SHM methods.

4.5 Acousto-Elastic Measurement for New Mexico Tech Payload on Sub-orbital Space Flight

On May 20, 2011 New Mexico Tech was given an opportunity to launch a scientific payload on a sub-orbital spaceflight. Piezoelectric sensors were monitored during the flight and acousto-elastic response of the joint was measured using a wave propagation technique in pre-launch and post launch conditions in the laboratory setting.

The suborbital flight utilized Space Loft XL Vehicle provided by UP Aerospace (http://www.upaerospace.com). The flight was a commercial flight, which also carried educational activities sponsored by NMSGC (http://www.nmspacegrant.com).
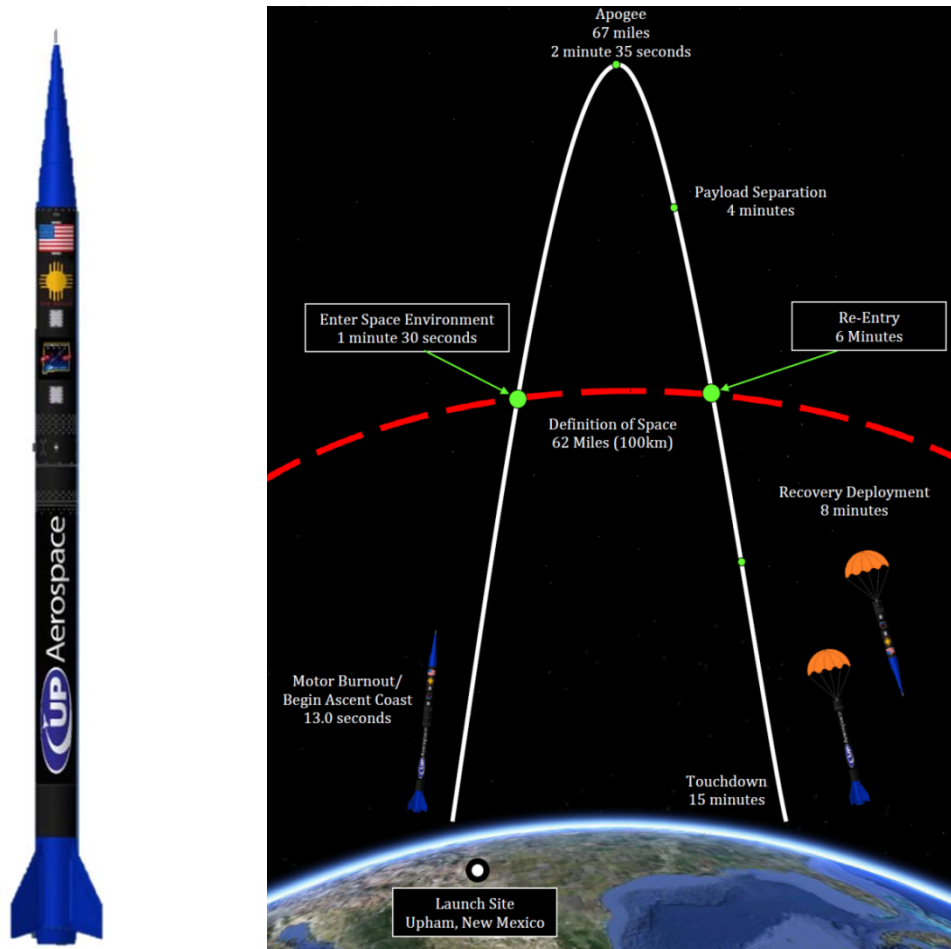
Figure 79 SpaceLoft vehicle and its suborbital trajectory.

A SpaceLoft vehicle and its typical trajectory are presented in Figure 79. Total duration of the flight is close to 13 minutes, which gives a payload several minutes in space environment. An overview of New Mexico Tech payload is presented in Figure 80. Detailed description of the payload assembly and electronic packaging is available in [53].
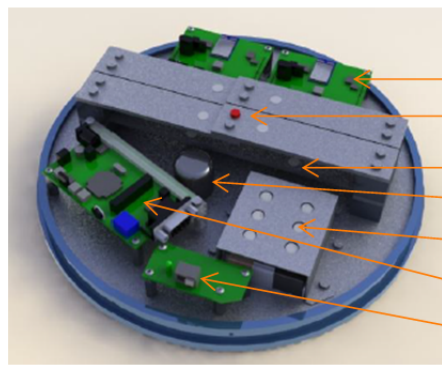
Figure 80 Schematics of New Mexico Tech payload.

For the purpose of this investigation, only information on a bolted joint is important. The bolted joint test fixture consisted of four aluminum beams. Two 4 3/8" by 1" beams were bolted with #8 bolts to create a lap bolted joint. In addition, two narrower dog-bone-like beams were placed under bolted joint beams. These beams were utilized in the sensor adhesive experiments. Figure 81 provides an illustration of the beams in the payload. Noticeable in Figure 80, both types of bolts were mounted on a payload with long bolts that went though beams and 1 inch aluminum separation blocks. Such a setting supposed to provide a fixed-fixed boundary condition for all beams. However, during electrical testing of a payload, a short was found propagating through blocks and they were insulated with rubber lining. Long bolts at boundaries were tightened to more than 20 in-lb, which was considered to be a "tight" condition for bolts of such a type.

Figure 81 Lap bolted joint beams and beams carrying an adhesive test.

Piezoelectric sensors (APC 851, 7 mm diameter with feedback electrode) were mounted using Hysol epoxy in close proximity of the bolted joint. Figure 82 shows a photo of the payload and respected labels for sensors and bolts. Beam 1 is considered to be a beam with an "intact" joint in which both bolts in the center of the beam were tight to 20 in-lbs. In the Beam 2 with "damaged" bolted joint, an outside bolt was set to 20 in-lbs and the inside bolt (in red color, labeled with "Loose bolt") was set to 5 in-lbs. This setting was selected because 5 in-lbs would provide reasonably tight, not actually loose, bolted joint, but with noticeable torque reduction in comparison with other bolts. A real "loose" or "finger-tight" bolt conditions were not acceptable to prevent disintegration of the joint during suborbital flight.
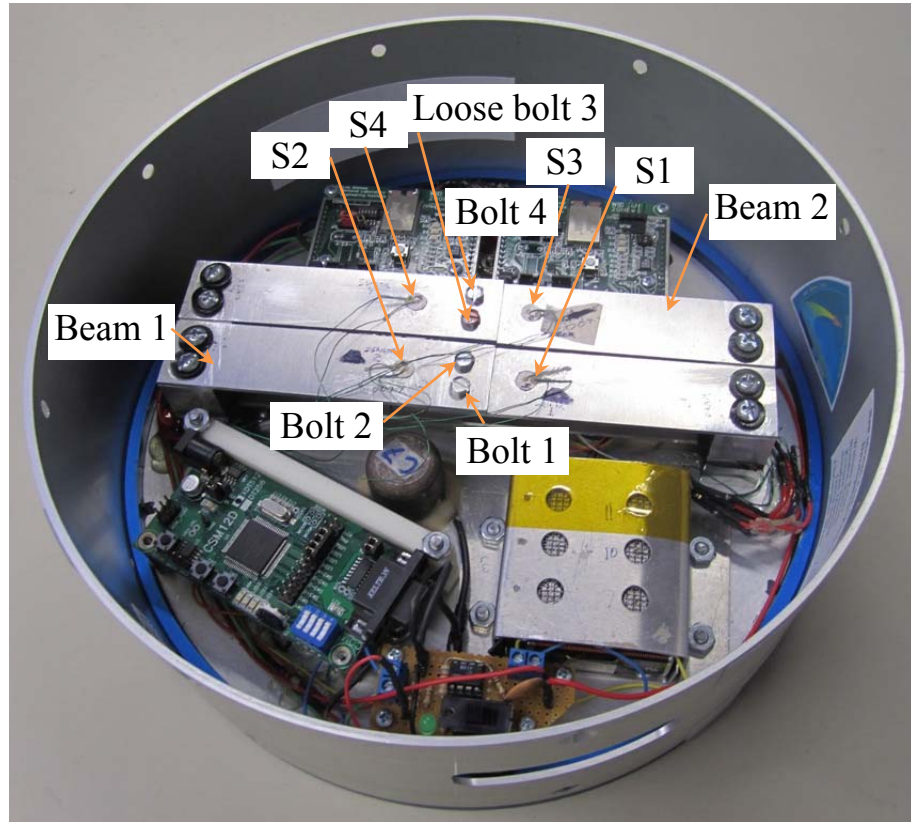
Figure 82 Photo of New Mexico Tech payload.

An acousto-elastic experiment on the payload was conducted in two sequences: after payload final assembly before delivery to vehicle integration facility – labeled as *Pre-launch* test and after receiving the landed payload, the latest among any other test performed in *Post-launch* condition. Similar equipment, Ritec system, with identical testing was utilized in both sequences.

A three count 300 kHz pulses were supplied to designated piezoelectric transducers: transmitters – S2 and S4, receivers S1 and S3. The transmitted pulses were very stable and practically identical in pre and post flight tests, as illustrated in Figure 83.
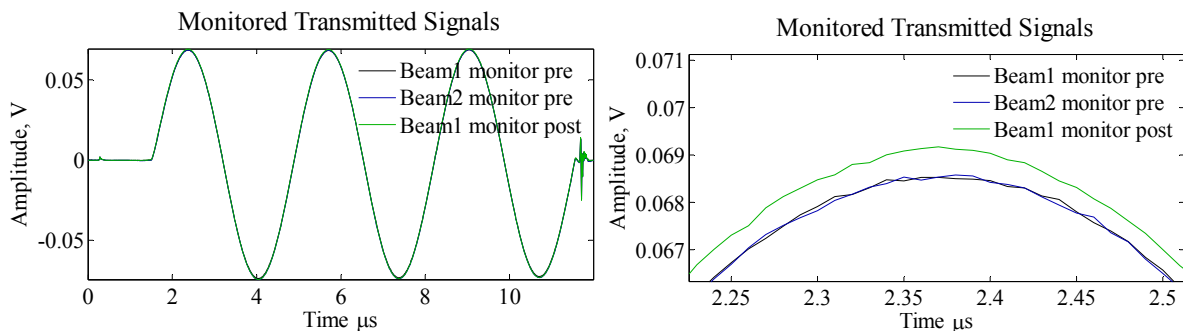
Figure 83 Transmitted signals in pre and post flight acousto-elastic experiments.

During the post-flight test, a hairline crack was noticed on sensor S4 as can be seen in Figure 84. At the time of post-flight tests it was unclear whether this crack was a surface scratch on PZT electrode or it actually fractured the PZT material.

Details of experimental procedures for all tests are given below:

Figure 84 Hairline crack in sensor S4.

Beam 1 (intact joint)

Pre-launch test: All bolts were tightened to 20 in-lbs.

Post-launch test: All bolts were tightened to 20 in-lbs.

No modification to joints or torque on bolts were made for Beam 1 in both pre and post launch tests, so the joint was tested in "as received" condition.

Beam 2 (joint with one loose "red" bolt)

Pre-launch test: All bolts (bolt 3 and bolt 4) were tightened to 20 in-lbs and acousto-elastic data were taken. Results of this test are labeled as *t pre*. Then the outer bolt 4 was to 0 in-lbs and data were taken, labeled as *loose pre*. The bolt was then tightened (loosened and tightened) to subsequently 10 in-lbs, 15 in-lbs, and 20 in-lbs and data were taken at each torque. On the figures below, these data are labeled as *t10 pre*, *t15 pre*, and *t20 pre*. The last one signifies "tight" condition. Bolt 3 stayed at 20 in-lbs during all of these tests.

Post-launch test: The acousto-elastic data were taken in "as received" condition, labeled as *t post*. Bolt 4 was loosened to 0 in-lb to imitate "loose condition". The data were taken and Bolt 4 was tightened (upon loosing each time) to 10 in-lbs, 15 in-lbs, and 20 in-lbs. The data for each condition in this sequence was taken and was labeled as *t10 pre*, *t15 pre*, and *t20 pre*.

Before analyzing the suborbital launch pre and post flight data, it is important to understand modifications in the acousto-elastic response caused by a loose bolt surrounded by tightened bolts. As indicated in our prior work on the subject [52], loosening of a bolt causes a phase shift of the elastic wave indicative of lower wave speed. The shift is proportional to torque supplied to bolts. Results of the acousto-elastic tests are presented in the following figures.

Figure 85 shows results for intact Beam 1. Although no changes were anticipated for this beam, the acousto-elastic response indicates first right shift, then phase stabilization, left shift and then again a profound left shift. Also noticeable in the figure, amplitude of the post-flight wave is lower than in the pre-flight case. Initial left shift of the post-flight record indicates that bolts in the "intact" joint may show lower torque than in the pre-flight condition. Clearly, even for the intact beam, there is significant deviation of the acousto-elastic response.
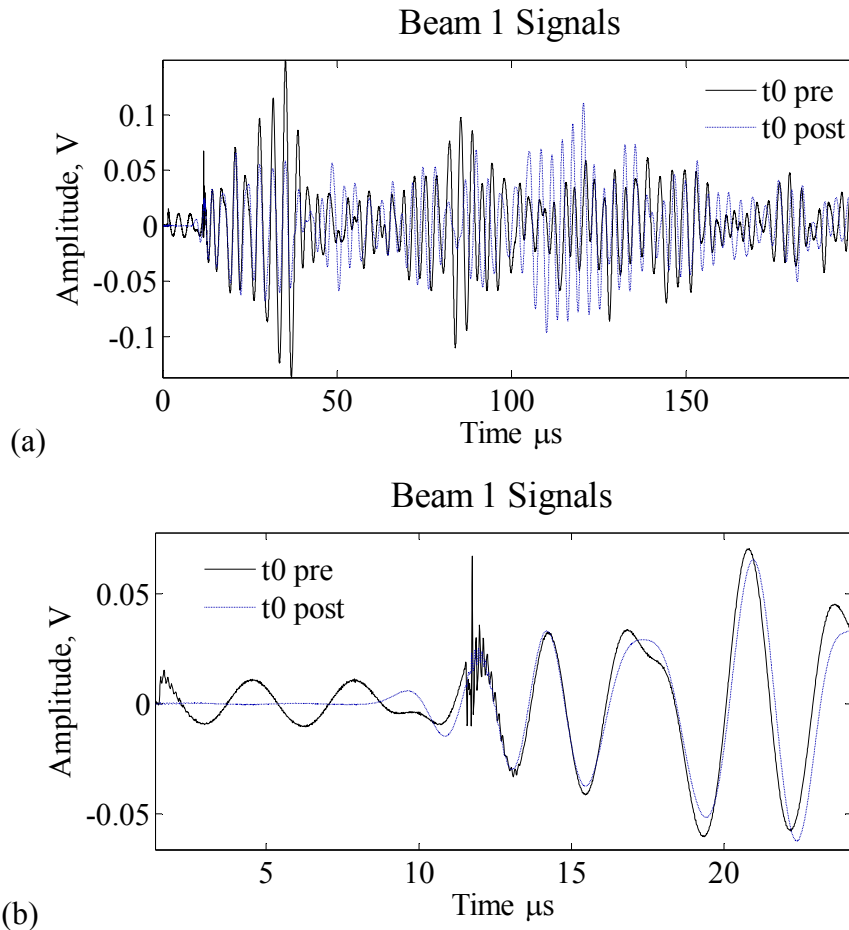
Figure 85 (a) Elastic waveforms obtained for pre and post flight conditions of intact Beam 1. (b) zoom-in into the beginning portion of the signal.

The pre-launch data shown in Figure 86 indicate several interesting facts. Largest right shift is observed for the case of "loose" bolt. Further re-tightening does not fit exactly with previous "tight" data, but it shows a clear trend into more shift towards right for the lower torque conditions. Apparently, there could be changes in the joint for initial tight and re-tightened conditions. The post flight signal depicted in Figure 87 with pre flight signals shows distinct difference, but it behavior resembles more "loose" condition rather than intact case. However, a perfect match was not anticipated because in pre-launch tests, Bolt 3 was tightened to 20 in-lbs while in post flight condition it supposedly was at 5 in-lbs.

Beam 2 Pre Launch Signals

(a)

Beam 2 Pre Launch Signals

(b)
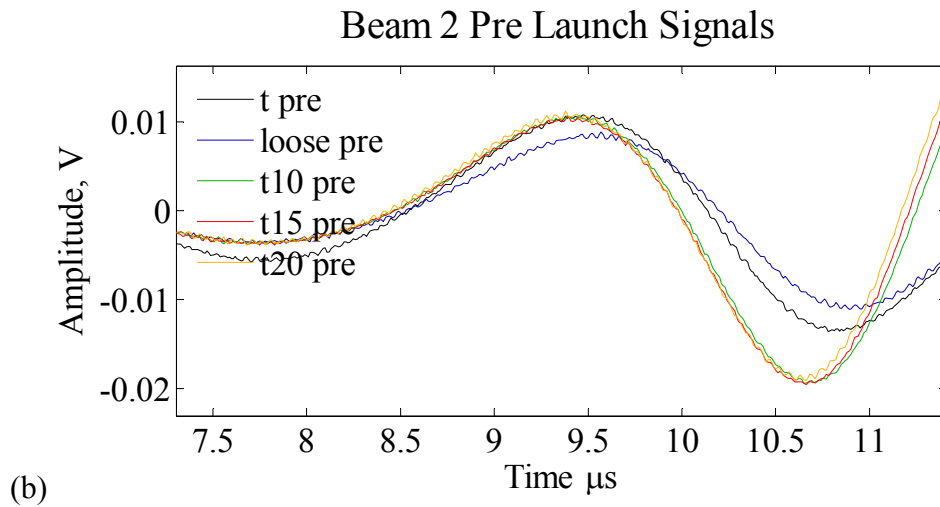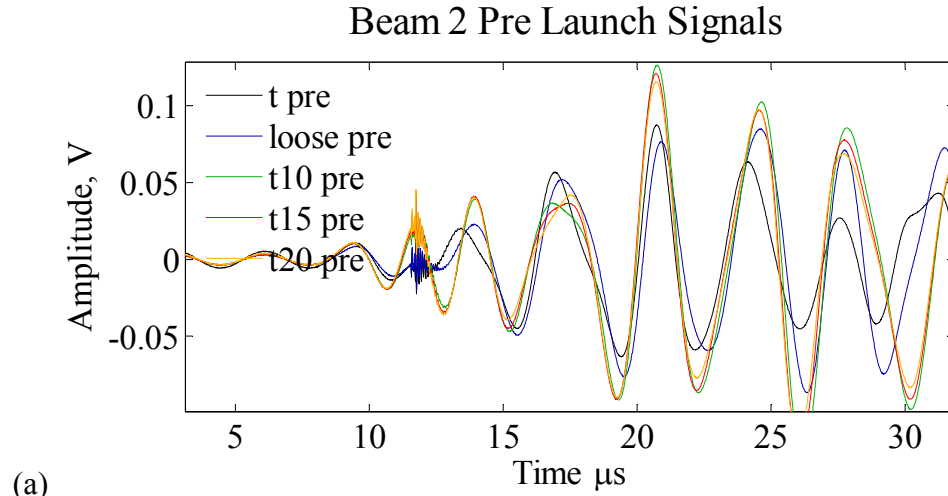
Figure 86 Elastic waveforms obtained for pre flight conditions of Beam 2. (a) zoom-in into the beginning portion of the signal, (b) more detailed zoom into beginning portion of the signal.

Beam 2 Pre Launch and Initial Post Signals
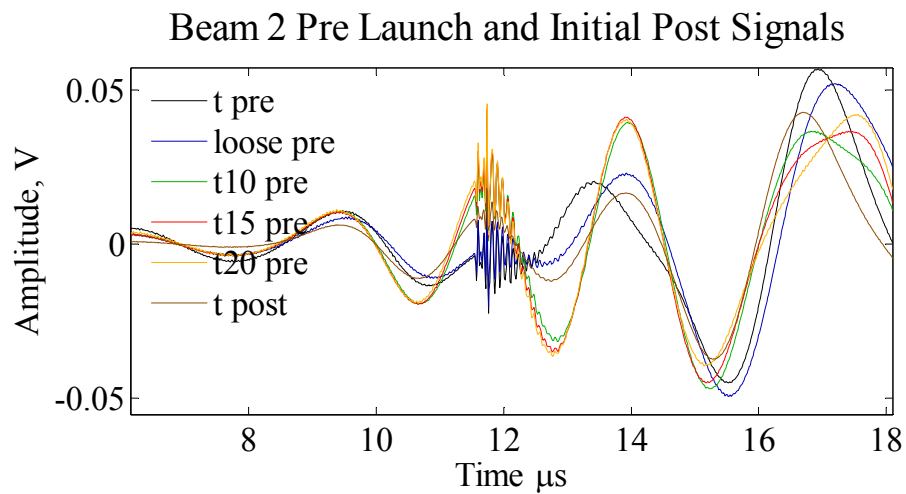
Figure 87 Elastic waveforms obtained for pre flight and one post flight conditions of Beam 2.
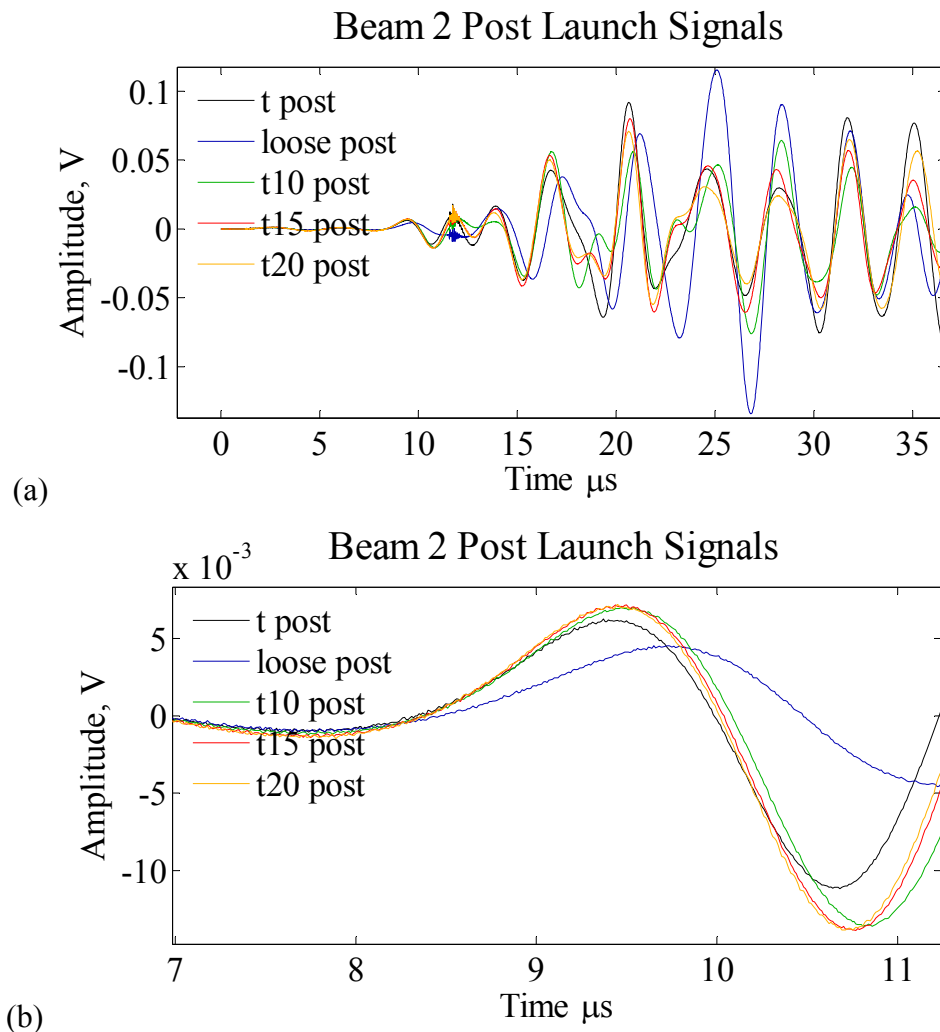
Figure 88 Elastic waveforms obtained for post flight conditions of Beam 2. (a) zoom-in into the beginning portion of the signal, (b) more detailed zoom into beginning portion of the signal.

Figure 88 illustrates elastic signals in the post flight condition. The post flight signal is close to "tight" condition of the bolt, as was anticipated because before launch, Bolt 4 was tightened to 20 in-lbs. Loosening of Bolt 4 (Bolt 3 stays at original torque of 5 in-lbs) substantially modifies the signal as waveform noticeably shifts towards right. Subsequent tightening to specified torques, produces a left shift of the waveform as anticipated from previous tests. Analysis indicates that the spaceflight clearly changes state of torque in a bolted joint. To quantify the change, a real-time acousto-elastic system for monitoring bolted joint condition during flight is needed. Some quantification is currently underway via analysis of typical data deviation and its application to suborbital flight cases.

4.6 Material/structural Characterization for Model Updating

Modern space applications often require high fidelity structural dynamic models for efficient and reliable operation. Consequently, accurate models need information on structural parameters such as stiffness, mass, and damping coefficients that depend on fundamental material properties. Traditional models updating procedures utilize the experimentally-measured structural dynamic response to correct analytical or numerical model of the structural element. Over past decades, this subject attracted substantial attention and a broad spectrum of model-updating methodologies has been developed focusing on mechanical, civil, aerospace and other applications [54]. Although it is not possible to mention all methods for model updating, the general approach consist of adjusting material constants in the model by iteratively minimizing the discrepancy between theoretically calculated and experimentally measured structural dynamic responses. Since it is anticipated that experimental vibration data for any particular satellite may not be available for pre-launch and on-orbit conditions, the satellite model updating procedure departs from a traditional approach and needs to consider independent means of determining structural material parameters, which may be achieved by utilizing the SHM system as illustrate in Figure 89. The basic idea is to update low frequency finite element vibration model using material characterization data obtained in high frequency (ultrasonic) measurements.
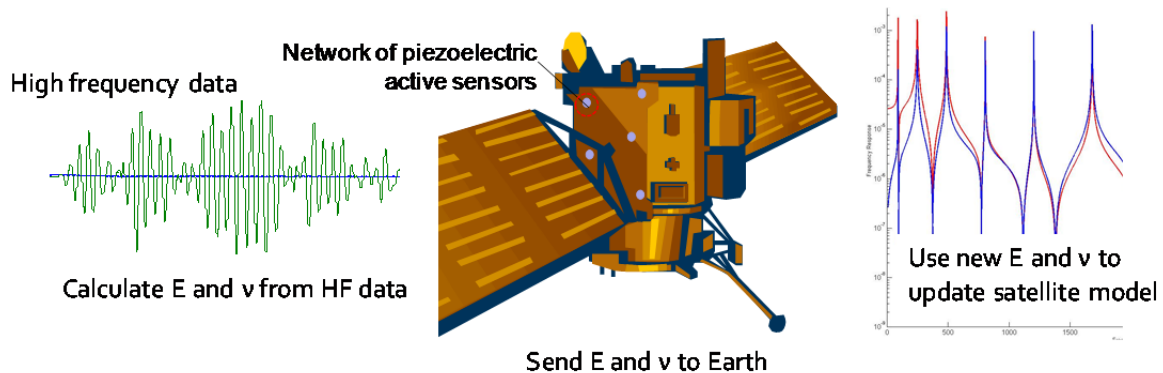
Figure 89 Concept of the low frequency model updating using data from high frequency tests.
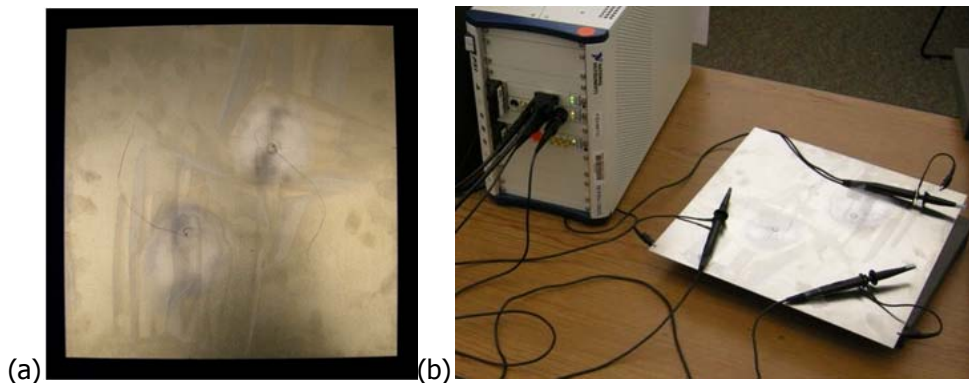
Figure 90 (a) Aluminum 2024 (1ftx1ft) plate specimen instrumented with PWAS, (b) experimental setup for sound speed measurements.
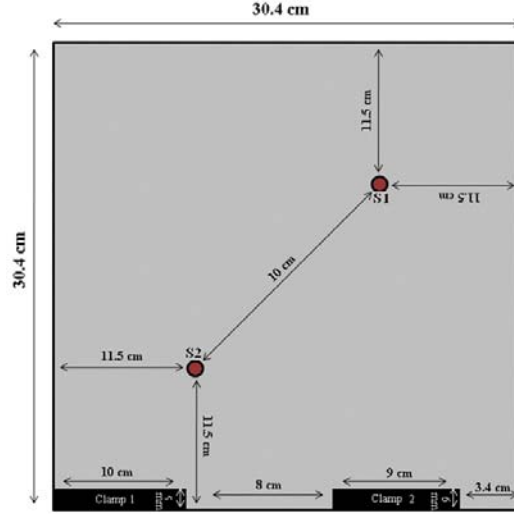
Figure 91 Schematics of Al 2024, 1.6 mm thick plate with surface-bonded piezoelectric sensors.

The proposed method for determining structural material parameters such as Young's modulus (E), the shear modulus (G) and the Poisson ratio is based on the guided wave propagation enabled by embedded ultrasonic sensors. In contrast to classical ultrasonic evaluation that needs two independent measurements to determine these material parameters, the guided (Lamb) wave propagation requires only one standardized configuration such as a typical sensor network layout. Advantageously, this allows the SHM system to perform two tasks: damage detection and material characterization. The general idea of characterizing structural material using the guided waves is to experimentally determine the dispersion curves for symmetric and anti-symmetric modes and to obtain the best fit with theoretical values by adjusting the shear wave velocity, C_S, and the Poisson ratio, v [55]. With C_S and v known, the Young's and shear modules can be determined and used for the model updating.

$$G = C_S^2 \cdot \rho \,, E = 2G \cdot (1+v) \tag{15}$$
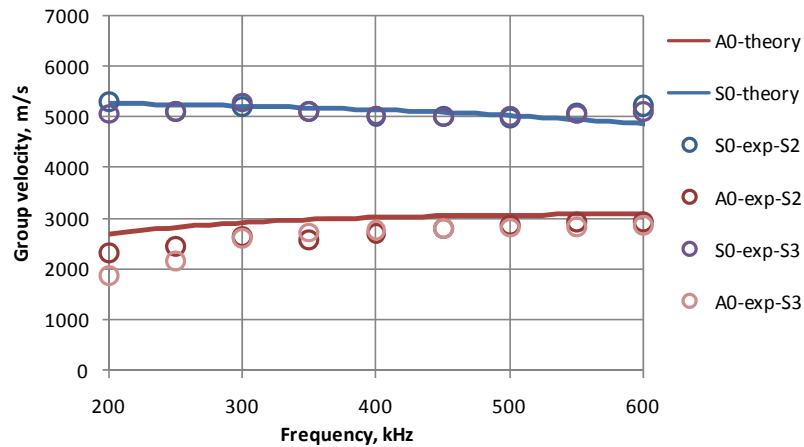
Figure 92 Dispersion curves for Al 2024, 1.6 mm thick plate.

Approved for Public Release; Distribution Unlimited.

As a first step in realizing this approach, we conducted a set of experiments on a 1ft × 1 ft × 0.063 in aluminum 2024 panel instrumented with surface-bonded piezoelectric sensors as illustrated in Figure 90. As it can be seen in the Figure 91, a separation distance between sensors was rather short and equaled 10 cm. Sensor S1 was used as a transmitter of 5 count elastic wave pulses. The pulses were received by sensors S2 and S3; the latter one being positioned on the other side of a plate directly underneath S2. Illustration of experimental group velocity dispersion curves within 0.2-0.6 MHz frequency range is presented in Figure 92. Theoretical curves calculated for aluminum 2024 nominal values of E=72 GPa, v=0.33, and ρ=2770 kg/m^3 are also presented in the figure. Good match of experimental and theoretical data has been achieved, which may be further improved through automation and refinement of the fitting procedure.

Boundary conditions have a profound effect on structural dynamics. Hence, it is important to monitor changes in structural boundary conditions, which may occur during storage and assembly of satellite's components, transport to the launch facility, and on-orbit operation. Three sets of tests were conducted to investigate the capability of the embedded piezoelectric system to monitor the state of the structural boundary conditions. In each set, the aluminum plate depicted in Figure 91 was measured in free-free condition, clamped (with vices) near sensors S2 (clamp 1), clamped near sensor S1 (clamp 2), and clamped with both clamp 1 and clamp 2. The sets differed in methodologies used to monitor boundary conditions:

1) Pitch-catch method utilizing two sensors (one as a transmitter and one as a receiver),
2) Pulse-echo method realized with one sensor,
3) Electro-mechanical impedance method with one sensor.

Ultrasonic signals obtained for four boundary conditions of the plate are presented in Figure 93 and Figure 94. The first pulse in the record is a directly transmitted S0 pulse, which is followed by the A0 pulse overlapping with S0 reflection. The end of this reflection and waveforms occurring after 80 μs (in Figure 93) are anticipated to reflect changes in boundary conditions. Figure 93 shows no effect of boundary conditions on the initial portion of the record (no reflections from boundary yet) and noticeable changes when the pulse reflects off boundary with clamps. These changes, however, are more significant at higher frequencies, as suggested in Figure 94. It is interesting to note that application of clamp 1 and both clamps gives the largest deviation from the free-free boundary condition. It seems that clamp 1 plays a key role in this process as it is closest to the receiving sensor S2.

One inconvenience of utilizing the pitch-catch method for assessing boundary conditions is the need to analyze the signal record based on geometry of the sample and to identify the affected pulses. The pulse-echo technique was considered to mitigate this problem as it allows one to configure the system for boundary assessment based on the first or second pulse in the record. Figure 95 presents a pulse-echo 200 kHz signal recorded for four states of the plate's boundary. Changes of both amplitude and phase for clamp 1 and both clamps are in opposite direction to clamp 2. Clamp 2 induces a larger change in amplitude, but clamp 1 and both clamps cause larger phase shifts. A pulse-echo signal at 500 kHz shows a slightly different dependence with clamp 2 causing some changes that increased when clamp 1 and both clamps were used.
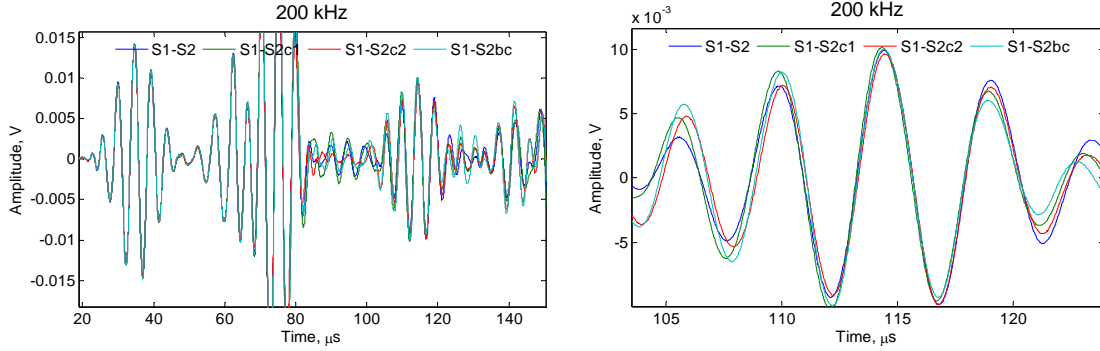
Figure 93 Pitch-catch 200 kHz ultrasonic signals obtained for four boundary conditions of the plate: free-free (S1-S2), clamp 1 (S1-S2c1), clamp 2 (S1-S2c2), both clamps (S1-S2bc).
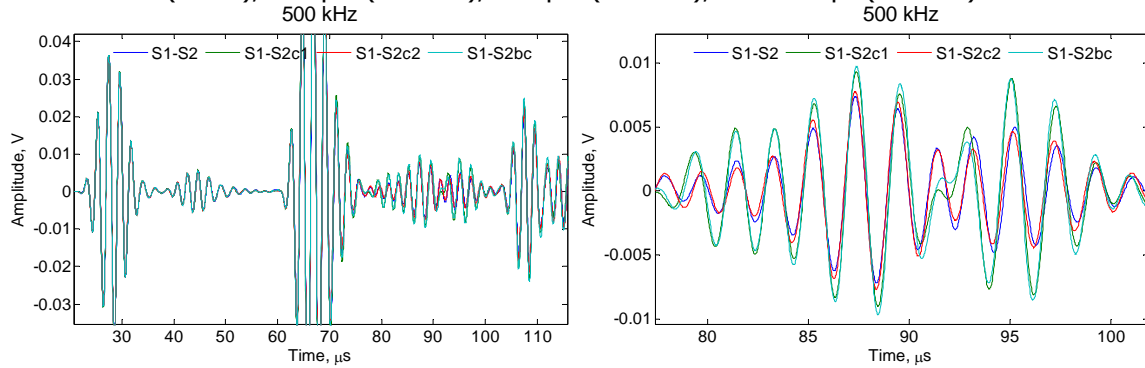
Figure 94 Pitch-catch 500 kHz ultrasonic signals obtained for four boundary conditions of the plate: free-free (S1-S2), clamp 1 (S1-S2c1), clamp 2 (S1-S2c2), both clamps (S1-S2bc).
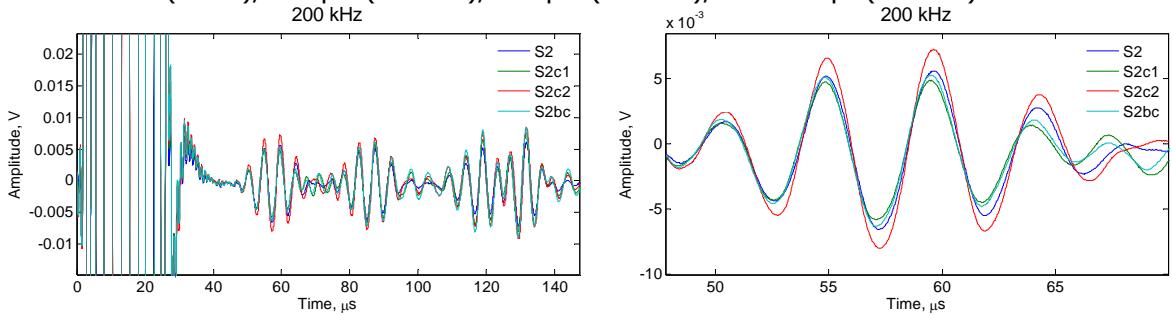
Figure 95 Pulse-echo 200 kHz ultrasonic signals obtained for four boundary conditions of the plate: free-free (S1-S2), clamp 1 (S1-S2c1), clamp 2 (S1-S2c2), both clamps (S1-S2bc).
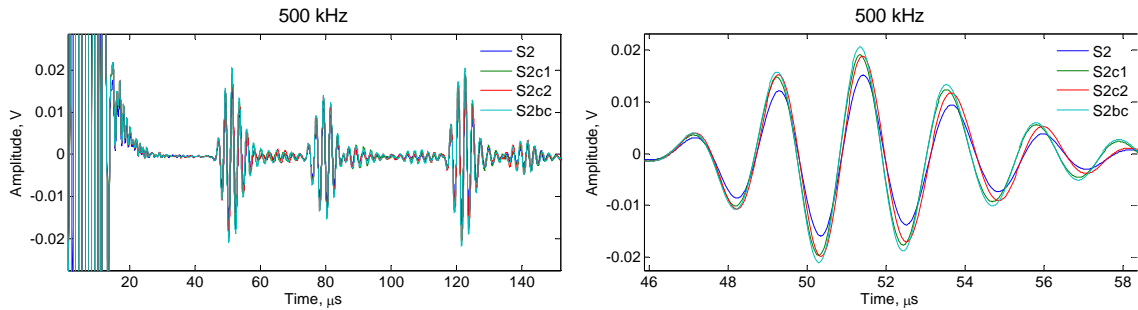
Figure 96 Pulse-echo 500 kHz ultrasonic signals obtained for four boundary conditions of the plate: free-free (S1-S2), clamp 1 (S1-S2c1), clamp 2 (S1-S2c2), both clamps (S1-S2bc).
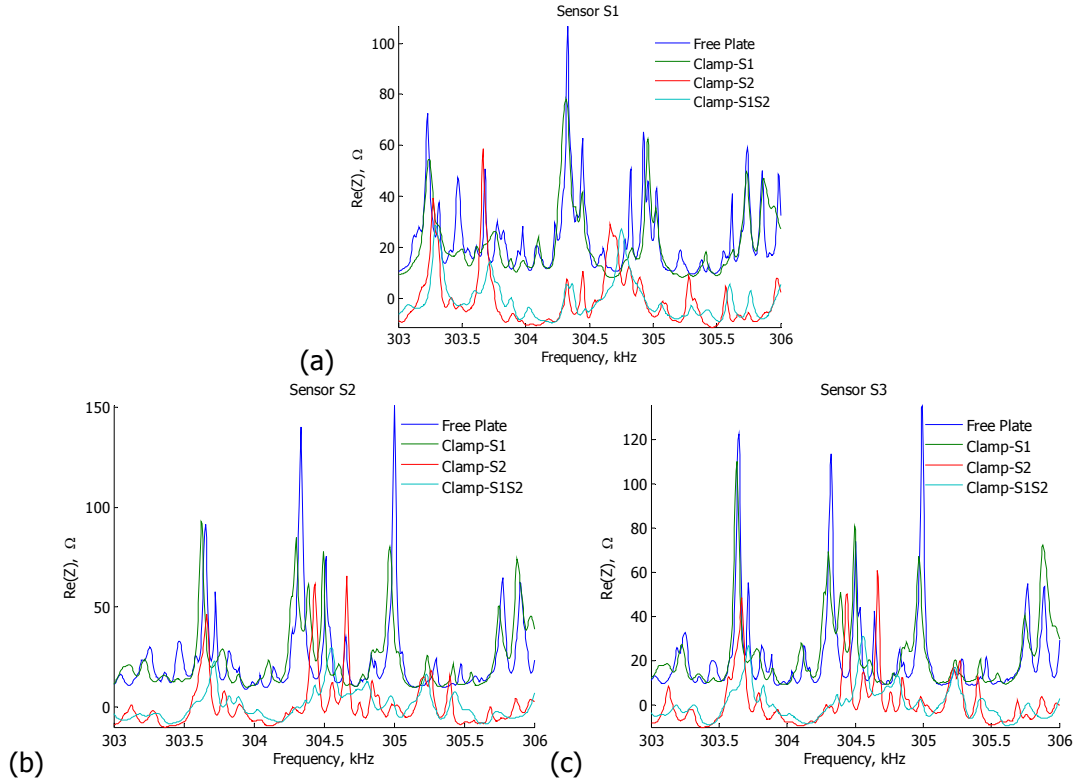
Figure 97 Impedance signatures of sensors S1 (a), S2 (b), S3 (c) corresponding to four boundary conditions of the plate: free-free, clamp 1 (S2), clamp 2 (S1), both clamps (S1S2).

In addition to embedded ultrasonic techniques utilizing a pulse signal, the electro-mechanical impedance method and CW structural excitation were explored for assessment of structural boundary conditions. The electro-mechanical impedance method allows for direct extraction of the structural dynamic response at ultrasonic frequencies. In effect, the impedance signature of the piezoelectric sensor bonded to structural surface reflects structural dynamic features. Figure 97 shows position and magnitude of impedance peaks for four different boundary conditions of the plate. The impedance signature of sensor S1 located rather far away from the clamps is presented in Figure 97a. Clamp 2 (at S1) introduced mostly right-hand frequency shifts indicating stiffening of the plate. This trend is continued with application of clamp 1 and both clamps. However, for sensors S2 and S3 located closer to clamps than S1, right-hand frequency shifts were observed for boundary conditions exerted by clamp 1 and both clamps, but a decreased frequency shift was noticed when clamp 2 was applied. Interestingly, such an opposite shift for similar boundary conditions was observed in Figure 95 for the pulse-echo data. Impedance data presented in Figure 97 suggests that the electro-mechanical impedance method can be used to discern changes in boundary conditions of a structural element. In principle, material properties may be inferred from impedance tests on a structure with known boundary conditions and rather simple geometry as correlation is sough between the analytical or numerical model and experimental impedance data. However, such correlation is typically considered at rather low frequencies at which sensor sensitivity to boundary condition is not pronounced. Because the major concern of spacecraft structures is integrity of interfaces, studies at low

frequencies were not conducted and priority was given to studies at rather high (100s of kHz) frequencies considered to be more sensitive to changes in boundary constraints and, hence, interface conditions.

4.7 Piezoelectric Sensors for SHM of Space Structures

4.7.1 Sensor Protection and Shielding

One of the issues raised after acquiring SHM data during suborbital flight is sensor survivability and shielding. On the first issue, it is know that even unprotected piezo-ceramic wafer sensors (PWAS) may survive and perform adequately for rather long time under typical environmental conditions [56]. Integrity of adhesive interface, continuity of wires and thermal cycling are primary concerns when sensor survivability is considered. Much less attention is given to PWAS shielding. In fact, no studies on PWAS shielding are available to our knowledge. Because shielding is a concern in spacecraft operation, it was decided to briefly investigate aspects of shielding applied to PWAS and suggest potential shielding design.

Absence of PWAS shielding affects (a) electromagnetic interference (EMI) and (b) level of signal noise. Example of EMI in pitch-catch and pulse-echo SHM setups can be found throughout this report. To address both issues, PWAS shielding designs are suggested.

(a) (b)
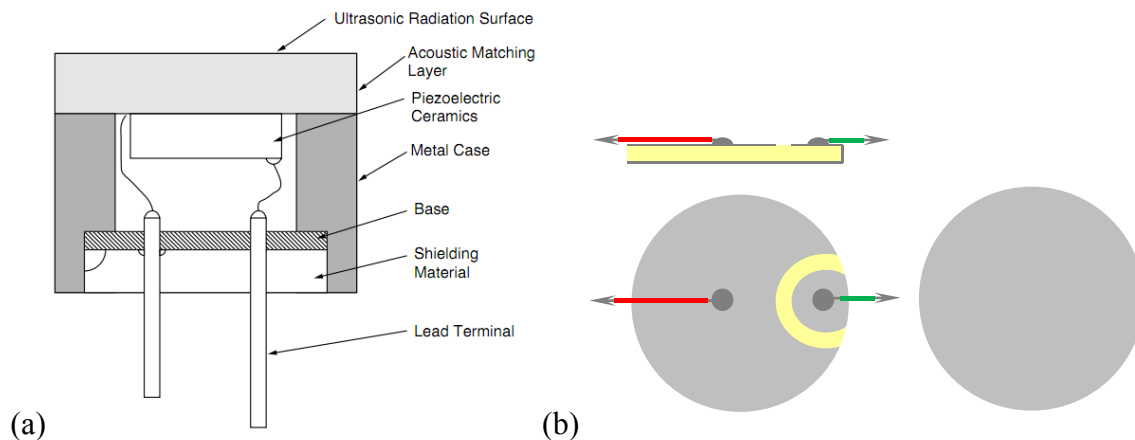
Figure 98 Typical design of (a) high frequency ultrasonic sensor (www.murata.com), (b) PWAS.

Typical design of high frequency ultrasonic transducer is shown in Figure 98a. In the figure, it is noticeable that piezoelectric element is enclosed into a metal case for shielding. However, PWAS configuration is not well suited for applying a shielding case. This is primarily because bottom ground electrode can not extend into sensor thickness except limited "flip over" area as illustrated in in Figure 98b. Two potential shielding designs are presented in Figure 99.

(a) (b)
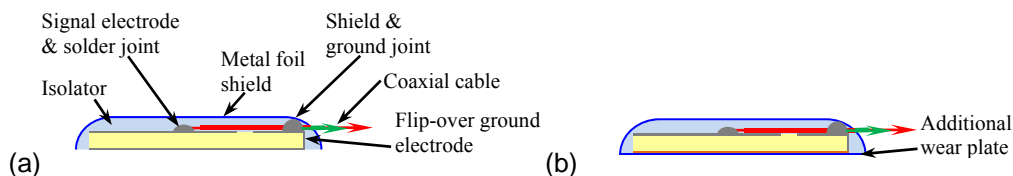
Figure 99 Shielding designs for PWAS (a) with metallic foil around the sensor (b) with additional to (a) metallic wear plate.

Approved for Public Release; Distribution Unlimited.

Main concern in presented designs is isolation of signal electrode from the ground and connection of the ground electrode to the shield. More robust and "integrative" design would involve wear plates as a part of the shield, but this option would affect the efficiency of elastic wave generation as there will be two adhesive layers and a metal foil between the sensor ground electrode and host structure. In addition to actual shield, PWAS design should involve proper cable and connector. Our primary selection is 0.81mm OD coaxial cable and a micro-dot connector.

There is an alternative to the design presented above. Integration of installation and shielding processes is suggested. Instead of using a metal foil shield, the sensor is installed using standard methodology, a layer of isolating epoxy is applied atop and around the sensor, a small portion of isolating epoxy covering ground solder joint is carefully removed to expose ground connector and metallic epoxy is applied over isolating epoxy to form electromagnetic shield. Figure 100 illustrates this approach.
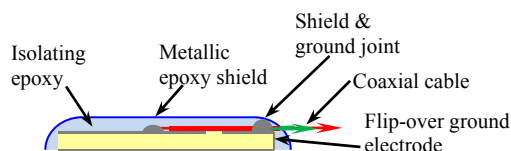
Figure 100 Shielding using integrative approach in which a metallic epoxy is applied over isolating epoxy.

From sensor fabrication and installation point of view, the third approach is preferable, although shielding efficiency of metallic epoxy may be questionable.

4.7.2 Consideration of Sensor Statistics and its Use in SHM

Structural Health Monitoring can be a useful tool for inferring information about structural integrity. However, a large number of factors can influence an SHM systems ability to accurately determine the integrity of the structure. Traditionally the evaluation of an SHM system involves considering a specific technology with a fixed sensor type and damage detection methodology. These evaluations then study the influence of contributing factors within the scope of the specific SHM system. The statistical information collected for these situations reflect a cumulative contribution of all SHM factors, such as sensors, electronics, bonds, structure, environment, etc. The SHM system will need to be reevaluated if any factor is changed.

It is proposed that it would be beneficial to depart from this philosophy and consider the contributions of individual SHM components on the cumulative statistics used in evaluating the systems performance. Research efforts presented below were aimed at investigating variability in SHM sensors and possible contribution to the cumulative statistics.

4.7.3 PWAS Impedance Statistics

Piezoelectric sensors are well understood and are often characterized by their electro-mechanical (E/M) impedance which is defined as the frequency dependent ratio of voltage to current. Therefore, in order to calculate the effects of variability in the PWAS on the

performance of the sensor, it is necessary to calculate the effects of sensor variability on measured E/M impedance.

In order to decouple the effect of bond layer and medium on the PWAS statistics, impedance measurements were performed on PWAS in a free-free boundary condition. A sample size of 30 was selected to adequately represent PWAS population. The selected circular PWAS have a 7 mm diameter and 0.25 mm thickness. The batch of PWAS was manufactured from APC851 piezoelectric material with a wraparound electrode, as illustrated in   Figure 101. The wrap around electrode is beneficial for many embedded sensor applications; however, it increases the complexity of electro-mechanical transformation within the sensor and respective analytical and numerical descriptions.

(a)   (b)   (c)

Figure 101 a) Circular PWAS diagram with wrap around electrode.   b) Test samples for free-free test fixture. c) Test samples with soldered leads.

Two sets of impedance and admittance measurements were taken. First, the 30 samples were tested using a fixture to simulate a free-free boundary condition on the PWAS without soldered leads, see Figure 102a. The sensors were oriented similarly for all 30 samples. The second measurement set was taken after leads were soldered to the electrodes. For this measurement, the PWAS were suspended by their leads so the sensors were not in contact with any surface. The wrap around lead was connected to ground for all 30 samples.

Three E/M impedance measurement ranges were chosen to characterize PWAS. The first range chosen was from 200 – 1000 kHz with a resolution of 500 Hz. The second range was from 250 – 400 kHz with a 100 Hz resolution. The third measurement range was 8 – 11 MHz with a 4 kHz resolution. The third measurement range captures the fundamental resonance of the thickness mode, while the other two ranges capture an in-plane resonance. Both sets of measurements were taken using an HP4192A impedance analyzer with an LCR 005 test fixture, see Figure 102b.

(a)   (b)
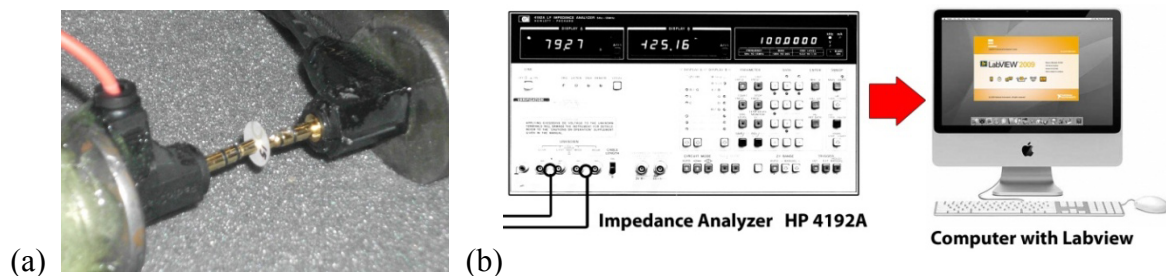
Figure 102 a) Free-free test fixture b) HP4192A with LCR 005 Test Fixture.

After collecting test data for free-free PWAS conditions depicted in Figure 102a, lead were soldered for all participating sensors and impedance data were taken again. Impedance tests

yielded collections of data for all 30 PWAS specimens with the test fixture and with soldered leads. Examples of the data obtained in both tests are depicted in Figure 103.

(a)

(b)

(c)
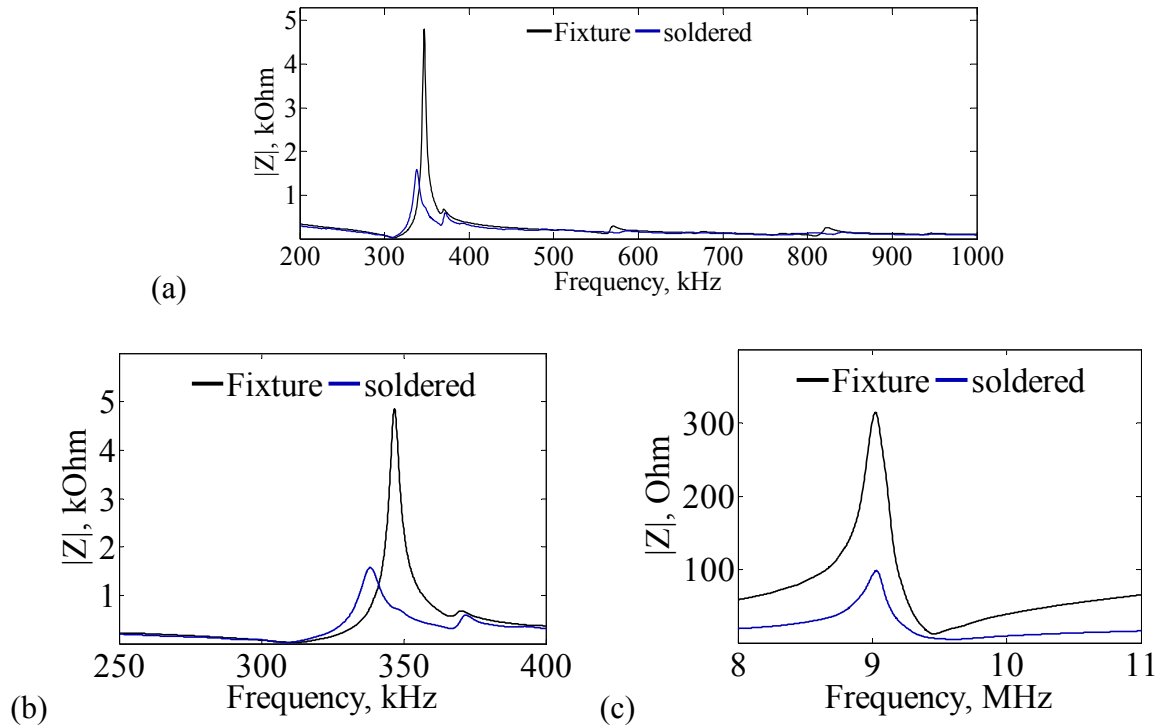
Figure 103 Test data from PWAS #4 comparing the impedance magnitude measurements using the free-free fixture to the measured with soldered leads. a) shows 200 − 1000 kHz range, b) shows 250 − 400 kHz range, and c) shows 8 − 11 MHz range.

(a)

(b)
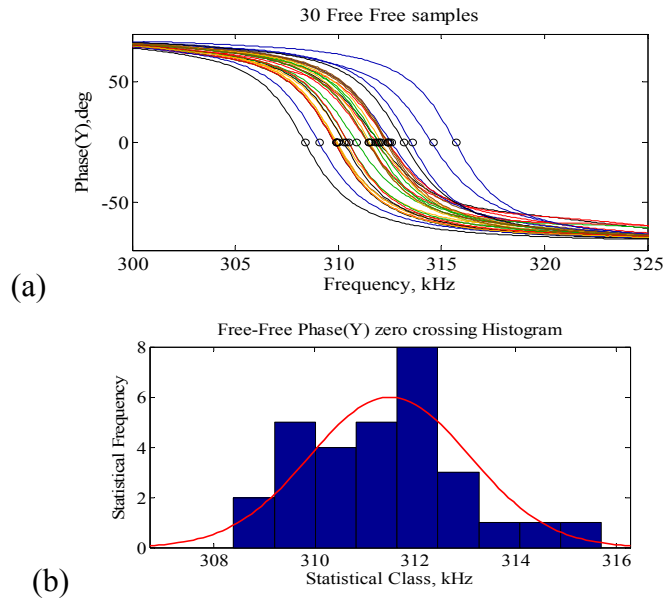
Figure 104 (a) Resonance frequencies of piezoelectric disk actuators/sensors determined as zero crossings of admittance phase, (b) resonance frequency statistics and superimposed normal distribution.

The data was processed to determine the frequencies of the primary resonance and anti-resonance. The in-plane resonance is determined from the peak of the admittance magnitude curve, while the in-plane anti-resonance is determined from the peak of the impedance magnitude curve. For thickness resonances the impedance peak indicates a resonance while an admittance peak indicates an anti-resonance (Giurgiutiu, 2008). Figure 103 shows the three measurement ranges for PWAS sample 4. However, since damping is present in the measurements, the zero-crossing frequency for the admittance phase is taken as a measure of the undamped resonance frequency. Example of the phase data is presented in Figure 104.

Likewise, the zero-crossing frequency for the impedance phase is taken as a measure of the undamped anti-resonance frequency. The zero-crossing frequency was calculated by performing a linear interpolation between points lying above and below the zero crossing. A sample mean was calculated using the sample mean formula:

$$\bar{x} = \frac{\Sigma x}{n} = \frac{x_1 + x_2 + x_3 + \cdots + x_n}{n} \qquad (16)$$

Similarly the formula for calculating a samples variance was used:

$$s = \sqrt{\frac{\Sigma(x - \bar{x})^2}{n - 1}} \qquad (17)$$

Mean Impedance Magnitude (Fixture)

(a)

Mean Impedance Magnitude (Soldered)

(b)
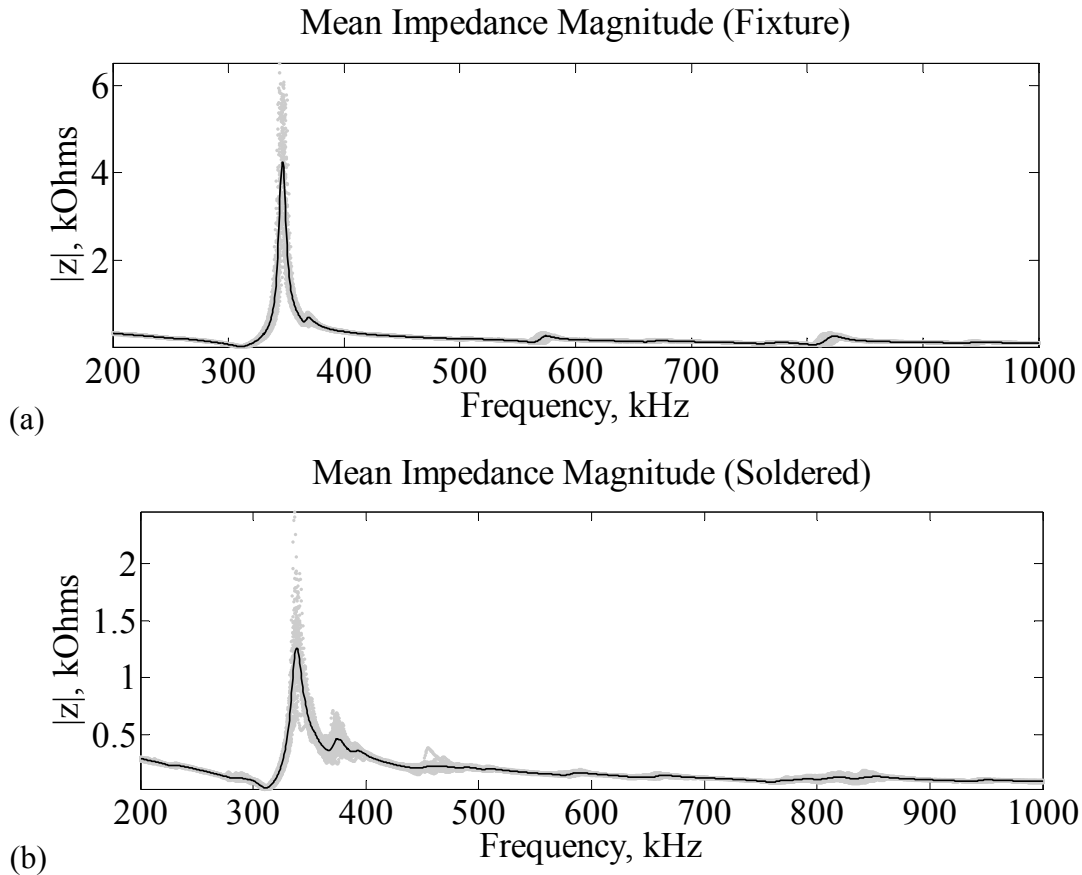
Figure 105 Electro-mechanical impedance response of (a) free PWAS measured in fixture and b) free PWAS with soldered leads. Mean response is indicated as solid line.

Table 7 shows the sample mean and standard deviations for the in-plane resonance and anti-resonance. It should be noted that the standard deviation for the resonance and anti-resonance is higher for the soldered case. It is understandable that the soldering process creates more variability in the impedance and admittance

Table 7 Sample mean and standard deviations for in-plane resonances

Sample Case	Sample Mean (kHz)	Sample Standard Deviation (kHz)
In Plane Resonance (Fixture)	311.4	1.58
In Plane Resonance (Soldered)	312.3	1.65
In Plane Anti-resonance (Fixture)	346.5	1.61
In Plane Anti-resonance (Soldered)	337.8	1.82

response of the sensors as illustrated in Figure 105. It is also important to note that the anti-resonance frequency decreases 8.7 kHz for the soldered case while the resonance frequency increases 0.9 kHz for the soldered case.

A histogram was used to represent the distribution of the resonances. A theoretical Gaussian distribution was calculated using the sample mean and standard deviation. The theoretical distributions were scaled and plotted on top of the histograms as seen in Figure 106. The histograms appear to be in reasonable agreement with the Gaussian distribution for the in-plane resonance and anti-resonance. Plots of sample residuals were generated to assess any bias errors that may be present in the data. No unusual trends were observed and the residuals appear normally distributed.
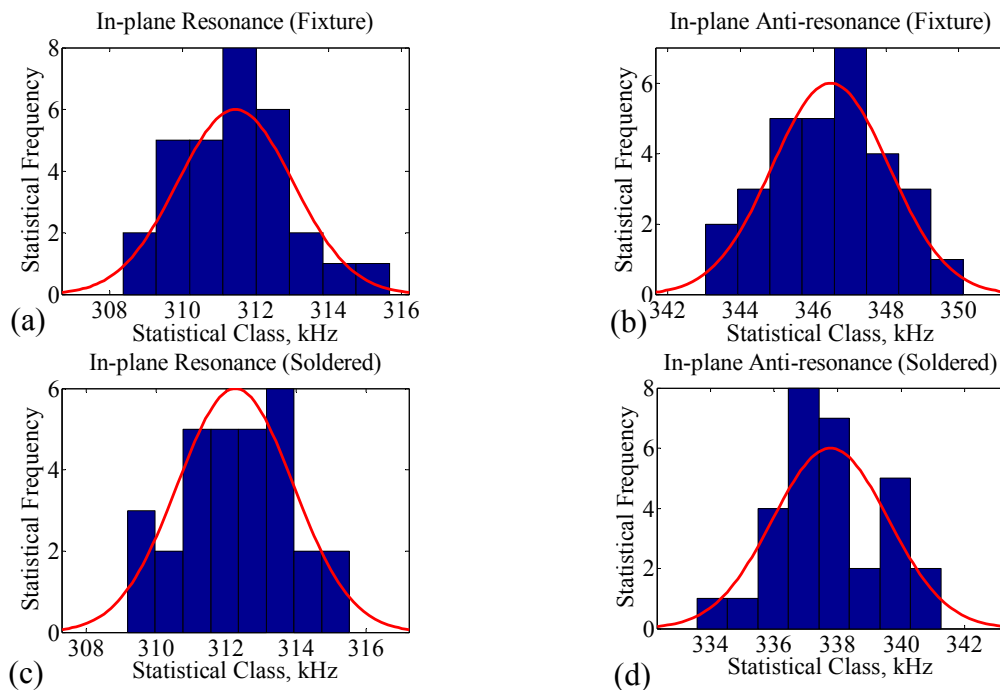
Figure 106 Histograms for in-plane resonance and anti-resonance frequencies.

A similar analysis was performed on the fundamental thickness resonance and anti-resonance mode that was measured using the 8 – 11 MHz measurement range. The sample mean and standard deviation for the thickness anti-resonance was largely unaffected by the soldering process. There was only a slight

Table 8 Sample mean and standard deviations for thickness resonances

Sample Case	Sample Mean (MHz)	Sample Standard Deviation (kHz)
Thickness Resonance (Fixture)	9.56	214
Thickness Resonance (Soldered)	9.68	204
Thickness Anti-resonance (Fixture)	9.22	232
Thickness Anti-resonance (Soldered)	9.12	231

decrease in frequency due to soldering. The resonance mean increased by a small margin. The standard deviation of the resonance actually decreased due to the soldering process. The change in mean and standard deviation may likely be the result of a strain on the PWAS resulting from the use of the free-free test fixture.

Histogram plots were also generated to compare the distribution of thickness resonance and anti-resonance samples. As could be seen in Figure 107, unlike the in-plane resonances, the thickness resonances do not appear to follow a Gaussian distribution.
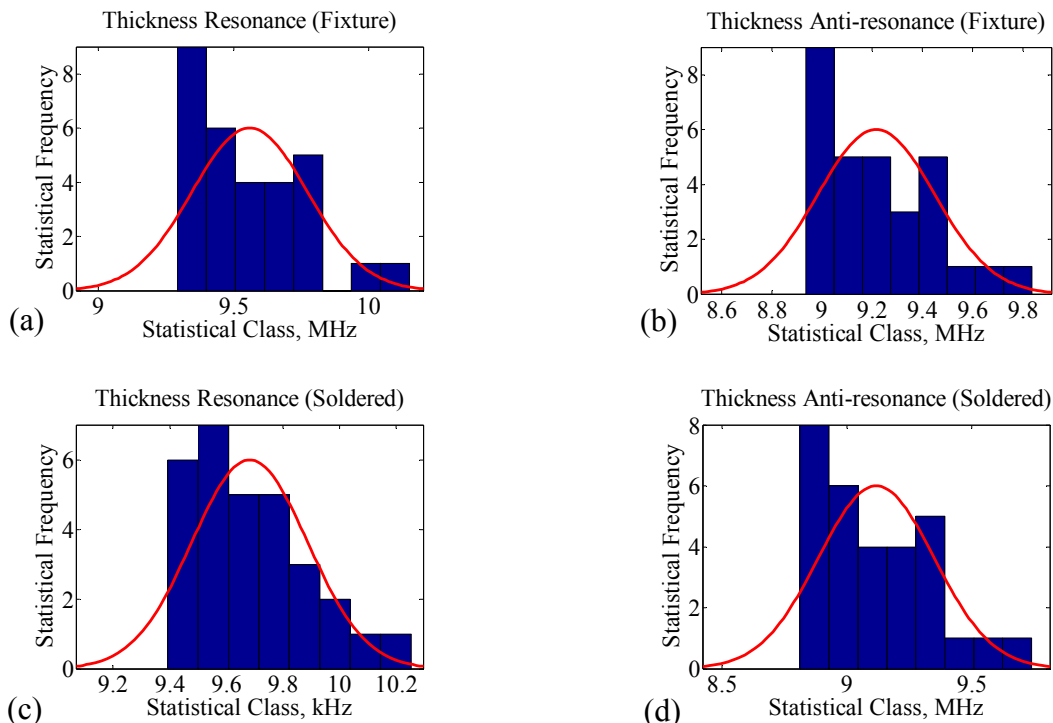
Figure 107 Histograms for thickness resonance and anti-resonance frequencies. The distributions don't appear Gaussian.

In addition to calculating statistical parameters for the resonance and anti-resonance frequencies, statistical parameters were also calculated for the amplitudes of the resonance and anti-resonance peaks. Table 9 and Table 10 show the calculated statistics for the in-plane and thickness resonance and anti-resonance peaks. The amplitude of those peaks clearly decreases except for the thickness anti-resonance which increases. In all cases the standard deviation increases as a percentage of mean for the soldered samples.

Table 9 Sample mean and standard deviations for in-plane resonance amplitudes

Sample Case	Sample Mean	Sample Standard Deviation
In Plane Resonance (Fixture)	61.9 mS	5.5 mS
In Plane Resonance (Soldered)	36.7 mS	5.0 mS
In Plane Anti-resonance (Fixture)	5602 Ω	530 Ω
In Plane Anti-resonance (Soldered)	1403 Ω	339 Ω

Table 10 Sample mean and standard deviations for thickness resonance amplitudes

Sample Case	Sample Mean	Sample Standard Deviation
In Plane Resonance (Fixture)	331.6 Ω	30.0 Ω
In Plane Resonance (Soldered)	94.0 Ω	9.8 Ω
In Plane Anti-resonance (Fixture)	72.4 mS	7.4 mS
In Plane Anti-resonance (Soldered)	198 mS	33.3 mS

4.7.4 PWAS Analytical Model

Presented analytical model is focused on PWAS electro-mechanical impedance as these curves govern frequency-dependent behavior of an active element.

The piezoelectric sensors utilized in this analysis were made from APC 851 piezoelectric ceramic. Sensors features a feedback electrode flipped over thickness of the sensors to facilitate access from one (top) side of the sensor. While sensors with feedback electrode were measured during laboratory tests, our modeling considers a circular sensor with uniform electrodes on the opposite sides of the sensor. An electro-mechanical model of such sensor can be considered for free-free sensor boundary conditions and vertical polarization direction. Solution of the equation of motion for a given set of boundary conditions yields expression.

$$Yd_j := i \cdot \omega_j \cdot C_a \cdot \left[1 - \left(k'_p \right)^2 \right] \cdot \left[1 + \frac{\left(k'_p \right)^2}{1 - \left(k'_p \right)^2} \cdot \frac{(1 + \sigma) \cdot J1(\phi_i)}{\phi_i \cdot J0(\phi_i) - (1 - \sigma) \cdot J1(\phi_i)} \right], \quad Zd_j := \left(Yd_j \right)^{-1} \quad (18)$$

where

$$\upsilon'_E := \sqrt{\frac{1}{\rho_a \cdot s'_{11} \cdot \left(1 - \sigma^2 \right)}}, \qquad \upsilon'_E = (3130.572 + 1.565i) \frac{m}{s} \qquad \phi_i := \frac{r_a}{\upsilon'_E} \cdot \omega_i$$

$$C_a := \varepsilon'_{33} \cdot \frac{\pi \cdot r_a^2}{t_a}, \qquad \left| C_a \right| = 2.662 \times 10^{-9} F \qquad \rho_a = 7600 \frac{kg}{m^3}$$

substitution of typical values for APC piezoceramic result the graph below
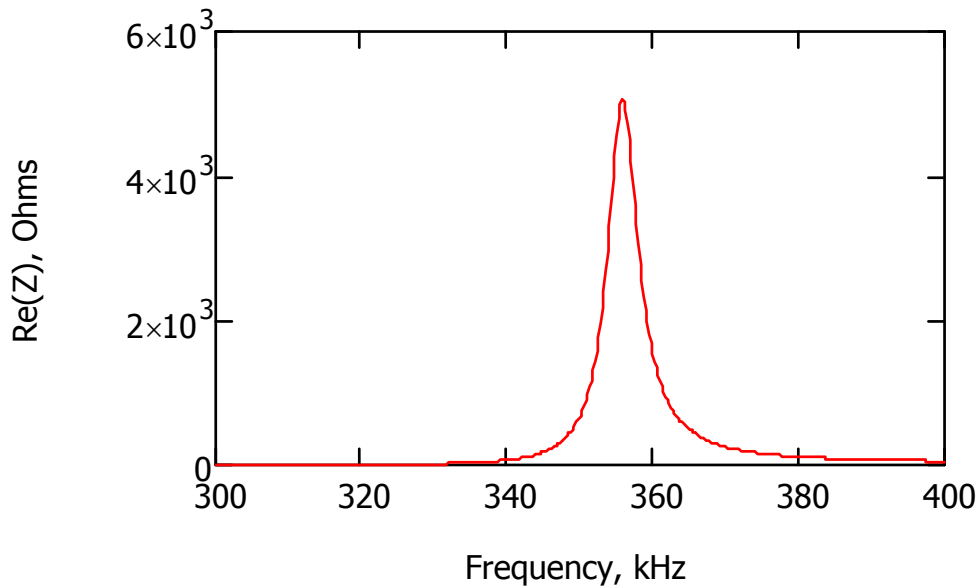
Figure 108 Real part of the electro-mechanical impedance of thin disk piezoelectric sensor.

Displacement is governed by

$$\xi_i = \frac{d'_{31} \cdot (1 + \sigma) \cdot r_a \cdot J_1(\phi_i) \cdot E_0}{\phi_i \cdot J_0(\phi_i) - (1 - \sigma) \cdot J_1(\phi_i)} \qquad (19)$$

For voltage input of 10 V, the graph below illustrates frequency-dependent output of the piezoelectric disk.

Theoretical values were compared with experimental data presented above. In general, theoretical curve matches well with experimental data. Deviations come from material parameter variability and influence of feedback (flipped over) electrode.
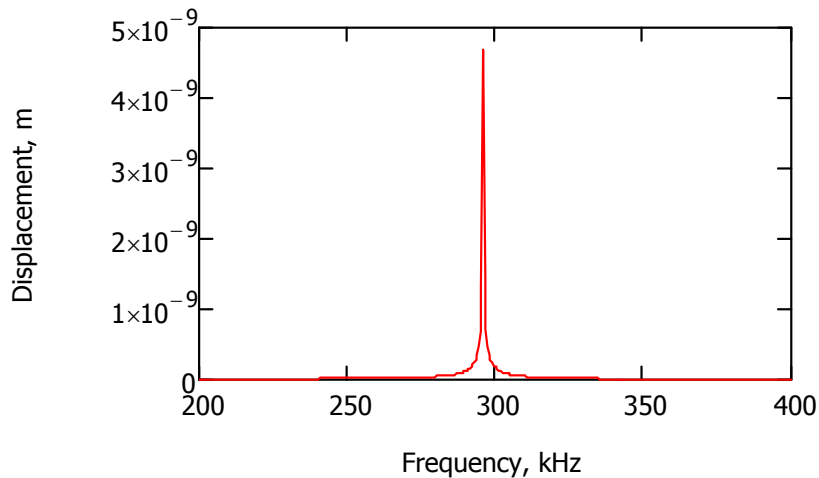
Figure 109 Displacement of piezoelectric disk actuator.

4.7.5 Voltage Output Analysis of PWAS Connected to RITEC System

It should be remembered that transmission of an elastic wave depends on both actuator and signal generator/amplifier characteristics. In the ideal case, both of them are linear. However, high power signal generators, such as RITEC, may exhibit nonlinearities that need to be accounted for while building statistical models. For this reason, we turn our attention to signal generator output as one of constitutive elements of the modeling scheme.

Piezoelectric sensors can be damaged when they are excited with high voltage. This means that it is important to make sure the pulse signal being sent to the sensors is at a level which will not harm the sensor or compomise its integrity. In order to make sure this does not occur, it became crucial to investigate the voltage output of the RITEC at different output level settings in the RITEC control panel. The software which controls the RITEC allows one to change the output level of the signal, however, it does not allow you to specify the exact voltage necessary. Instead, the user inputs a number ranging from -25 To 100 which corresponds a voltage which is actual produced by the RITEC. To determine the voltage levels being emmited at the specified levels the following test was performed.

The RITEC outputs were connected to an Tektonix TDS2024B, four channel, digital storage oscilloscope as shown in Figure 110. This allowed us to monitor the trigger signal, the gate signal, the RF burst monitor as well as the RF burst. The first step was to configure the oscilloscope so it would trigger off the trigger signal from the RITEC. RITEC generates a pulse by creating a contiuous waveform at the specific frequency and level which is desired. The user is able to specify the burst length in one of two ways: by the pulse length in time or by the number of cycles in the pulse. Based on the information specified by the user the RITEC generates a pregate signal which controls the burst. When the pregate signal is high the continuous wave is allowed through, which creates a burst and when it goes low again the wave is not allowed through. Channel 3 on the oscilloscope clearly showed the pregate signal which coincided exactly with the monitored burst, which confirmed that this function was operated as expected.
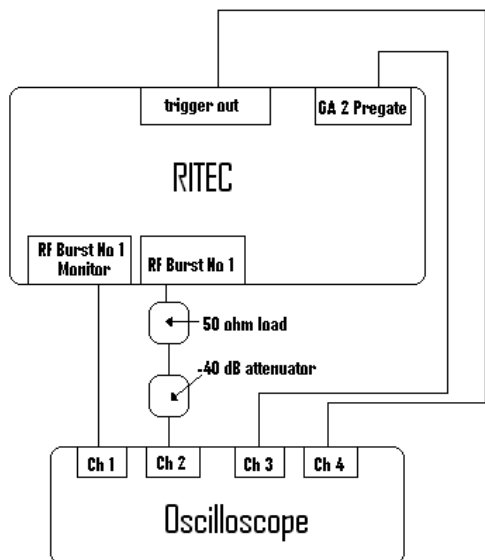
Figure 110 RITEC output characteristic test setup

The RF Burst No 1 monitor was connected to Ch1 on the oscilloscope. The RITEC monitor has an internal attenuator which is set to -60 dB. This means that the amplitude of recorded signal should be 1000 times less than the actual RF burst. The RF Burst signal was connected to Ch 2 through a 50 ohm load and an attenuator set to -40 dB, meaning that the recorded signal is 100 times less than the actual output. The attenuator was included to make sure the oscilloscope was not damaged by the voltage levels being monitored from the RITEC. By comparing the Ch 1 and 2 it was verified that the attenuator was working correctly. The voltage was determined by measuring from the middle of the waveform to the top of the peak.

After it was verified that the pulse triggering and displaying was working properly and the oscilloscope was correctly setup, the voltage test was performed. This was done by taking voltage measurements of a 5-pulse, 350 kHz harmonic RF pulse from output levels ranging from -25 to 100 in the RITEC control software.Table 11 shows the actual data from the experiment and this is visualized in Figure 111. The values reported are the voltages adjusted to correspond for the voltage before the signal goes through the -40 dB attenuator.

Table 11   Voltages corresponding RITEC output levels

RITEC Output Level	Volts	RITEC Output Level	Volts	RITEC Output Level	Volts
-25	10.5	10	85	45	290
-20	15	15	110	50	330
-15	21	20	130	60	400
-10	29	25	160	70	480
-5	40	30	187	80	560
0	50	35	220	90	630
5	64	40	255	100	770

From Figure 111 it can be seen that the relationship between the RITEC output and the actual voltage is not a linear one. A polynomial trend line seems to fit the graph best and is very close to polynomial of using a power of 2. However, it should be noted that the graph is fairly linear for the RITEC output values between 20 and 90. It was decided that the highest excitation level which is used to excite the piezoelectric actuators should not be greater than

Approved for Public Release; Distribution Unlimited.

200 volts. From the table and graph we can see the voltage crosses this threshold between output levels of 30 and 35. The results indicate that the highest output level one should use for piezoelectric excitation with RITEC is around 30.
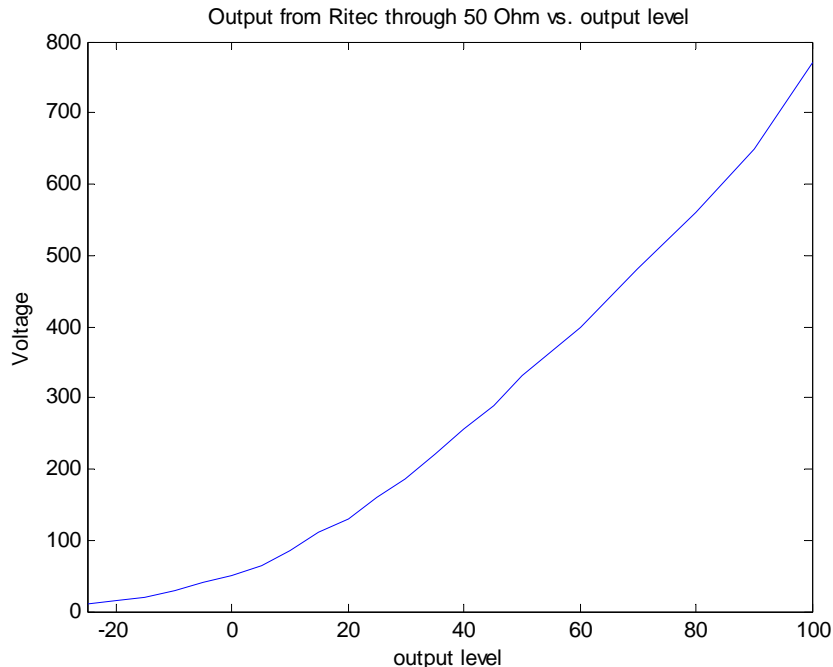
Figure 111 RITEC software level versus actual output voltage.

5   CONCLUSIONS

A comprehensive review was conducted on prior SHM efforts in space systems. Practical experimental systems mostly feature fiber optic and acoustic emission sensors. A few studies were available on use of embeddable piezoelectric sensors, but no systematic SHM efforts for space structures were considered. This situation likely occurred due to difficulties in determining actual tasks of SHM system in space vehicles. It is advocated that monitoring of structural interfaces should be a focus of spacecraft SHM and such monitoring would have a clear economic benefit during spaceship pre-launch diagnosis and qualification. Main elements of an SHM system for space craft were suggested and potential impact of space weather factors were considered

Instantaneous amplitude and phase signal processing approaches were explored for extraction of signal instantaneous features sensitive to the condition of structural interfaces. It was found that the effect of damage is pronounced in both amplitude and phase features, but phase offers much more stable detection. The Hilbert-Huang Transform has revealed

deviation of instantaneous frequency over time as a possible damage detection and classification feature.

To investigate the effect of applied stress on wave propagation in metallic material, laboratory tests were conducted in which embeddable piezoelectric sensors were attached to a thin plate subjected to monotonically increased stress. Under applied stress, the elastic wave signal has shown noticeable phase shift proportional to stress magnitude. Both symmetric and anti-symmetric waves have shown this phase shift, but analysis of the latter one was difficult due to low amplitude and noise contamination. It also needs to be mentioned that a phase shift depended on mutual orientation of vectors of applied force and direction of wave propagation. Pronounced phase changes were observed for cases when the elastic wave propagated in the direction (parallel) to the applied load. Vanishingly small changes were observed for wave paths oriented perpendicularly to applied load.

A numerical model describing acousto-elastic effect in thin plates was attempted, but not finalized yet due to issues with the dedicated PC station. Elastic wave propagation in thin plates was modeled and current results show good agreement between experimental, analytical and numerical data.

Acousto-elastic experiments in structures of simple geometry were conducted and demonstrated the capability of the method to detect the location of a loose bolt and establish correlation between the levels of torque (i.e. stress) in the joint and the phase shift of propagated elastic waves. The best detection was achieved for cases when a baseline (a record of elastic wave corresponding to healthy "tight" condition of the joint) was available. However, a new baseline-free method based on rotation of phases in the transmitted elastic wave was developed and verified in experimental studies. Sensitivity of the baseline-free method was lower than the method involving the baseline.

Structures of complex geometry were represented with a realistic aluminum satellite panel. The panel featured an isogrid design and 49 bolts connecting two parts of the panel. Similarly to the tests conducted for simple structures, the acousto-elastic method in complex structures has shown an ability to detect and locate a loose bolt. It was demonstrated that the efficiency of detection depends on wave propagation distance and active sensor excitation levels. Best results were obtained for cases when a baseline representing intact condition of the joint was available. The baseline-free method, based on rotation of initial phases in the transmitted wave, has shown utility in detecting loose bolts located on direct wave propagation path between transmitting and receiving sensors. The availability of the baseline removes this limitation. Another interesting fact uncovered during experimental studies was larger standard deviation of signals corresponding to "loose" condition of the joint. Therefore, a new methodology for baseline-free statistics-based detection was proposed in which several nominally identical signals were transmitted, response of the joint was measured, and the associated standard deviation for the obtained set of data was calculated. Based on the level of standard deviation, one may infer the condition of the joint.

The acousto-elastic method was validated in a set of experiments conducted on the PnP satellite. A method involving recording a baseline of the intact condition has shown very good performance while the baseline-free method was successful in many, but not all cases.

New Mexico Tech developed and launched a payload on a suborbital flight in May 2011. A bolted joint experiment was part of the payload, but because of limited flight hardware, wave propagation acousto-elastic studies were conducted only in pre-flight and post-flight conditions. To the author's knowledge, this is the first known case of acousto-elastic monitoring of a flown payload. Analysis indicated that the spaceflight clearly changed the torque state in a bolted joint. However, quantification of the change was not possible using pre and post flight data. To infer details of joint behavior, a real-time acousto-elastic system for monitoring bolted joint conditions during flight is needed.

The possibility to update space structure models using material parameters inferred from high frequency wave propagation tests was considered. Experiments have demonstrated the feasibility of determining elastic modulus and Poisson ratio from wave propagation tests. The effect of stress changes in boundary conditions was investigated using pitch-catch, pulse-echo and electro-mechanical impedance methods. All methods have shown utility in detecting changes in boundary condition, but pulse-echo was also instrumental in locating the site of stress variations.

Applicability of piezoelectric sensors to SHM of space structures was given special attention. It was confirmed that Hysol® adhesive performed well as a bonding agent for sensors during suborbital flight. Sensor shielding options were investigated and two shielding designs were suggested. Statistical studies on a relatively large sensor sample set were conducted and demonstrated: statistical distribution for natural frequency of low frequency extensional mode was found to follow the normal distribution pattern, however natural frequencies of the high frequency thickness mode did not follow the normal distribution pattern. Noticeable differences were observed for impedance signatures of sensor with and without leads attached. The impedance model has shown reasonable correlation with experimental data.

REFERENCES

1. Chona, R., (2005) "Aerospace Structures for the 21st Century: An Air Force Perspective on Research Needs," SDM Keynote Lecture, 46th AIAA/ASME/ASCE/AHS/ASC ADM Conference, Austin, Texas, April 18, 2005.
2. Arritt, B.J., *et. al.* (2008) "Structural health monitoring; an enabler for responsive satellites," *Proceedings of SPIE on Health Monitoring of Structural and Biological Systems*, Vol. 6935.
3. Brotherhood, C.J., Drinkwater, B. W. Dixon, S., (2003) "The detectability of kissing bonds in adhesive joints using ultrasonic techniques," Ultrasonics, Vol. 41, Issue 7, pp. 521-529.
4. Yang, S., Gu, L., Gibson, R.F., (2001) "Nondestructive detection of weak joints in adhesively bonded composite structures," Composite Structures, Vol. 51, Issue 1, pp. 63-71.
5. Rokhlin, S.I., Wang, L., Xie, B., Yakovlev, V.A., Adler, L. (2004) "Modulated angle beam ultrasonic spectroscopy for evaluation of imperfect interfaces and adhesive bonds," *Ultrasonics*, Vol. 42, pp. 1037–1047.
6. Matt, H., Bartoli, I. Lanza Di Scalea, F., (2005) "Ultrasonic guided wave monitoring of composite wing skin -to-spar bonded joints in aerospace structures," *Journal of the Acoustical Society of America*, v 118, n 4, pp. 2240-2252.
7. Cuc, A.; Giurgiutiu, V.; Joshi, S.; Tidwell, Z. (2007) "Structural health monitoring with piezoelectric wafer active sensors for space applications," *AIAA Journal*, Vol. 45, No. 12, pp. 2838-2850, Dec. 2007.
8. Jhang, K.Y., Quan, H.H., Ha, J., Kim, N.Y., (2006), "Estimation of clamping force in high tension bolts through ultrasonic velocity measurement," Ultrasonics, Vol. 44, pp el339-el342.
9. Adams, D.E. and Nataraju, M. (2002) "A Nonlinear Dynamical Systems Framework for Structural Diagnosis and Prognosis," International Journal of Engineering Science, Volume 40, Issue 17, October 2002, pp. 1919-1941.
10. Clayton, E.H., Kennel, M.B., Fasel, T. R., Todd, M.D., Stabb, M.C., Arritt, B.J., (2008) "Active ultrasonic joint integrity adjudication for real-time structural health monitoring," *Proceedings of SPIE on Health Monitoring of Structural and Biological Systems*, v 6935.
11. Yang, J., Chang, F., (2006) "Detection of bolt loosening in C–C composite thermal protection panels: II. Experimental verification," Smart Materials and Structures, Vol. 15, pp. 591-599.
12. Mascarenas D.L, Park G., (2005) "Monitoring of Bolt Preload using Piezoelectric Active Devices," *Structural Health Monitoring and Smart NDE of Structural and Biological Systems IV*, Proceedings of SPIE Vol. 5768, pp. 129-136.
13. Zagrai, A. Doyle, D., Arritt, B., (2008) "Embedded nonlinear ultrasonics for structural health monitoring of satellite joints," *Proceedings of SPIE on Health Monitoring of Structural and Biological Systems*, v. 6935.
14. Park, G., Cudney, H.H., and Inman, D.J. (2000) "An Integrated Health Monitoring Technique Using Structural Impedance Sensors," Journal of Intelligent Material Systems and Structures, Vol. 11, No. 6, June 2000, pp. 448-455.
15. Tseng, K. and Naidu, A., (2002) "Non-Parametric Damage Detection and Characterization Using Smart Piezoceramic Materials," Smart Materials and Structures, Vol. 11, 317–329.
16. Giurgiutiu, V., *Structural Health Monitoring: with Piezoelectric Wafer Active Sensors*, Academic Press, 2007.
17. Mancini, S., Tumino G., Gaudenzi, P. (2006) "Structural Health Monitoring for Future Space Vehicles," *Journal of Intelligent Material Systems and Structures*, Vol. 17, No. 7, pp. 577-585.
18. Mizutani, T., Takeda, N., Takeya, H., (2006) "On-board Strain Measurement of a Cryogenic Composite Tank Mounted on a Reusable Rocket using FBG Sensors," Vol 5(3), pp. 205–210.
19. Baumann, E.W., Becker, R.S., Ellerbrock, P.J. and Jacobs, S.W. (1997) "DC-XA structural health monitoring system," Proceedings of SPIE's Smart Structures and Materials, Vol. 3044, pp. 195–206.
20. Ellerbrock, P.J. (1997) "DC-XA structural health monitoring fiber-optic based strain measurement system," Proceedings of SPIE's Smart Structures and Materials, Vol. 3044, pp. 207–218.

21. Jassemi-Zargani, R., Simard, J.F., Blacow, R.G., Waechter, D.F., and Prasad, S.E. (1999) "Utilization of Smart Structures in Enhanced Satellites," Proceedings of 2nd CanSmart Workshop on Smart Materials and Structures, pp. 157-164.

22. Finlayson, R.D., Schaafsma, D.T., Shen, H.W., Carlos, M.F., Miller, R.K., and Shepherd, B., (2001) "Continuous health monitoring of Graphite Epoxy Motorcases (GEM)," Proceedings of SPIE's Smart Structures and Materials, Vol. 4335, pp. 155-166.

23. Kabashima, S., Ozaki, T., Takeda, N., (2001) "Structural Health Monitoring using FBG Sensor in Space Environment," Proceedings of SPIE, Vol. 4332, pp. 78-87.

24. Shimizu, T., Yari, T., Nagai, K., and Takeda, N., (2001) "Strain measurement using a Brillouin optical time domain reflectometer for development of aircraft structure health monitoring system," Proceedings of SPIE, Vol. 4335, pp. 312-322.

25. Mizutani, T., Takeda, N., Takeya, H., (2006) "On-board Strain Measurement of a Cryogenic Composite Tank Mounted on a Reusable Rocket using FBG Sensors," Structural Health Monitoring, Vol. 5, N. 3, pp. 205-214.

26. Mckenzie, I. and Karafolas, N., (2005) "Fiber optic sensing in space structures: the experience of the European Space Agency," Proceedings of SPIE, Vol. 5855, pp. 262-269.

27. Boller, C., Chang, F.-K., Fujino, Y. (eds.) *Encyclopedia of Structural Health Monitoring*, Wiley, 2009.

28. Mancini, S., Tumino, G., Gaudenzi, P., (2006) "Structural Health Monitoring for Future Space Vehicles," *J. Intell. Mater. Syst. Struct*, Vol. 17-July 2006, pp. 577-585.

29. Qing X.P., Chan H.L., Beard S.J., and Kumar, A. (2006) "An active diagnostic system for structural health monitoring of rocket engines," *J. Intell. Mater. Syst. Struct*. Vol. 17, pp. 619–628.

30. Qing, X.P., Beard, S.J., Kumar, A., Sullivan, K., Aguilar, R., Merchant, M., and Taniguchi, M., (2008) "The performance of a piezoelectric-sensor-based SHM system under a combined cryogenic temperature and vibration environment," *Smart Mater. Struct.* 17, pp. 1-11.

31. Clayton, E.H., Kennel, M.B., Fasel, T.R., Todd, M.D., Stabb, M.C., Arritt, B.J. (2008) "Active Ultrasonic Joint Integrity Adjudication for Real-time Structural Health Monitoring," Proceedings of SPIE, Vol. 6935, pp. 69350M-1-11.

32. Zagrai, A., Doyle, D., Arritt, B., (2008) "Embedded Nonlinear Ultrasonics for Structural Health Monitoring of Satellite Joints," Proceedings of SPIE, Vol. 6935, 693505.

33. Yang, J. and Chang, F.-K., (2006) "Detection of bolt loosening in C–C composite thermal protection panels: II. Experimental verification," *Smart Mater. Struct*. 15 (2006) pp. 591–599.

34. Xie, W., Zhang, B., Du, S., and Dai, F. (2007) "Experimental Investigation of Bolt Loosening Detection in Thermal Protection Panels at High Temperatures," *Proceedings of 6th International Workshop on Structural Health Monitoring*, Stanford 2007, Vol. 2, pp. 1480-1490.

35. Yu, P. (2007) "Real-time Impact Detection System for Thermal Protection System," *Proceedings of 6th International Workshop on Structural Health Monitoring*, Stanford 2007, Vol. 1, pp. 153-158.

36. Na, J.K., Kuhr, S.J., and Jata, K. (2008) "Detection of impact damage on thermal protection systems using thin-film piezoelectric sensors for integrated structural health monitoring," Proceedings of SPIE, Vol. 6935, pp. 693503-1-8.

37. Giurgiutiu, V. (2008) *Structural Health Monitoring with Piezoelectric Wafer Active Sensors*, Academic Press, 2008.

38. Pisacane , V.L., (2008) *The Space Environment and its Effects on Space System*s, AIAA Education series.

39. Dargaville, T.R., Celina, M.C., Elliott, J.M., Chaplya, P.M., Jones, G.D., Mowery, D.M., Assink, R.A., Clough, R.L., Martin, J.W. (2005) "Characterization, Performance and Optimization of PVDF as a Piezoelectric Film for Advanced Space Mirror Concepts," Sandia Report, SAND2005-6846.

40. Sarafin T.P, and Doukas P.G, 2007, "Simplifying the Structural Verification Process to Accommodate Responsive Launch," AIAA-RC5 2007-5003, Proceedings of the 5th Responsive Space Conference.

41. Arritt, B.J., Buckley, S.J., Ganley, J.M., Kumar, A., Clayton, E.H., Hannum, R., Todd, M.D., Kennel, M.B., Welsh, J., Beard, S., Stabb, M.C., Xinlin, Q., Wegner, P., 2007, "Responsive Satellites and the Need for Structural Health Monitoring," Proceedings of the SPIE, Volume 6531, pp. 6531-09.

42. Couchman J., Bell J., Noronha P., (1976) "Computerized Signal Processing for Detecting Cracks Under Installed Fasteners," Ultrasonics, pp. 256-262, November 1976.

43. Light, G.M., Ruescher, R.H., Bloom, E.A., Joshi, N.R., Tsai, Y.M., Liu, S.N., (1993) "Application of the cylindrically guided wave technique for bolt and pump shaft inspections," Nuclear Engineering and Design, Vol. 144, pp. 465-468, Elsevier Science Publishers, 1993.

44. Jhang, K.Y., Quan, H-H., Ha, J., Kim, N-Y., (2006) "Estimation of Clamping Force in High-Tension Bolts through Ultrasonic Velocity Measurement," Ultrasonics, Vol. 44, e1339-e1342, 2006.

45. Mascarenas D.L, Park G., (2005) "Monitoring of Bolt Preload using Piezoelectric Active Devices," Structural Health Monitoring and Smart NDE of Structural and Biological Systems IV, Proceedings of SPIE Vol. 5768, pp. 129-136.

46. Doyle, D., Zagrai, A., and Arritt, B., (2009) "Bolted Joint Integrity for Structural Health Monitoring of Responsive Space Satellites," 50th AIAA/ASME/ASCE/AHS/ASC Structures, Structural Dynamics, and Materials Conference, 4-7 May 2009, Palm Springs, California, paper: AIAA 2009-2705.

47. Huang *et al*, 1998, "The empirical mode decomposition and the Hilbert spectrum for nonlinear and non-stationary time series analysis," *Proc. Royal Soc. London A*, 454, pp. 903-995

48. Norris, A.N., (1997) "Finite-Amplitude Waves in Solids," in Nonlinear Acoustics edited by Hamilton, M.F. and Blackstock, D.T., Academic Press, 1997.

49. Zarembo, L.K. and Krasil'nikov, V.A. (1971) "Nonlinear Phenomena in the Propagation of Elastic Waves," Sov. Phys. Usp., 13, pp. 778-797.

50. Giurgiutiu, V., (2005) "Tuned Lamb Wave Excitation and Detection with Piezoelectric Wafer Active Sensors for Structural Health Monitoring," Journal of Intelligent Material Systems and Structures, Vol. 16, April 2005, pp. 291-305.

51. Doyle, D., Zagrai, A., Arritt, B.J., Çakan, H., (2008) "Damage Detection in Satellite Bolted Joints," Proceedings of SMASIS-08, ASME Conference on Smart Materials, Adaptive Structures and Intelligent Systems, Oct. 28-30, 2008, Ellicott City, Maryland, paper: SMASIS2008-550.

52. Doyle, D., Zagrai, A., Arritt, B., Çakan, H., (2010) "Damage Detection in Bolted Space Structures," Journal of Intelligent Material Systems and Structures, Vol. 21, N. 3, pp. 251-264, first published on November 25, 2009.

53. William R. Reiser, Brandon Runnels, Chris White, Abraham Light-Marquez, Andrei Zagrai, David Siler, Stephen Marinsek, Andrew Murray, Stuart Taylor, Gyuhae Park, Charles Farrar, Richard Sansom, (2012) "Design, Development, and Assembly of Sub-orbital Space Flight Structural Health Monitoring Experiment," *Proceedings of SPIE's 19th Annual International Symposium on Smart Structures and Materials + NDE for Health Monitoring and Diagnostics*, 11-15 March 2012, San Diego, CA.

54. Friswell M., Mottershead, J.E. (1995) *Finite Element Model Updating in Structural Dynamics (Solid Mechanics and Its Applications)*, Springer, 1995.

55. Meeker, T.R., and Meitzler A.H. (1964) "Guided Wave Propagation in Elongated Cylinders and Plates," in Physical Acoustics, Vol. I, Part-A, edited by Mason, W.P.

56. Lin, B., Giurgiutiu, V., Pollock, P., Xu, B., Doane, J., (2010) "Durability and Survivability of Piezoelectric Wafer Active Sensors on Metallic Structures," *AIAA Journal*, Vol. 48, No. 3, pp. 635-643.

Journal Publications

1. Zagrai, A., Doyle, D., Gigineishvili, V., Brown, J., Gardenier, H., Arritt, B., (2010) "Piezoelectric Wafer Active Sensor Structural Health Monitoring of Space Structures," Journal of Intelligent Material Systems and Structures, Vol. 21, N. 9, pp. 921-940, first published on May 4, 2010.

2. Doyle, D., Zagrai, A., Arritt, B., Çakan, H., (2010) "Damage Detection in Bolted Space Structures," Journal of Intelligent Material Systems and Structures, Vol. 21, N. 3, pp. 251-264, first published on November 25, 2009.

Conference Papers and Presentations

1. Murray, A., Zagrai, A., Conrad, D. (2011) "Diagnosis of Space Structures Using Embedded Sensors and Elastic Waves," *SPIE's 18th Annual International Symposium on Smart Structures and Materials and 16th Annual International Symposium on NDE for Health Monitoring and Diagnostics*, 6-10 March 2011, San Diego, CA, v 7984. paper 7984-22, pp. 79840N-1-12.

2. Zagrai, A, (2011) "Structural Sensing During Suborbital Space Flight," Technical presentation at AFOSR Annual Grantees Meeting, University of Dayton Research Institute, August 9-11, 2011, Dayton, Ohio

3. Zagrai, A, (2011) "Piezoelectric Wafer Active Sensing During Suborbital Space Flight," Technical presentation at ASME Conference on Smart Materials, Adaptive Structures and Intelligent Systems, September 18 – 21, 2011, Scottsdale, AZ, presentation: SMASIS2011-5274.

4. Zagrai, A., (2010) "Embedded Ultrasonic Characterization of Interfaces in Space Structures," AFOSR Workshop on Improved Precision for Space Systems, 27-28 May 2010, Albuquerque, NM.

5. Zagrai, A., Gigineishvili, V., Kruse, W., Murray, A., Doyle, D., Reynolds, W., Arritt, B., Gardenier, H., (2010) "Acousto-Elastic Measurements and Baseline-Free Assessment of Bolted Joints using Guided Waves in Space Structures," *SPIE's 17th Annual International Symposium on Smart Structures and Materials and 15^{h} Annual International Symposium on NDE for Health Monitoring and Diagnostics*, 7-11 March 2010, San Diego, CA, v 7650, n PART 1, paper 7650-41, pp. 765017-1-12.

6. Zagrai, A.N., Doyle, D., Gigineishvili, V., Brown, J., Gardenier, H., Arritt, B., (2009) "Developing a Piezoelectric Active Sensor SHM System for Satellites," *Proceedings of SMASIS-09, ASME Conference on Smart Materials, Adaptive Structures and Intelligent Systems*, September 20-24, 2009, Oxnard, California, paper: SMASIS2009-1342.

7. Barnes, T., Zagrai, A.N. Kukhalashvili, D., Doyle, D., Arritt, B., Gardenier, H., (2009) "Development of Magneto-Elastic Active Sensors (MEAS) for Damage Detection in

Aerospace Structures," *Proceedings of 7ᵗʰ International Workshop of Structural Health Monitoring*, 9-11 September 2009, Stanford University, California, pp. 1096-1103.

8. Doyle, D., Zagrai, A., Arritt, B., (2009) "Bolted Joint Integrity for Structural Health Monitoring of Responsive Space Satellites," *50ᵗʰ AIAA/ASME/ASCE/AHS/ASC Structures, Structural Dynamics, and Materials Conference*, 4-7 May 2009, Palm Springs, CA, paper: AIAA-2009-2705.

APPENDIX B
LIST OF PEOPLE INVOLVED IN RESEARCH EFFORTS

Vlasi Gigineishvili – MS student

Andrew Murray – MS student

Walter Kruse – MS student temporarily

Daniel Kitts – MS student temporarily

David Conrad – MS student temporarily

DISTRIBUTION LIST

DTIC/OCP

8725 John J. Kingman Rd, Suite 0944

Ft Belvoir, VA 22060-6218   1 cy

AFRL/RVIL

Kirtland AFB, NM 87117-5776   2 cys

Official Record Copy

AFRL/RVSV/Whitney Reynolds   1 cy

(This page intentionally left blank)